Trapping and Cooling of Ions and the Study of Ion Atom Interactions

by

Ravi Krishnamurthy

a thesis submitted to
Jawaharlal Nehru University
for the degree of

Doctor of Philosophy

2012

Raman Research Institute
Bangalore 560 080
India

Declaration

I hereby declare that the work reported in this thesis is entirely original. This thesis has been composed by me at Raman Research Institute under the supervision of Dr. Sadiq Rangwala. I further declare that, to my best knowledge, the matter presented in this thesis has not formed the basis for the award of any degree, diploma, membership, associateship, fellowship or any other similar title of any university or institution.

Ravi Krishnamurthy

Countersigned:

Dr. Sadiq Rangwala
Light and Matter Physics Group
Raman Research Institute
Bangalore-560 080

Certification

This is to certify that the thesis titled **"Trapping and Cooling of Ions and the Study of Ion Atom Interactions"** submitted by Ravi Krishnamurthy for the award of the degree of Doctor of Philosophy of Jawaharlal Nehru University is a bona-fide work. This has not been submitted to any other university for any other degree, diploma or title.

Dr. Sadiq Rangwala
(Thesis Supervisor)
Light and Matter Physics Group
Raman Research Institute
Bangalore-560 080

Prof. Ravi Subrahmanyan
Director
Raman Research Institute
Bangalore-560 080

Acknowledgements

First of all I would like to express my deep thanks to Dr. Sadiq Rangwala for giving me an opportunity to work in his group and envisaging, facilitating, advising and supervising my thesis work.

I am indebted to Prof. G. Werth, Institut für Phyzik, Mainz, Germany for collaborating with our group and sharing his vast experience and expertise on ion trap physics. The collaboration has been very fruitful and helped us to conceive, design and understand the experimental and theoretical aspects of this work.

I wish to thank the director and the administrative department of Raman Research Institute (RRI) for providing the environment to embark on this experimental project. I also thank Dr. Reji Philip and Dr. Yashodhan Hatwalne for periodic review and assessment of my thesis work.

I gratefully acknowledge the technical support of Mr. N. Narayanaswamy, Mr. Achan Kunju, Mr. V. Dhamodaran (retd.), Mr. V. Venu (retd.), Mr. R. Elumalai and all members of the RRI general and precision workshops. My special thanks to Mr. Narayanswamy for fabricating many of the precision mechanical components used in the experiments including diode laser mounts and the entire ion trap assembly. I thank Mr. R. Duraichelvan for rendering the schematic 3D diagram of the experimental chamber.

I sincerely thank Mrs. S. Sujatha from the Radio Astronomy Laboratory for her extensive support in designing, fabricating and testing of many of the electronic components used in the experiments. She has been extremely supportive in debugging and addressing problems with electronic instruments at various stages of the experiment.

I thank Ms. Lee Seunghyun, Mr. Tridib Ray, Mr. Arijit Sharma, Ms. S. Jyothi and all the present and past members of the Quantum Interactions (QuaInt) Lab for their co-operation, collaboration and useful discussions. Special thanks

to Ms. Lee Seunghyun for her extensive role in the measurements, analysis and discussions. I would also like to acknowledge her significant role in quantifying the kinematics of ion-atom collisions relevant to our system and programming a molecular dynamics framework that helped us in understanding ion trapping and detection in the many-ion regime.

My thanks to all the members of the Light and Matter Physics (LAMP) group at RRI for their help and co-operation. I would like to thank Mr. Nandan Satapathy for useful discussions and sharing technical know-how on cold-atom physics.

I finally thank the entire staff of RRI including Marisa, Radha, Meena, Shiva, Manju, Jacob, Sridhar, Nandu, Krishnamurthy and all the people who have directly or indirectly helped in the accomplishment of the present work.

Synopsis

The experimental study of collisions is a vast field of physics with a multitude of approaches taken to explore diverse problems related to classical and quantum scattering, resonance phenomena, inelastic processes and few-body systems. As a parallel approach to the beam-target experiments, the quest to explore interactions between particles at very low collision energies has led to technological advances in creating cold, trapped ensembles of atoms, ions and molecules. The low temperatures of the order of a few hundred micro kelvin and the corresponding low kinetic energy of the constituents makes these ensembles ideal for studying interactions and quantum phenomena as opposed to ensembles at higher temperatures where many of the effects are obscured. The techniques of laser cooling and trapping have been extensively developed for both ions and neutral atoms with promise in a variety of applications. An emerging area of research is the cold and ultra-cold chemistry with atoms, ions and molecules as the principal material ingredients [1]. In this context, mixed systems of cold atoms and ions [2, 3, 4, 5, 6, 7] act as a test bench for studying ion assisted cold chemistry [8, 9, 10, 11] and novel many body phenomena [12].

The primary motivation for the present work is to experimentally explore the interactions that manifest in a mixed system of atoms and ions. Such a mixed system can be used to study the ion-atom collision dynamics, the interactions between the atoms in the presence of ions and cold chemical reactions such as the formation of molecules and molecular ions. The presence of ions interspersed in a cloud of atoms is potentially a microscopic, many-centred aggregation mechanism, mediated by the Stark interaction, to reduce the inter atomic spacing and enhance the interactions between the atoms.

In order to explore these phenomena, an important technical requirement is the construction of an apparatus which is capable of holding cold ions and cold atoms simultaneously with spatial overlap. The apparatus must be able

to confine the species of interest in a state of equilibrium for sufficiently long interrogation times and allow for the creation, detection and manipulation of the ions and atoms as required using light and external fields. The flow of energy between the ions and atoms resulting from their interaction has to be well understood and characterized. The intrinsic stability of the ion-atom ensemble in such a system is a key requirement to enable further studies.

At the onset of the present work, the experimental study of ion atom collisions at very low energies was still at a nascent phase. The technical aspects of such studies were not yet well established. The principles of conventional buffer gas cooling had been explored and it was widely prevalent to use light mass atoms in a buffer gas to cool relatively heavier ion species. The creation of cold molecules in the ground rotational and vibrational states had not yet been demonstrated. The study of chemical reactions in cold ensembles of atoms, ions and molecules was also in its infancy. The idea of trapping ions and cold atoms simultaneously with spatial overlap was proposed and developed by Smith et.al. [2] in 2005. Subsequently, different aspects of such combined ion-atom systems have been studied experimentally in various groups worldwide.

In the context of the scientific goals envisaged above, the present work was undertaken with the following objectives:

- To design a combined trap that can confine $^{85}Rb^{+}$ ions and cold atoms simultaneously with spatial overlap.
- To construct such a combined trap and demonstrate its operation.
- To develop techniques for detection and diagnostics of the trapped species.
- To characterize the above trap to function as an instrument to study ion-atom interactions.
- To identify and formalize the ion-atom interactions that are relevant to the experimental system.

- To study the exchange of energy between the ions and atoms via their interaction and explore the possibility of cooling the ions by the cold atoms.
- To experimentally study the time-evolution of ion populations in the presence and absence of atoms and look for signatures of ion cooling.
- To understand the experimental observations using numerical calculations and models.

In the present work, we systematically address these objectives with an emphasis on the intrinsic stability of the ion-atom system. We design a combined trap that can confine $^{85}Rb^{+}$ ions and cold ^{85}Rb atoms simultaneously with spatial overlap. The established technology of Magneto-Optical Trap (MOT) is adopted to cool and trap the atoms. A modified linear Paul trap, that can simultaneously accommodate the MOT in the same region of trapping, is designed to confine the ions. The different regimes of operation of the ion trap and the effect of one trap on the other are numerically simulated and characterized.

The designed trap is successfully implemented and constructed. The simultaneous confinement of ions and cold atoms is demonstrated.

An indirect, destructive detection technique is implemented for the optically dark $^{85}Rb^{+}$ ions. The detection of ions is developed in two different regimes namely the discrete counting regime and the proportional counting regime. The detection of the atoms is realized by monitoring the laser light scattered by them. This fluorescence is measured to estimate the total number of atoms in the trap and their density distribution.

The parameter space of the ion trap is scanned to experimentally determine the stable regions of ion trapping. A generic experimental sequence is formulated and programmed to perform experimental studies of ion-atom interactions.

The elastic and resonant charge exchange collisions between the $^{85}Rb^{+}$ ions and the ^{85}Rb atoms are identified as the primary channels in our system. The

kinematics and mechanisms of these collisions involving ions and atoms in their ground state are formalized in the energy regimes that are relevant to our experiment.

A hypothesis is proposed for the cooling of ions by collisions with atoms in a spatially compact distribution, for all mass ratios, contrary to the expectations of conventional buffer gas cooling. This hypothesis is studied for the case of $^{85}Rb^{+}$ ions colliding with equal mass ^{85}Rb atoms in the MOT. The role of elastic collisions and resonant charge exchange collisions in the cooling process is studied by performing multiple-scattering numerical simulations. The hypothesis for cooling is shown to be valid when purely elastic collisions are present and the cooling process is shown to be accelerated in the presence of resonant charge exchange collisions. The glancing collisions where resonant charge exchange occurs is highlighted as an important mechanism of cooling, where in a fast ion colliding with an atom at rest can result in a slow ion and a fast atom.

The time evolution of the $^{85}Rb^{+}$ ion population in the ion trap is experimentally studied in the presence and absence of the ^{85}Rb atoms in the MOT as a function of the hold time. Significantly longer trapping times of the ions in the presence of the MOT atoms are observed compared to that in the absence of the MOT atoms, with all other conditions remaining the same. This is argued to be a stand-alone signature of ion cooling, thus verifying the above hypothesis. This establishes an alternate way of cooling charged species that are not amenable to direct laser cooling. The number of ions in the trap, after being in contact with the MOT atoms for certain hold time, is shown to be stabilized at a constant value within the limits of experimental error. The width of the ion arrival time distribution at the detector, which is a measure of the ion temperature, is measured as a function of the hold time and shows a qualitative signature of ion cooling. The intrinsic stability of the ion-atom ensemble demonstrated here, is a significant step towards further studies of interactions and cold-chemistry envisaged in the ion-atom system.

A Monte-Carlo simulation is performed to model the experimentally measured evolution of the trapped ion population in the absence of the MOT. A single exponential heating factor is assumed to collectively represent all the ion heating mechanisms and the functional form of the ion evolution given by this simulation shows good agreement with the observed data and we achieve quantitative agreement with a two-parameter fit. The heating factor hence derived is used in conjunction with the multiple scattering simulation to get the qualitative features of ion stability in the presence of atoms. The process of detection of the ions is numerically modelled for different initial position and velocity distributions of the ions to obtain a correspondence between the observed width of the ion arrival time distribution and the temperature of the ions in the trap. The range of temperatures and cloud sizes which correspond to the observed widths are established. The numerical simulations developed here provide a better understanding of the underlying processes in the system and are an essential tool to estimate various quantities in further studies of the system.

In summary, this work establishes the experimental aspects of a mixed system of trapped ions and cold atoms that is tailored to study the interactions between them. The exchange of energy between the ions and atoms via their interactions in such a system is studied and the intrinsic stabilization of the system using these interactions is demonstrated and characterized. This sets a platform for the further study of problems related to ion-atom collisions, cold chemistry and many body physics.

Contents

1 Introduction **1**

1.1 Overview 1

1.2 Motivations 2

1.3 Objectives 2

1.4 Organization of the thesis 3

2 Design of the Ion trap **5**

2.1 Introduction 5

2.2 Trap design 6

2.2.1 General considerations 6

2.2.2 The mechanical design and construction 8

2.3 Numerical simulation of the trapping 11

2.3.1 The potential 12

2.4 Stability diagrams 17

2.4.1 The ideal stability diagram 17

2.4.2 Scaled stability diagram 18

3 Experimental Setup **23**

3.1 The vacuum system 23

3.1.1 Pumping sequence 24

3.2 The Magneto Optical trap 27

3.2.1 Lasers 27

3.2.2 Magnetic coils 33

3.2.3 Loading of atoms 34

3.2.4 Detection of the atoms 35

3.3 The Ion Trap 39

3.3.1 Ionization methods 39

3.3.2 Method I: Resonant TPI 39

3.3.3 Method II: Non-Resonant TPI . . . 40
3.3.4 The RF and biasing system . . . 40
3.3.5 Detection of ions . . . 42
3.4 The data acquisition . . . 45
3.5 The experimental sequence . . . 47
3.6 Stability regions . . . 49

4 Interactions between trapped ions and cold dilute atoms 51
4.1 Introduction . . . 51
4.1.1 The possible interactions . . . 51
4.2 The collision channels . . . 52
4.2.1 The interaction potential . . . 53
4.3 Elastic collisions: Classical framework . . . 53
4.3.1 The critical impact parameter for elastic collisions . . . 59
4.4 Inelastic collisions . . . 60
4.4.1 Resonant charge exchange (RCx) . . . 64
4.5 Conclusion . . . 69

5 Cooling of ions by interactions with cold atoms 72
5.1 The scope for sympathetic cooling . . . 73
5.2 Ion lifetime measurements . . . 78
5.2.1 Experimental procedure . . . 78
5.2.2 MOT-Ion trap overlap . . . 79
5.2.3 Observations . . . 81
5.3 Model for the ion heating in the absence of atoms . . . 81
5.3.1 The envelope of maximum energy . . . 82
5.3.2 Monte-Carlo . . . 83
5.4 Estimating the ion temperature . . . 84
5.5 Simulating the ion-atom collisions . . . 85
5.6 Simulation: The elastic and RCx channels . . . 87

5.7 Simulation: Collisions in the presence of ion heating 89

6 Conclusions **91**

6.1 Summary of the results 91

6.2 Perspectives and future challenges 93

A Mechanical drawings of the ion trap **95**

B List of computer programs **104**

CHAPTER 1

Introduction

1.1 Overview

The study of interactions in cold dilute gases is a field of experimental physics that has seen a lot of technological developments in recent years. The low temperatures of the order of a few hundred micro kelvin and the corresponding low kinetic energy of the constituents makes these ensembles ideal for studying interactions and quantum phenomena as opposed to ensembles at higher temperatures where many of the effects are obscured. The techniques of laser cooling and trapping have been extensively developed for both ions and neutral atoms with promise in a variety of applications.

The cooling and trapping of ions and atoms have a number of similarities in terms of the experimental techniques and the physics they address. Individually, cold atom physics as well as cold ion physics are both sufficiently advanced for investigating some of the most exciting problems, ranging from sensitive tests of QED, fundamental interactions and symmetries at one end to many particle physics at the other [13, 14, 15, 16]. An emerging area of research is the cold and ultra-cold chemistry with atoms, ions and molecules as the principal material ingredients [1]. In this context, mixed systems of cold atoms and ions [2, 3, 4, 5, 6, 7] act as a test bench for studying ion assisted cold chemistry [8, 9, 10, 11] and novel many body phenomena [12].

The idea of trapping ions and cold atoms simultaneously with spatial overlap was originally proposed and developed by Smith et.al. [2]. Subsequently, different aspects of such combined ion-atom systems have been studied experimentally in various groups worldwide. Cold ion-atom collisions have been

studied between different isotope combinations of Yb and Yb+ in laser-cooled thermal ensembles [4]. The technology of immersing a single trapped ion in a BEC has been demonstrated [5, 6] and the ion has been used as a probe for the atoms [6]. Cold chemical reaction kinetics have been experimentally studied for mixed species of ions and atoms [10, 11]. In addition there have been studies on the dynamics of trapped ions in the presence of micromotion heating in buffer gases [17, 18].

1.2 Motivations

The primary motivation for the present work is to experimentally explore the interactions that manifest in a mixed system of atoms and ions. Such a mixed system can be used to study the ion-atom collision dynamics, the interactions between the atoms in the presence of ions and cold chemical reactions such as the formation of molecules and molecular ions. The presence of ions interspersed in a cloud of atoms is potentially a microscopic, many-centred aggregation mechanism, mediated by the Stark interaction, to reduce the inter atomic spacing and enhance the interactions between the atoms.

1.3 Objectives

The key objectives that the present work aims to address are enumerated as follows:

- To design a combined trap that can confine $^{85}Rb^{+}$ ions and cold atoms simultaneously with spatial overlap.
- To construct such a combined trap and demonstrate its operation.
- To develop techniques for detection and diagnostics of the trapped species.

- To characterize the above trap to function as an instrument to study ion-atom interactions.
- To identify and formalize the ion-atom interactions that are relevant to the experimental system.
- To study the exchange of energy between the ions and atoms via their interaction and explore the possibility of cooling the ions by the cold atoms.
- To experimentally study the time-evolution of ion populations in the presence and absence of atoms and look for signatures of ion cooling.
- To understand the experimental observations using numerical calculations and models.

1.4 Organization of the thesis

The first part of this work mainly deals with the design, construction and operation of a combined ion-atom trap that can be used as a platform to study ion-atom interactions. We design the combined trap by suitably adapting two independently established technologies of ion and atom trapping namely the linear Paul trap and the Magneto-Optical trap (MOT) respectively. The combination of the two traps introduces additional constraints on the ion trap introducing significant deviations from the conventional designs. The second chapter of this thesis describes the design considerations and the numerical simulations that validate this design.

The third chapter describes in detail the actual construction and operation of the combined trap as an instrument to study ion-atom interactions. The vacuum system, the different components of the trap such as the lasers and electronics, the detection of the ions and atoms and the calibration of the instrument are discussed.

The latter part of the thesis focusses on the aspects of the ion-atom interactions and a method to cool the ions via these interactions. The fourth chapter establishes the formalism for describing the two important ion-atom interaction channels namely the elastic collisions and the resonant charge exchange collisions.

In the fifth chapter we propose and experimentally demonstrate a hypothesis for cooling the ions by collisions with the cold atoms in the MOT. The experimental data is modelled wherever possible and numerical simulations incorporating the ion-atom collisions are used to verify the hypothesis and to fortify the observations.

The thesis concludes with an outlook on the future directions of research that can possibly be undertaken using the system and the techniques discussed in this work.

CHAPTER **2**

Design of the Ion trap

2.1 Introduction

For constructing the experimental set-up that facilitates the goals envisaged in the previous chapter, the basic cornerstone is an ion-trap that can also accommodate a separate trap for the atoms. The atoms can be trapped in different energy regimes using different techniques of cooling and trapping. Depending upon the energy regime and the species, the atomic ensemble can be a classical thermal ensemble, a Bose-Einstein condensate or a Fermi-degenerate gas. The latter two ensembles lie in the regime of high phase-space density typically at ultra-cold temperatures and usually referred to as quantum degenerate gases [14, 19, 20, 21]. Due to the high degree of overlap of the matter waves of the individual atoms, these ensembles are collectively sensitive to local perturbations such as scattering events and external electric and magnetic fields. A single collision with an extraneous particle or a photon can potentially destroy the quantum degeneracy of the whole system. For the same reason, the detection of atoms in such ensembles has to be done indirectly thus increasing the technical complexity. In contrast, generating a classical thermal ensemble of atoms is technologically simpler and temperatures of the order of a 100μK are feasible. We choose a very established technology, namely the magneto optical trap (MOT), to cool and trap atoms into a thermal cloud [22]. A cold thermal cloud of atoms in a MOT is a more robust system for studying collision phenomena at low energies that are not specifically related to the quantum statistics and non-local correlations of the atoms. The presence of small external fields such as those of the ion trap and the collisions with ions do not destroy the nature of

the ensemble and a direct observation of the scattered light from the atoms is possible.

The most efficient way of trapping ions is by forces that act upon its charge. The force can be either due to electric or magnetic fields. By Earnshaw's theorem, a purely static electric field configuration cannot be used to confine an ion. Depending upon the type of force used, the technology for trapping of ions broadly falls into two categories namely Paul traps and Penning traps [23]. In a Paul trap, a combination of static and time-varying electric fields is used to dynamically trap the ions. Different electrode shapes and voltage configurations are used depending upon the desired properties of the experiments. In a Penning trap, a static homogeneous magnetic field (of the order of a Tesla) is used in combination with a static electric field to confine the ions. The Penning trap is the trap of choice in many experiments involving precision measurements of mass and g-factors of ions and electrons. [23]

In order to achieve the full functionality of trapping the atoms in spatial overlap with the ions, the ion trap design in our experiment does not, in general, conform to the conventional designs. So it becomes essential to carefully design the system and perform numerical simulations of the trapping parameters to determine the valid regimes of effective ion-trapping. This chapter describes in detail the mechanical design of the ion trap, the numerical simulations that validate the design and the hence determined ion-stability diagrams.

2.2 Trap design

2.2.1 General considerations

The design goal of the ion-trap is to achieve confinement of Rb^+ ions with a provision to also accommodate relatively heavy positively charged ion species like K^+, Cs^+ and Ca^+ and their associated molecular ions. The technology

of choice for confining the cold atoms in spatial overlap with the ions is the Magneto-Optical Trap (MOT). To this end, the ion-trap should have high solid angle of optical access to allow the MOT cooling and repumper beams. The MOT requires a quadrupolar gradient magnetic field of modest magnitudes ($\sim$ 10Gauss/cm). The system has to be compact so that currents in the coils that generate this magnetic field are small to avoid elaborate cooling apparatus. The presence of any other strong magnetic field would shift the zero of this quadrupolar field out of the capture region thus compromising the operation of the MOT. Hence using constant magnetic fields to confine the ions as in Penning traps is ruled out. The magnetic fields required in Penning traps is quite high ($\sim$ 1T) and this would only increase the complexity of the system with issues like magnetic field stability, limited optical access and magnetization of the vacuum chamber components. This means that the ions have to be confined by a suitable combination of time-varying and static electric fields. A widely used ion-trap geometry that, in principle satisfies these requirements is the linear Paul trap. This general trap geometry consists of four parallel quadrupole electrodes which are fed with a time-varying voltage to achieve radial confinement and two end-electrodes which are biased with a positive DC voltage to effect axial confinement. This geometry also has the added advantage that the RF node is a line along the axis of the ion trap. The detection of the ions also needs to be considered while designing the ion trap geometry. We are mostly interested in the ions derived from the Group 1 elements in the periodic table. These ions have a closed shell electronic configuration. Therefore the first the electronic transition wavelengths are deep in the ultraviolet or the X-ray region of the electromagnetic spectrum. Hence it is not practical to optically detect or laser cool the alkali ions. In the absence of optical detection, the other option is to detect them on a charge-particle detector. The idea is to steer the ion that is initially in the ion trapping region onto an external detector where it can be detected on impact. In the process, we should also ensure minimal loss of

ions. When the end-electrodes are not biased, the linear quadrupole rods act as a mass-filter and provide a radially confining "track" for extracting the ions along the central axis. With this detection strategy, the end-electrodes must allow the ions to pass through. Hence the end-electrodes were designed to be hollow cylinders. The distance between the end-electrodes has to be such that four of the MOT beams have to be accommodated to orthogonally intersect at the centre of the ion trap. Also the spacing between adjacent quadrupole electrodes and their diameter have to be designed such that the the MOT beams can pass through. The whole ion-trap has to be immune to stray magnetic fields, eddy currents, must be thermally stable, mechanically rigid and at the same time ultra high vacuum (UHV) compatible. The system of electrodes must also have a high degree of alignment with respect to each other and to the rest of the experiment. The above considerations determine the geometric structure and the materials used in the construction of the ion trap.

2.2.2 The mechanical design and construction

The platform for mounting the ion trap is a custom-manufactured vacuum chamber from Kimball Physics (MCF600-SHD20000.16). This is illustrated in Fig. 2.1 along with the co-ordinate axes. This chamber is in the form of a flat cylinder and consists of sixteen radial ports in addition to the top and bottom ports. This chamber has the advantage that the magnetic coils required for the magneto-optical trap can be placed outside of vacuum but almost flush with the top and bottom viewports and the distance between the coils is very small hence enabling the generation of the required magnetic field gradients with minimal current. This also avoids the complication of water-cooling of the coils since it runs on a current of a few amperes. The centres of the ion trap and the MOT have to coincide with the centre of the chamber and also the axis of the ion trap has to be coincident with the axis of one of the radial through-ports of the

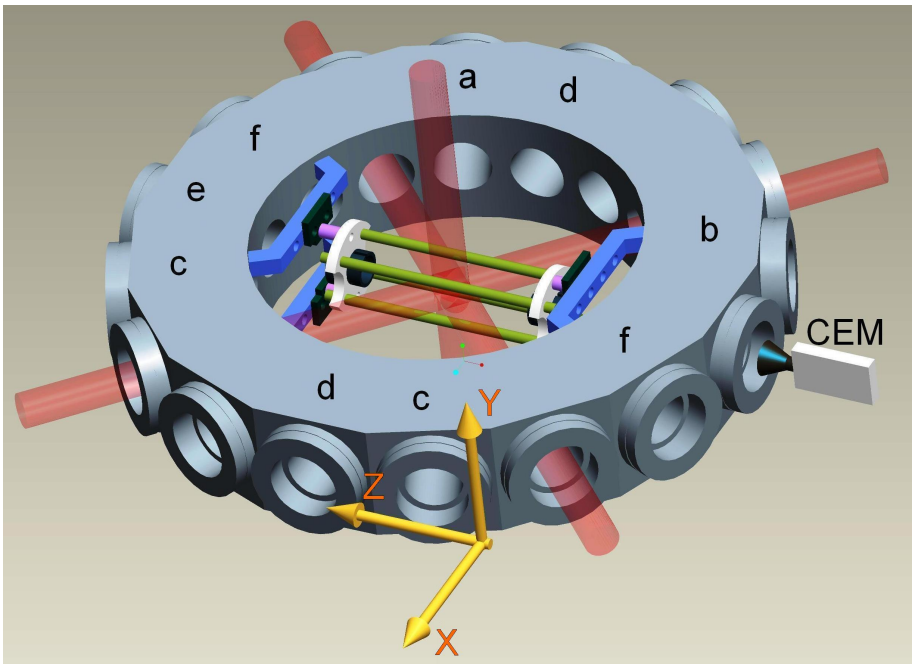

Figure 2.1: Experimental Schematic: Schematic diagram of the hybrid, ion-atom trap, within the experimental chamber. The diagram is not to scale. The ion trap axis is oriented along the z-axis. The magnetic field coils for the MOT (not shown) are external to the vacuum system, mounted symmetrically from the origin coaxial with the y-axis. A CEM for ion detection, is mounted coaxial with respect to the ion trap axis, in the -z direction from the origin. The horizontal MOT beams intersect the z-axis, at the origin, with 45 and 135 degree angles. The vertical beam intersects this arrangement orthogonally. The ports are labelled to illustrate the relative positions of the various components of the experiment as follows. (a) alkali atom dispensers, (b) the blue light source, (c) MOT imaging and fluorescence measurement, (d) Nd:YAG ionization ports, (e) the vacuum pump connection, and (f) feedthroughs.

chamber.

The four quadrupole rods each of diameter 3mm and length 71mm are machined out of SS304. The ends of each rod are threaded for a length of 3mm. The axis to axis spacing between adjacent rods was designed to be 13mm. This relative alignment between the rods is maintained by two insulating disks of thickness 3mm and diameter 25.4mm that have four holes each to accommodate the rods with a slide fit insertion. These are machined out of Macor® glass ceramic (RS: 158-3118). The ceramic disks are fixed onto the chamber with the help of a few coupling elements and groove grabbers (Kimball Physics: MCF600-GG-CR04-A). The groove grabbers have a slot which can be tightened to latch on to grooves that run along the inner rims of the flat-cylindrical chamber. The quadrupole rods are fixed onto the ceramic disks by nuts fastened on both their threaded ends. The tightening force of the coupling of the ceramic disks onto the chamber pulls them away from the centre of the ion-trap and the tightening force of the nuts on the ends of the quadrupole rods pushes them towards the centre. This, when done carefully, can give a very good quality of self-centering of the entire ion trap assembly. This also ensures that the ion trap centre is coincident with the centre of the chamber, within the limits of the machining precision. The only remaining degree of freedom is the angular position of the ion trap axis with respect to the chamber's ports. This angular alignment is done carefully with a graph sheet referenced to the chamber's outer surface. The relative alignment between quadrupole rods is initially maintained by custom-made jigs before securing the whole assembly. This gives an added level of alignment accuracy. The end-electrodes are machined from SS304 in the shape of hollow cylinders. Each cylinder has a slit of width 1mm along its length (such that the cross-section is not a full ring) to avoid eddy currents that would be generated by the time-varying fields of the ion trap if the loop was full. These end-electrodes are held by a push-fit arrangement into central holes in the ceramic disks described above. The ceramic disks are cut away on their sides to

accommodate the radial MOT laser beams. Pure uncoated copper wires with their surface freshly rinsed with hydrochloric acid are used to make all the electrical connections in the chamber. Small segments are cut out of a glass capillary tube and strung all along the length of the wires. These glass "beads" give good electrical insulation, can resist high temperatures during bake-outs and also due to the segments being small, the ability to pump the volume inside them is not compromised.

For the detection of the ions, we chose a channel electron multiplier (CEM) which can give a current pulse at its output whenever an ion impinges on its sensitive area. A micro-channel plate (MCP) could as well serve the purpose, with the added advantage that even the spatial point of ion incidence can be detected with suitable anode-encoding. But owing to the small size of our system and also the relatively larger "dead time" of the MCP, we chose to detect the ions with a CEM. Also, a smaller dead time is a better option when a large number of ions are to be detected with sufficient time resolution within a small time window. The CEM (Dr.Sjuts: KBL-10RS) is compact and fits into a conical reducer nipple which is attached to the main chamber. There is sufficient clearance between the funnel of the CEM, which would be biased at a high voltage, and the chamber-reducer assembly, which is to be maintained at ground potential.

The components mentioned above are labelled in Fig. 2.1. The mechanical designs for each of these components with the detailed dimensions is given in appendix A.

2.3 Numerical simulation of the trapping

The design of the ion trap described above is quite different when compared to the conventional linear Paul trap. Some of the significant deviations are: (i) The diameter of the quadrupole electrodes is very small compared to their spacing.

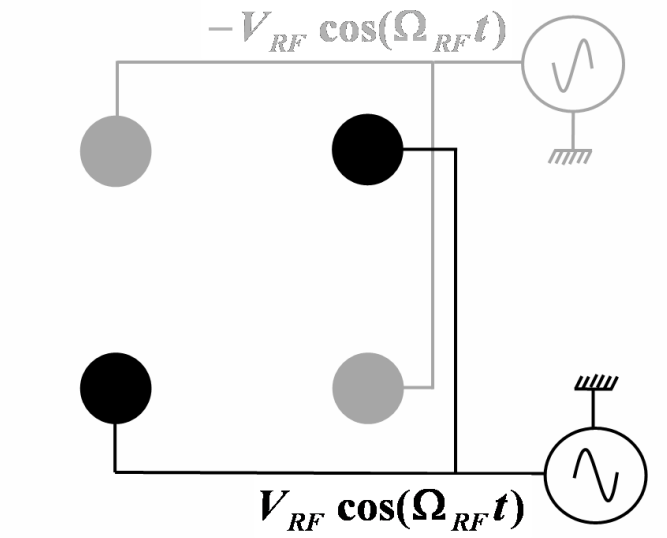

Figure 2.2: The biasing scheme for the quadrupole rods illustrated in cross-section view. The drive RF sinusoidal voltage of equal amplitude is applied on all the four electrodes. The voltages on diagonally opposite electrodes are in phase and adjacent electrodes are 180° out of phase. The end-electrodes (not shown) are biased with a positive DC voltage to achieve Z-axis trapping of positive ions.

This means that the potential in the X-Y direction has higher order components in addition to the quadrupolar component. (ii) The spacing between the end-electrodes is quite large, giving a relatively shallow Z-axis trap depth.

2.3.1 The potential

To validate the feasibility of trapping Rb^+ ions in this trap, we simulate the motion of a single ion in a potential corresponding to the proposed ion trap operating point. The trapping is effected by biasing the quadrupole rods as shown in Fig. 2.2. The XY potential is a saddle at any given instance of time, as plotted in Fig. 2.3. The end-electrodes are maintained at a positive DC potential. As time progresses, the applied time-varying voltage with a phase difference of π between adjacent quadrupole electrodes gives a rotating saddle in any plane parallel to the XY plane. This results in a dynamic trapping of the ion in the X-

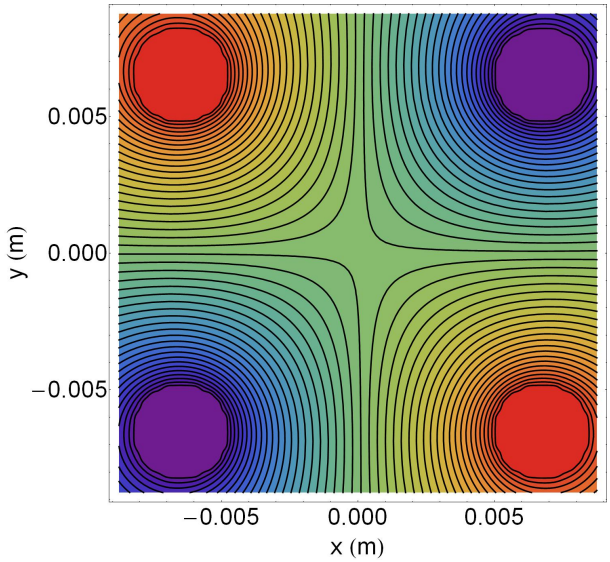

Figure 2.3: A contour plot of the numerically solved potential in the XY plane for our ion trap geometry. The discrete potential array is first solved in Simion 7 and then interpolated in Mathematica. The circular regions of uniform potential correspond to the cross-section of the quadrupole electrodes of the trap.

Y directions in a particular range of amplitudes and frequencies of the applied voltage waveform. The ion motion in the X-Y directions comprises of a macromotion component and a small micromotion component. Close to the central axis of the trap, the time-averaged force experienced by the ion can be approximated by a force corresponding to a static secular harmonic potential. The ion oscillates in this "pseudo-potential" at the frequency of the macromotion oscillation. The potentials at a given instant of time are obtained by solving the Laplace equation for the boundary conditions corresponding to the voltages on the electrodes.

These potentials are calculated in the software package Simion 7. Here we briefly describe the computational procedure. We refer the reader to the Simion 7 manual [24] for more details about the package. The geometry of the electrodes and their respective voltages are defined in a geometry file (.GEM file). All the conductors in the vicinity of the ion trap have to be incorporated in order to get the correct values of the numerical potential. The three dimensional

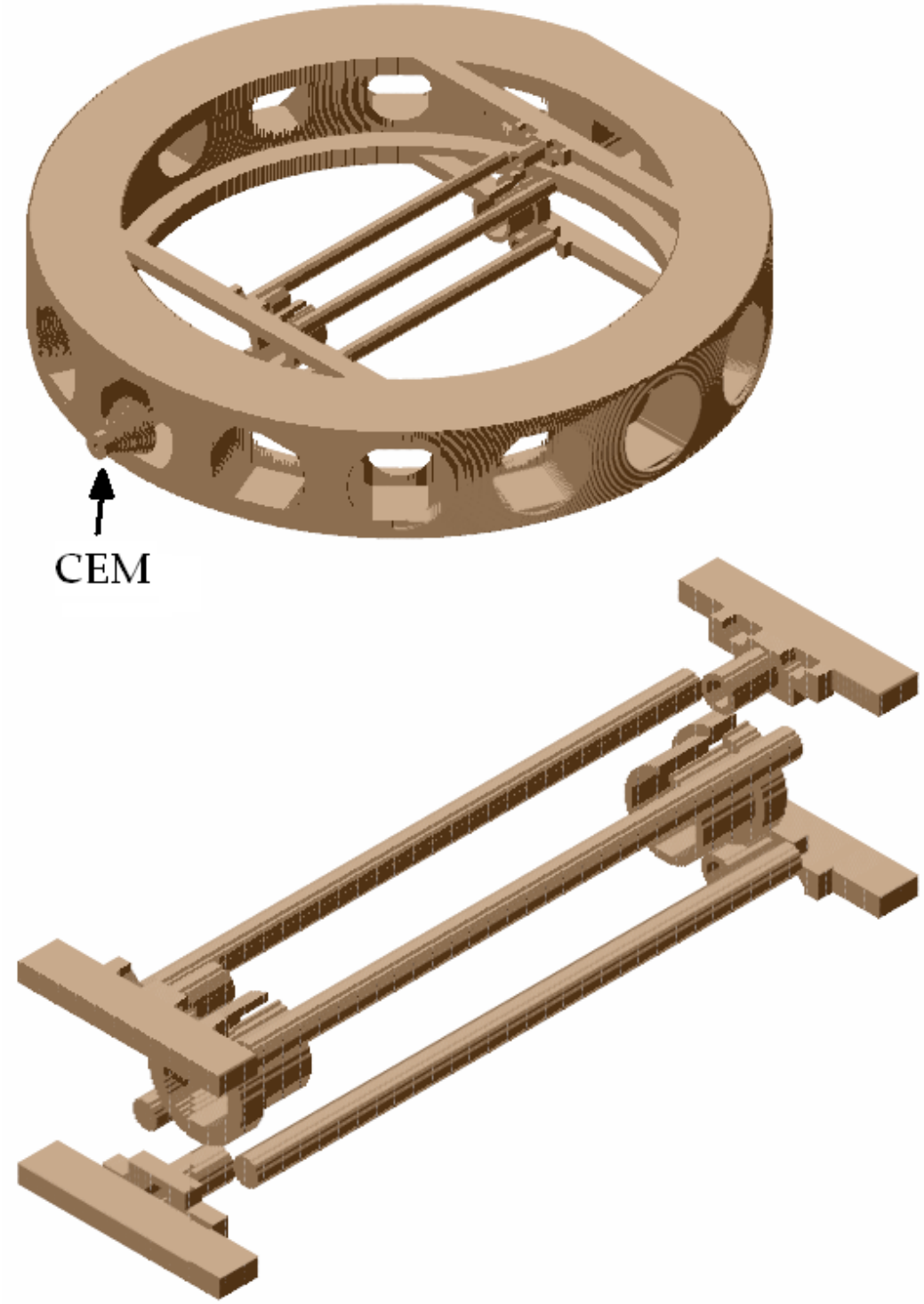

Figure 2.4: The Simion 7 rendering of the ion trap geometry with all the other conductors in the vicinity is shown in the perspective view. The diagram on top shows the full chamber with the CEM detector. The diagram at the bottom is a zoomed in segment showing only the ion trap assembly.

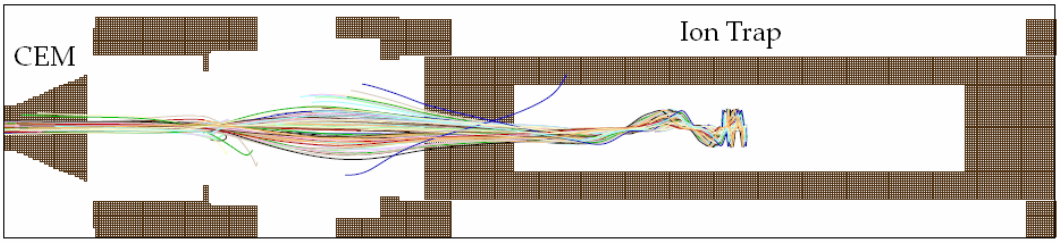

Figure 2.5: The profile view of a section of Fig. 2.4 including the CEM detector is shown. In this PA, the loci of the trajectories of multiple ions trapped for a finite time and then extracted onto the detector is also shown. The different ion trajectories are shown in different colours.

perspective views of the geometry of the ion trap is rendered in Simion 7 as shown in Fig. 2.4. The basic numerical entity in Simion 7 is a three-dimensional array representing the discretized version of the entire trapping region called as a potential array. A potential array (PA) for the given electrode-geometry is generated and a modified Runge-Kutta 4th order method is used to numerically solve for the potential from the Laplace equation in Simion 7. This process of solving for the exact potential starting from an initial array containing only the potentials of the electrodes is called refining of the potential array. A static interpolated potential array for our ion trap geometry is illustrated in Fig. 2.3. Time varying voltages are treated in two different ways: (i) Using the Simion fly'm feature and (ii) Superposition potential arrays separately.

Using fly'm:

In the geometry file, different electrodes are assigned voltages as 1V, 2V,... etc.. irrespective of the actual voltage to be simulated. Now the potential array for this is refined and saved as a *.PA# file. This PA# file is loaded as a new potential array and refined again. Simion generates and saves a separate potential array for each electrode defined as 1V, 2V, etc.. as *.PA1, *.PA2,... respectively and an additional *.PA0 file which is meant for dynamically storing the resultant array combining all these time-varying arrays. The time-varying voltages

on the individual electrodes can be incorporated by writing a *.PRG program file of the same name as the *.PA0 file. Alternatively, a simpler, higher level *.SL program can be written and compiled into an equivalent low level *.PRG program. Whenever the PA0 file is loaded in the "view" section of Simion 7, the corresponding PRG file is also loaded. The feature "Fly'm" will automatically identify all the variables defined in the program such as the various amplitudes and frequencies just before execution. Also, the time-varying voltages on each electrode is automatically incorporated as defined in the *.PRG program. The trajectory of the ion(s) can be solved for a stipulated amount of time and also recorded. Special events on the ion trajectory such as crossing of a plane, ion splatting and so on can also be recorded. The mass, charge, initial position, initial velocity and other parameters of each ion can all be defined in a separate *.ION file with the stipulated format. A typical set of loci of the trajectories of many ions generated using the Fly'm feature is illustrated in Fig. 2.5.

Separate superposition of PA's:

In this method, a separate geometry file is made for each electrode with only that particular electrode set to 1V and all the others kept at ground potential. The geometrical features are the same in all the files but only the voltages declared are different. These geometry files are individually loaded in to Simion 7 and a *.PA file is generated, refined and saved. From here on, the superposition of these voltages is done in a different programming language. The advantage of isolating the processes of PA refining and superposition is that external fields and forces other than that of the ion-trap electrodes can also be included into the trajectory calculations. For instance, we could easily incorporate the force on the ion due to the MOT magnetic field using this method. We used Mathematica to interpolate the potential array corresponding to each electrode and form a grand superposition. For example, one diagonally opposite pair of quadrupole rods are clubbed as one electrode and set to 1V in the file

labelled as q1.GEM, the other pair as q2.GEM, the end-electrodes as ec1.GEM and ec2.GEM and so on. A potential array for each *.GEM file is generated, refined and stored as q1.PA, q2.PA and so on. Now in Mathematica, these potential arrays are converted to a form identified by the program and interpolated to obtain $V_{q1}(x,y,z)$, $V_{q2}(x,y,z)$ and so on. These interpolated functions are weighted by their respective time-varying voltages and superposed into a total potential $V_{tot}(x,y,z,t)$defined as

$$V_{RF}\left[V_{q1}(x,y,z) - V_{q2}(x,y,z)\right]\cos\Omega_{RF}t + V_{ec1}V_{end1}(x,y,z) + V_{ec2}V_{end2}(x,y,z).$$

2.4 Stability diagrams

It is very important to determine the range of voltages and frequencies over which the ion can be stably trapped. These are the standard stability zones. Since our ion trap design is geometrically different compared to the standard linear Paul traps, we can expect the stability diagrams also to be quite different. First we will briefly review the stability diagram of an ideal linear Paul trap.

2.4.1 The ideal stability diagram

The ideal quadrupolar potential of a linear Paul trap with rods having hyperbolic cross-section in the X-Y plane is of the form,

$$\phi(x,y,t) = \frac{x^2 - y^2}{2R_0^2}(U_{DC} + V_{RF}\cos\Omega_{RF}t) \tag{2.1}$$

where R_0 is the radial distance of the electrode from the centre of the trap, V_{RF} is the amplitude of the radio frequency voltage, Ω_{RF} its frequency and U_{DC} is a DC offset for the radiofrequency voltage. By making the substitutions,

$$a_x = -a_y = \frac{4QU_{DC}}{m_I\Omega_{RF}^2R_0^2}\,, \quad q_x = -q_y = \frac{4QV_{RF}}{m_I\Omega_{RF}^2R_0^2}\,, \quad \tau = \frac{\Omega_{RF}t}{2} \tag{2.2}$$

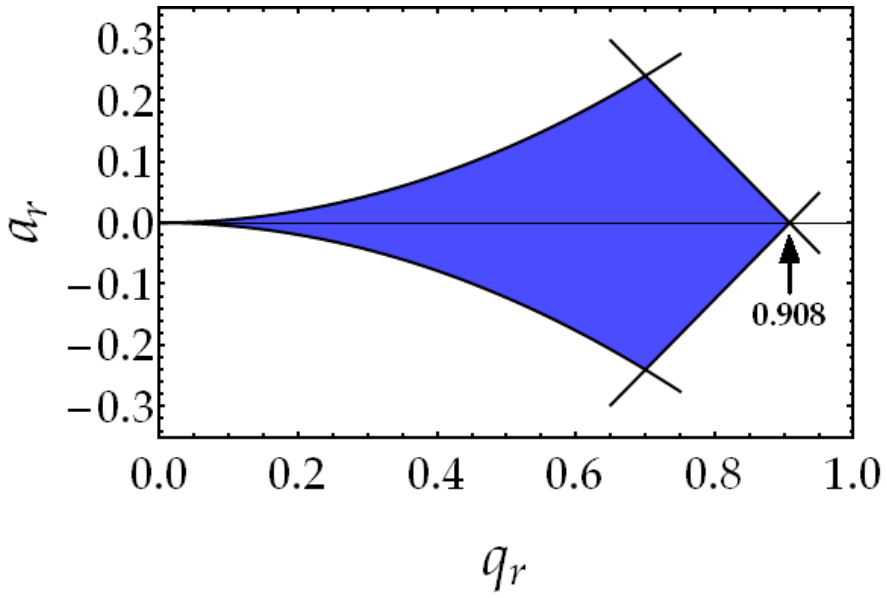

Figure 2.6: The first stability region in the radial direction for an ideal linear Paul trap. This region terminates at a value 0.908 of the dimensionless parameter q_r.

the motion of an ion of mass m_I and charge Q in this potential can be described by the Mathieu equations

$$\frac{d^2x}{d\tau^2} + (a_x + 2q_x \cos\Omega_{RF}t)x = 0\,, \quad \frac{d^2y}{d\tau^2} + (a_y + 2q_y \cos\Omega_{RF}t)y = 0. \tag{2.3}$$

The Mathieu equations inherently have regions of a_x and q_x where solutions are real and non-divergent. These are designated as the first stability region, second stability region and so-on. The first stability region for an ideal potential of the form of Eqn. 2.1 is shown in Fig. 2.6. Since in our trap we will be dealing with mostly $U_{DC} = 0$, the relevant region of the stability diagram is the $a = 0$ axis. On this axis, the first region of stability starts at $q = 0$ and ends at $q \approx 0.908$. This is consistent with the definition of R_0 in the potential.

2.4.2 Scaled stability diagram

In our trap, as discussed in the design section, apart from the fact that the rods are circular in cross-section, the spacing between the rods is much larger than the diameter of the rods. This means that the actual trap potential in the X-Y

plane cannot be not fully described by the form of Eqn. 2.1. The definition of R_0 also cannot be taken as the radial distance of the electrodes from the centre. To determine the actual stability diagram in the X-Y plane, we simulated the ion's trajectory on a computer for different trapping parameters. The potential was calculated as described in section 2.3.1 using the second method, i.e. superposing the different PA's in Mathematica. Now, the total potential $V_{tot}(x, y, z, t)$ is an interpolating function object in Mathematica, which can be treated like any standard function. The NDSolve function is used to numerically solve for the differential equations of motion for the ion given by

$$\begin{aligned} m_I \frac{d^2x}{dt^2} &= -Q\frac{\partial}{\partial x}V_{tot}(x, y, z, t) \\ m_I \frac{d^2y}{dt^2} &= -Q\frac{\partial}{\partial y}V_{tot}(x, y, z, t) \\ m_I \frac{d^2z}{dt^2} &= -Q\frac{\partial}{\partial z}V_{tot}(x, y, z, t) \end{aligned} \tag{2.4}$$

Since the frequency of the time-varying field is quite low, we consider the ion's motion in a quasi-electrostatic framework, wherein the electromagnetic nature of the oscillating field is neglected. We solve for the motion of the ion for typically a few hundred RF cycles. A stability condition is imposed on the ion's trajectory in this time interval where, if the ion goes outside a certain bounding sphere of radius r_{bound}, it will be considered an unstable trajectory. The value of r_{bound} is decided such that it represents a realistic stability condition and at the same time maintaining computational simplicity. The initial position of the ion in the X-Y plane is randomly assigned to lie in a region very close to the origin and the initial velocity is taken to be zero. The initial position and velocity in the Z-direction is assumed to be zero. Also, the voltage on the end-electrodes is assumed to be zero. The ion's trajectory is calculated for different values of V_{RF} and U_{DC} to span the entire region of stable trapping with $\Omega_{RF} = 400$kHz. If we take the radial distance of the electrode from the centre as the value R_0, which for our trap dimensions is ≈ 7.69mm, the stability region ends at $q \approx 0.56$ as

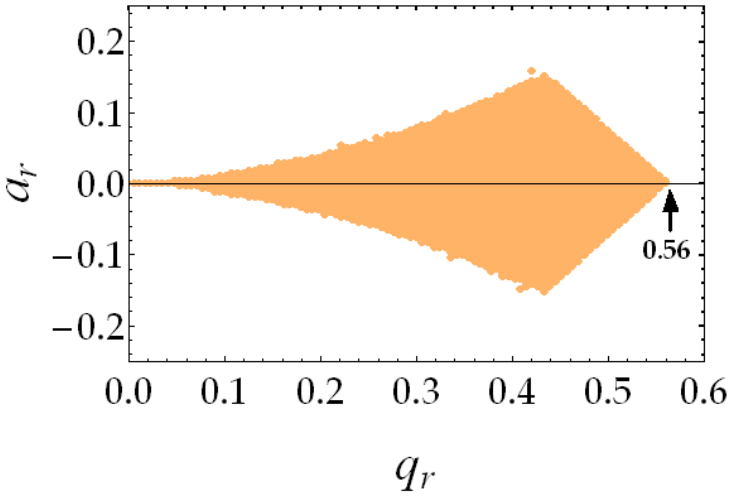

Figure 2.7: The first stability region in the radial direction for an ideal linear Paul trap. This region terminates at a value 0.908 of the dimensionless parameter q_r.

shown in Fig. 2.7. To make this terminate at the value $q = 0.908$ as prescribed by the Mathieu stability criterion, the value of R_0 has to be scaled accordingly to give $R_0' = 6.04$mm. Physically, this is the radius at which the ideal quadrupolar potential defined in Eqn. 2.1 would reach the voltage that is applied on the electrodes. The ideal and the actual potentials match near the central axis but deviate as we go radially way.

Stability diagram with magnetic field

The gradient magnetic field $\mathbf{B}(x,y,z) = B_x(x,y,z)\hat{x} + B_y(x,y,z)\hat{y} + B_z(x,y,z)\hat{z}$ required for the MOT is calculated for our configuration (as discussed in section 3.2.2) and the stability diagram in the X-Y plane is determined with the Lorentz force on the ion due to the magnetic field also incorporated into the equation of motion as

$$\begin{aligned}
m_I\frac{d^2x}{dt^2} &= -Q\frac{\partial}{\partial x}V_{tot}(x,y,z,t) + Q(\frac{dy}{dt}B_z(x,y,z) - \frac{dz}{dt}B_y(x,y,z)) \\
m_I\frac{d^2y}{dt^2} &= -Q\frac{\partial}{\partial y}V_{tot}(x,y,z,t) + Q(\frac{dz}{dt}B_x(x,y,z) - \frac{dx}{dt}B_z(x,y,z)) \\
m_I\frac{d^2z}{dt^2} &= -Q\frac{\partial}{\partial z}V_{tot}(x,y,z,t) + Q(\frac{dx}{dt}B_y(x,y,z) - \frac{dy}{dt}B_x(x,y,z))
\end{aligned} \tag{2.5}$$

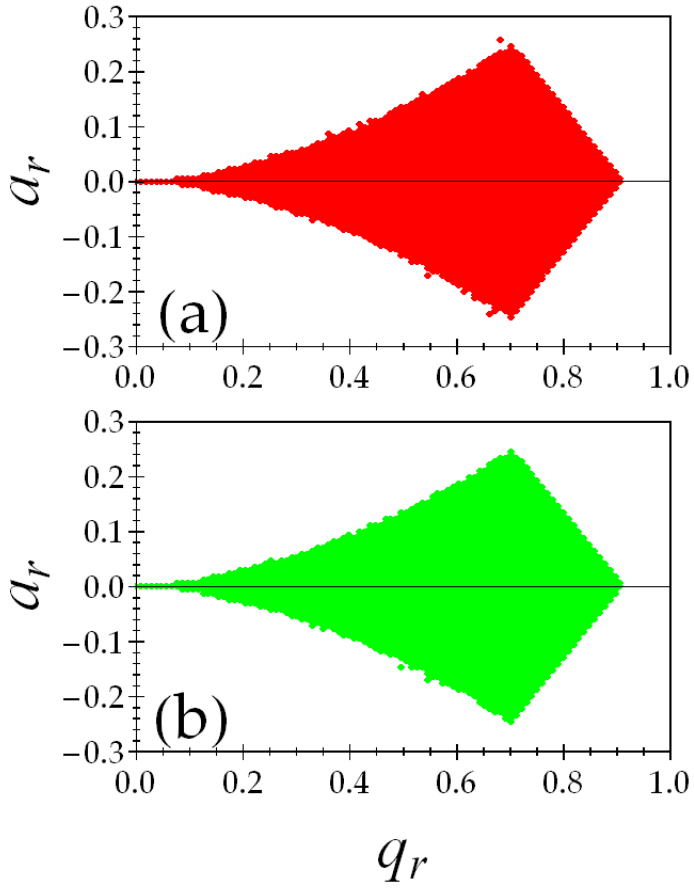

Figure 2.8: The calculated $a_r - q_r$ stability diagram for ions in the trap potential. A filled point at each $\{a_r, q_r\}$ indicates a stable trajectory at that operating point and these points constitute the region of stability. (a) shows the points of stable trajectories in the absence of the magnetic field and (b) in the presence of a gradient quadrupolar magnetic field of 24 Gauss/cm. The regions of $a_r - q_r$ space that support trapping of an ion in the two cases are almost identical.

The scaled stability diagrams with $R_0' = 6.04$mm in the presence and absence of the magnetic field are shown in Fig. 2.8.

For the full three-dimensional potential, the harmonic potential created by the end electrodes leads to fringing of the XY potentials near the end electrodes introducing a coupling between the XY and Z components. Near the centre, it is still a good approximation to decouple the radial and axial motions and treat them independently.

The numerical solution of trajectories using the interpolated potentials described above is highly time-consuming. In certain simulations such as the ones described in Chapter 5, we can approximate the full three-dimensional potential of our trap by an analytical expression of the form

$$U(x,y,z,t) \approx \frac{V_{RF}}{2R_0^2}(x^2-y^2)cos(\Omega_{RF}t) + \frac{\kappa V_{ec}}{Z_0^2}[z^2 - \frac{1}{2}(x^2+y^2)] \qquad (2.6)$$

A fit of the above analytical potential to the numerically calculated potential yields $R_0 = 5$ mm. With $Z_0 \equiv 25.5$ mm the geometric parameter $\kappa \approx 0.11$ is calculated for the trap. The sense of the x and y axes in this expression is rotated by 45° from those shown in Fig. 2.1 with the z-axis remaining the same.

CHAPTER 3

Experimental Setup

The confinement of ions and atoms in spatial overlap requires carefully worked protocols for implementing the design described in Chapter 2, creating the ion and atom species, loading their respective traps, diagnosing them and performing the experiments that probe the ion-atom interactions. In this chapter we shall describe in detail the construction and operation of the experimental set-up as a whole. We discuss the construction of the vacuum system, the laser systems involved and their associated electronics, the magneto-optical trap and its properties, the characterization and operation of the ion trap and detection of ions and the generic sequence of performing an ion-atom experiment.

3.1 The vacuum system

Our aim is to pump the main vacuum chamber described in Chapter 2 to a pressure of less than 10^{-11}mBar which is usually categorized to be in the ultra-high vacuum (UHV) regime. To create this vacuum and measure the pressure many other components and instruments have to be incorporated in the vacuum system. A schematic diagram of our set-up is shown in Fig. 3.1. The whole system is mounted on a vibration isolation optical table with tuned damping (Newport: RS4000). The entire vacuum system is based on the conflat technology, wherein every joint between different components is sealed by tightening flanges such that their corresponding knife-edges bite into copper gaskets placed at the joint. All vacuum components are thoroughly washed in a sonicator with soap, distilled water, acetone and methylene in that order to make sure that there is no undesirable substances like grease or oil sticking to the surface. Then they are assembled carefully making sure that no vacuum joint is being stressed by their

weight or any extraneous torques. We use powder-free latex gloves to assemble in-vacuo components. The flanges especially those corresponding to viewports are tightened with the prescribed torque using a torque-wrench. Once the system is fully assembled and tightened, we use four different types of pumps operated in a particular sequence described below, to achieve the required vacuum. The pressure inside the system is measured primarily with an ionization gauge(Varian: UHV-24) shown in Fig. 3.1 and cross-checked with a cold-cathode gauge that is attached to the mouth of the turbo pump during the time of operation of the turbo pump.

3.1.1 Pumping sequence

Roughing and initial turbo operation

The process of attaining a steady state pressure of less than 10^{-11}mBar requires a sequence of steps in which the pressure is progressively reduced according to the range of operation of the appropriate pump. We first use a diaphragm pump to first pump the system to a pressure of about 10^{-1}mBar. This is also called as a "roughing pump". Now in this range, we operate a turbomolecular (turbo) pump to further reduce the pressure to about 10^{-7}mBar. We use a turbomolecular pump (Pfeiffer: TMU 071) that can pump nitrogen at a rate $59l/s$ with its accompanying diaphragm pump (Pfeiffer: MVP 015-2).

Bake-out

At this stage we have to address the issue of outgassing of the components inside of vacuum. Outgassing is a phenomenon where contaminant gases that are trapped on the inner surface of the system start slowly escaping from the surface over time and hence eventually degrade or limit the ultimate vacuum. The chief gases that are usually involved are water vapour which is adsorbed on the surface due to the humidity in the atmosphere and hydrogen which gets

trapped in the bulk of stainless steel during its manufacturing process. To eliminate these gases, the outgassing rate has to be temporarily accelerated while still pumping the system. A standard way to do this is to heat the entire system to a high temperature so that the vapour pressure of the contaminant gases in the vacuum system is increased and they are quickly pumped out. This process of heating is commonly referred to as a "bake-out". To eliminate the hydrogen, the temperature of the bake-out is around 400°C and for the water vapour it is about 150°C. Since in our system there are components which cannot withstand very high temperatures, we perform only the bake-out at 150°C for a steady period of at least 48hours exclusive of the intervals where we gradually raise and lower the temperature. The turbo pump is kept operational during this entire process. When the system is back to room temperature again, the turbo pump operation is continued till there is no appreciable change in pressure over a long time. The pressure in our system stabilizes at about 10^{-9}mBar within a few days of pumping after the bake-out.

Sublimation pump

The section of tubing labelled as Titanium sublimation pump in the front view of Fig. 3.1 contains Titanium filaments (Varian). These filaments are heated for a few minutes by passing high current pulses $\sim$ 50A and the inner surface of the tube gets coated with a film of the sublimated Titanium. Because the Titanium is a getter, any gas molecules that collide with the surface will form a stable compound and stick to the surface. After a few cycles of sublimation over a period of a few hours, the pressure in the system is reduced by nearly two orders of magnitude. Throughout this process, the turbo pump is still operational.

Ion pump

The final stage in the vacuum is to fully transfer the operation to an Ion-pump (Varian: VacIon Plus 919-1210). The ion pump can achieve ultimate pressures of

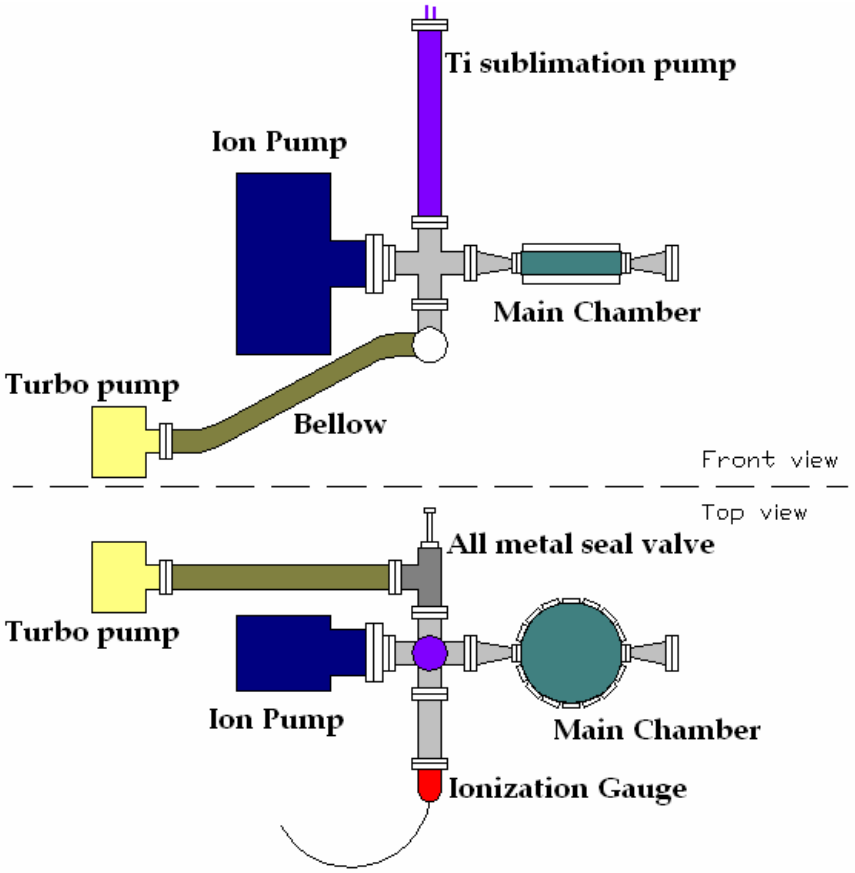

Figure 3.1: The schematic of the vacuum system. The entire system is based on conflat technology. Only the bare system without the mounting is shown. The different components are carefully mounted and secured on an optical vibration isolation table.

about 10^{-11}mBar. While the turbo pump is running and the sublimation pump has already been fired, the ion pump is switched on. This initially introduces a small increase in the pressure. Once the pressure equilibrates, the turbo pump is decoupled from the system by using an all-metal seal valve shown in the top view of Fig. 3.1. Now the system is being pumped only by the Ion pump and this is the steady point of operation for all the experiments. The option of firing the sublimation pump again is always available if we are required to further reduce the pressure.

3.2 The Magneto Optical trap

The Magneto-Optical trap (MOT) is our device of choice to confine the Rubidium atoms in our system. We use the standard configuration of six independent laser beams that intersect at the centre of the combined trap along the six cartesian directions. The frequency of the lasers have to be tuned and stabilized to specific values to effectively cool and trap the atoms. The point of intersection of the laser beams coincides with the centre of a quadrupolar magnetic field produced by a pair of anti-Helmholtz coils. Below, we first describe the Laser systems used and the features of the magnetic coils. Then we give the details of the operation of the MOT including the diagnostics for the number of atoms and their density distribution.

3.2.1 Lasers

The lasers required for the MOT and all the associated apparatus for processing the light are mounted on a separate vibration isolation table (Newport: RS2000). The laser beams for the MOT are a combination of two frequencies of light corresponding to the cooling and repumper hyperfine transitions of the Rubidium D2 series. The fine-structure transition wavelength in vacuum for this series is 780.24nm. The two frequencies are generated by separate external cavity diode lasers (ECDL) in the Littrow configuration and combined in a non-polarizing beam splitter. Fig. 3.2 illustrates the transitions that we use as cooling and repumper. The cooling laser frequency corresponds to a closed-cycle transition from the $5^2S_{1/2}$:F=3 state to the $5^2P_{3/2}$:F′=4 state. When the atom is pumped to the excited F′=4 state of this transition, the dipole selection rules forbid it to decay to any state other than the ground F=3 state. But due to higher order transitions, on an average once in every ten thousand closed cycles, the atom gets pumped to the ground F=2 state. The repumper laser is tuned to the tran-

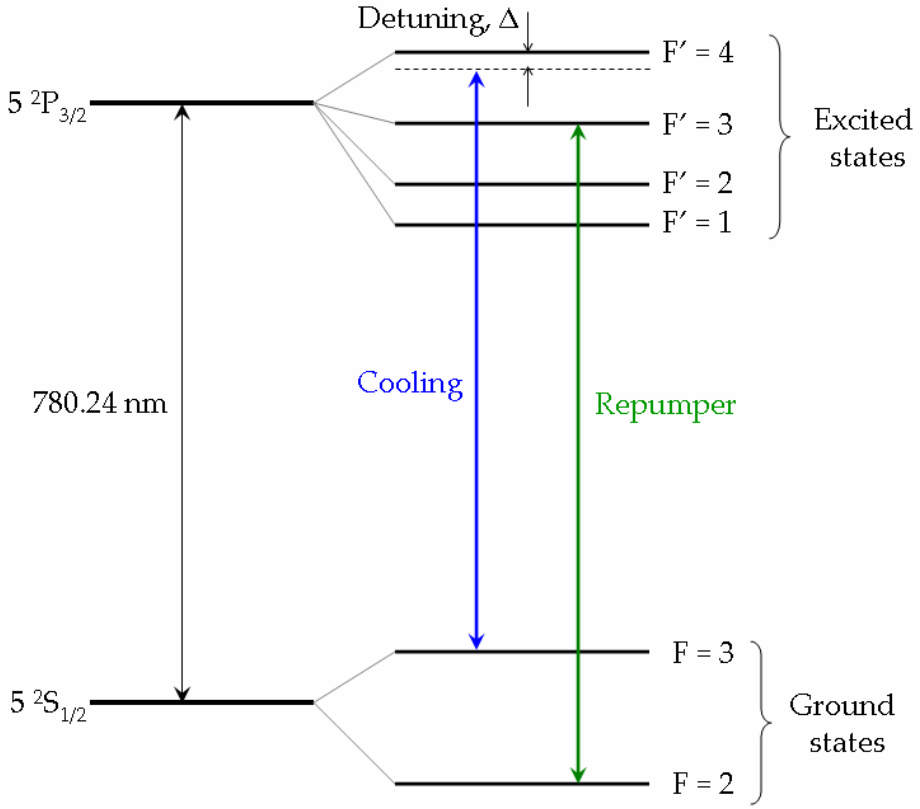

Figure 3.2: The hyperfine splittings of the ground and first excited fine structure energy levels of the valance electron in a ^{85}Rb atom

sition from the $5^2S_{1/2}$:F=2 state to the $5^2P_{3/2}$:F′=3 state. An atom that has found its way into the dark $5^2S_{1/2}$:F=2 state will be excited to the $5^2P_{3/2}$:F′=3 state by the repumper laser. From this state, there is a good chance for the atom to decay into the $5^2P_{3/2}$:F′=3 state and again engage into the cyclic transition. So the repumper laser effectively plugs the leakage of atoms from the cyclic transition.

For the cooling wavelength, we use a home-built ECDL which is schematically shown in Fig. 3.4. It consists of a laser diode (Thorlabs: GH0781JA2C) with an uncoated output facet. This surface reflects back part of the light emitted from the semiconductor junction to form an internal cavity within the diode. The laser diode emits a diverging beam and the light is collimated using an aspheric lens. The diode and the lens are mounted in a collimation tube (Thorlabs: SR9C DB-9). The entire collimation tube is secured onto a brass plate

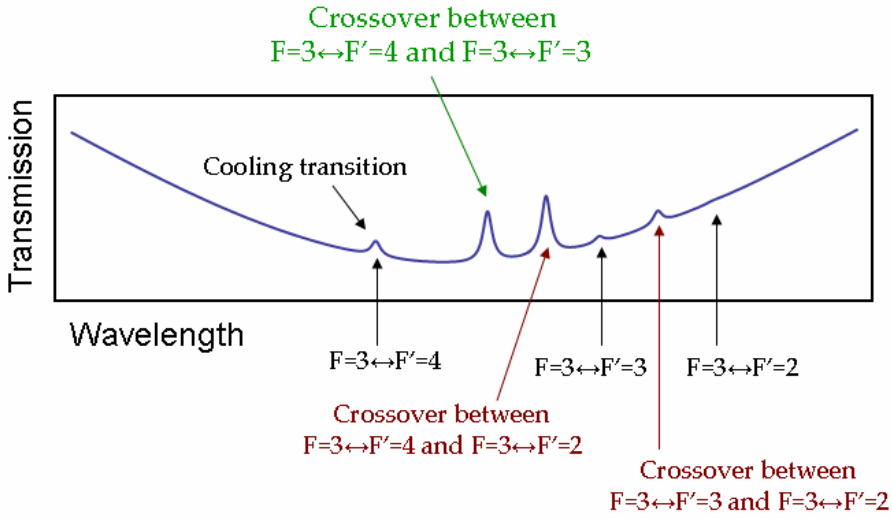

Figure 3.3: The saturated-absorption spectrum of ^{85}Rb shown for the $5S_{1/2}$:F=3↔$5P_{3/2}$:F′ set of lines. The Doppler absorption is seen as a wide Gaussian shape on which the lines are resolved at their natural linewidths. The lines are marked in black and the crossovers are marked in brown. The crossover on which we lock the cooling laser is marked in green.

which is cooled and maintained at a particular temperature from the bottom using a Peltier cooler(Thorlabs: TEC3-6). On the same plate is also mounted a diffraction grating (Thorlabs: GR13-1850) at an angle such that the first order of diffraction is fed back to the laser diode and the zeroth order emerges at roughly a right angle with respect to the incident beam. This creates an external cavity. The grating's angle can be changed by a small amount by the piezo-mechanical element (PiezoMechanik bullet actuator) and hence the length of the external cavity can be varied. With this we can scan across a small range of frequencies typically about a few GHz about the centre frequency. A saturated absorption spectrum is obtained from a Rb glass cell (Triad Technologies: TT-RB-75-V-P) which acts as a reference to tune the laser as desired. We use electronic modules from Toptica Photonics for generating a stable diode current (DCC110), the piezo voltage scanning (SC110), to maintain the diode at a steady temperature (DTC110) and to stabilize the laser to a particular frequency (PDD110 and

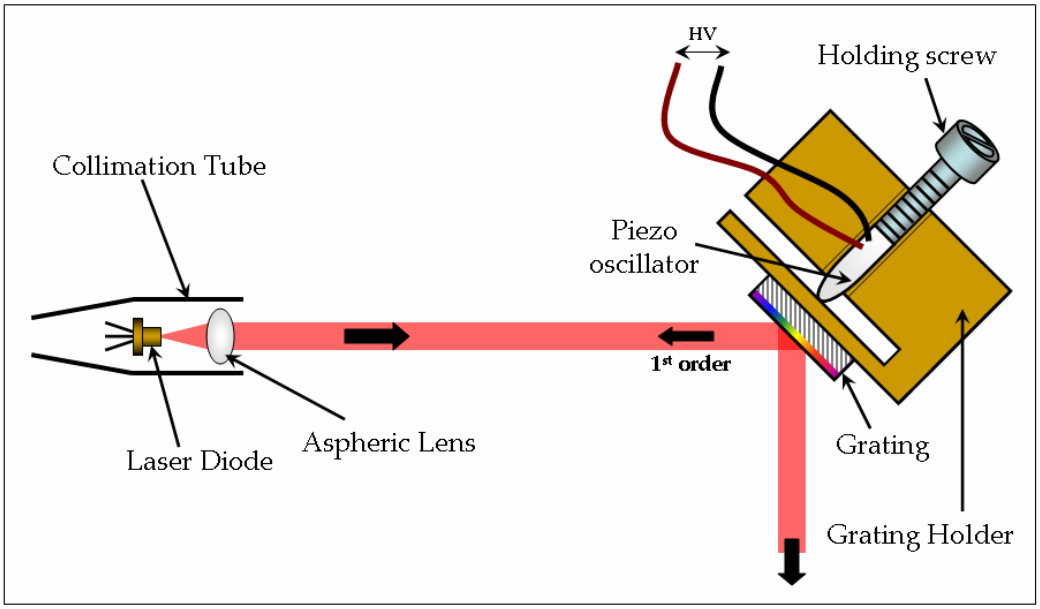

Figure 3.4: The schematic top view of the home-built External Cavity Diode Laser (ECDL). The entire assemble shown above is mounted on a brass plate. The temperature of this plate is regulated by a peltier cooler underneath (not shown) and has the provision for fine adjustment of height and tilt to enable the accurate alignment of the first-order feedback from the grating.

PID110). For the repumper laser, we use a commercial ECDL (Toptica: DL100) in addition to a separate set of all the above mentioned modules.

Frequency stabilization

The lasers described above are subject to drifts in the emission frequency due to various external factors such as small fluctuations in temperature of the diode, mechanical vibrations and electronic thermal drifts. So it is essential to provide an active feedback to the laser to keep it "locked" at a certain frequency. We use the saturated absorption spectrum of Rb to identify the atomic resonances and these provide a reference point for the feedback. A Pound-Drever-Hall system (Toptica: PDD110) is used to generate an differentiated signal of the atomic resonance spectrum. At the top of an atomic resonance, the corresponding differential has a zero-crossing and hence the laser can be fed back such that

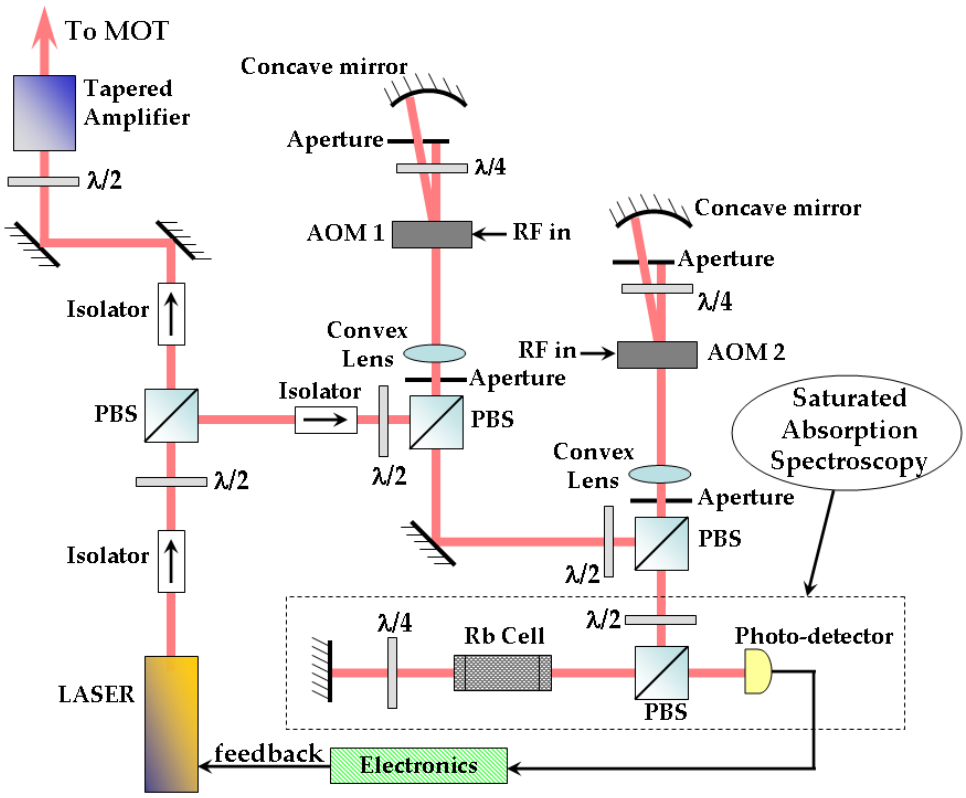

Figure 3.5: The schematic of the setup used to lock the frequency of the ECDL at a specific detuning from an atomic resonance.

the differential is maintained at zero. A proportional-integral-differential (PID) regulator (Toptica: PID110) is used to automatically keep the laser frequency locked to a particular atomic resonance.

Frequency shifting

For the proper operation of the MOT, the cooling laser has to be detuned about 10 to 20MHz red of the cooling transition. But in the method of frequency stabilization described above, it is essential to have an atomic resonance at the particular frequency. To achieve the locking at a frequency detuned from the atomic resonance, we perform a frequency shift operation on a fraction of the cooling laser light power with acousto-optic modulators (AOM) as illustrated in Fig. 3.5. The commonly available AOMs provide a frequency shift of a few hundred MHz with an RF voltage of the corresponding frequency δf being fed

orthogonal to the laser beam direction. The output of the AOM consists of a zeroth order beam which is at the input frequency f and sidebands that are shifted by multiples of the RF frequency ($f \pm \delta f$, $f \pm 2\delta f$ and so on) and emerge at different angles with respect to the incident beam. The AOMs are operated in double pass mode where the first order beam is passed through a quarter wave-plate and reflected back into the AOM using a concave mirror to produce an additional shift resulting in a frequency $f + 2\delta f$. The double-pass beam is out-coupled from the other port of the polarizing beam splitter through which the beam was initially fed in. This method of double pass makes the output beam immune to angular changes as a result of changes in δf. The first AOM (Isomet: 1206C) is operated at $\delta f = 112.5$MHz and the output of this is fed into a second AOM (Isomet: 1205C) which is operated on the -1th order at $\delta f = -90$MHz. This gives a resultant frequency of $f + 45$MHz. A saturated absorption spectrum of the frequency shifted output of the AOM stage is obtained and the laser is locked on the crossover line in this spectrum. The crossover corresponds to the one between the $5^2S_{1/2}$:F=3$\leftrightarrow$$5^2P_{3/2}$:F$'$=4 and the $5^2S_{1/2}$:F=3$\leftrightarrow$$5^2P_{3/2}$:F$'$=3 transitions. This crossover is detuned by 60.5MHz to the red of the cooling transition. When the laser is locked on this crossover, the effective detuning of the laser light is 15MHz red of the cooling transition. In effect we feed back on the master oscillator from the frequency shifted beam. The other fraction of the laser power which does not pass through the AOM stage is used for the MOT. The repumper laser does not require any detuning and is locked on the appropriate resonance line.

Laser power budget and coupling

We couple in a total cooling laser power of about 15mW for the six MOT beams. The repumper power is kept at 3mW. The home built cooling laser gives a power of 100mW and it needs to be mixed with the repumper laser in a 50:50 non-polarizing beamsplitter resulting in a 50% loss. To obtain a clean gaussian

beam profile, we pass both the laser beams through a single-mode optical fiber which has an efficiency of about 50%. After these two operations, the output power is one-fourth of the input power. In addition the fraction of light going to the AOM stage is substantial. In view of the the power budget, we are required to amplify the cooling light power. For this purpose, we use a tapered amplifier (Toptica: BoosTA) which can give a maximum output power of two watts. The output of the tapered amplifier is then coupled through a home built fiber-coupler into a five metre long single mode polarization-maintaining optical fiber (Thorlabs:HB750) and taken to the table on which the vacuum system is mounted. The repumper laser beam does not require any amplification and is directly coupled into a separate fiber. The two beams are combined on the experiment table and this resultant beam is expanded to a diameter of 10mm and split into six equal parts using five sets of half waveplates and polarizing beam splitters and aligned through the appropriate ports of the main vacuum chamber as illustrated in Fig. 3.9. The polarization state of the beams emerging from the polarizing beamsplitters is linear whereas circularly polarized light is required for the MOT. Quarter-wave plates are used to set the appropriate cicular polarization states of the MOT beams with respect to the asymptotic direction of the quadrupolar magnetic field along each beam axis.

3.2.2 Magnetic coils

To create the quadrupolar magnetic field for the MOT, we use a pair of matched coils in anti-Helmholtz configuration. The diameter of the coils is $a = 40$mm and the number of turns in each coil is $n = 100$. The coils are symmetrically and co-axially placed on the top-side and bottom-side of the vacuum chamber with a small gap from the respective viewports. If i_c is the current passing through each coil, the axial magnetic field at a point (ρ, ϕ, z) due to each coil is given in

SI units by

$$B_z(\rho, \phi, z) = \frac{\mu_0 n i_c}{2\pi\sqrt{(a+\rho)^2 + z^2}} \left[\frac{a^2 - \rho^2 - z^2}{(a-\rho)^2 + z^2} \mathcal{E}(m) + \mathcal{K}(m) \right] \tag{3.1}$$

where μ_0 is the permeability of free space, $\mathcal{E}(m)$ and $\mathcal{K}(m)$ are the complete elliptic integrals [25] of the first and second kind respectively with respect to the parameter m which is given by

$$m = \frac{4a\rho}{(a+\rho)^2 + z^2} \tag{3.2}$$

In our experiments, the coils are connected in series and a current of $i_c = 2.8$A gives an axial magnetic field gradient of $dB_z/dz = 12$Gauss/cm. Since the magnitude of the current is quite low, we do not require any additional cooling in the steady state of operation other than the ambient air circulation.

3.2.3 Loading of atoms

The alkali atom reservoir is a Rubidium getter (SAES: Rb / NF / 4.8 / 17FT10+10), which emits the atoms on resistive heating by a few Amperes of current. The MOT itself is loaded from the Rb vapour, which can either be directly emitted by the Rb getter, or alternatively, using desorbed atoms from the walls of the vacuum chamber by a process called Light Induced Atomic Desorption (LIAD) [26]. In the latter method, the chamber is illuminated by a blue light LED (Thorlabs: MRMLED) from a side port, as indicated in Fig. 3.9. The LED illuminates over a wide angle at a central wavelength $\lambda_{LED} = 456.5$ nm and $\Delta\lambda_{LED} = 22$ nm, full width at half maximum. In the presence of the blue LED illumination, alkali atoms are desorbed from the cell walls due to LIAD [26], which is known to increase in efficiency with decreasing wavelength over the visible range [27]. The energy corresponding to a single photon of the blue light is significantly below the ionization threshold for alkali atoms, so it contributes to desorption but not direct ionization. The desorbed atoms are much colder

than the atoms emitted from the resistively heated alkali getter. Unlike the getter, the desorption method recycles the atoms already in the chamber, resulting in better vacuum.

The getter loading method gives a larger vapour density and is used when we require a large number of atoms loaded into the MOT. The getter is kept on for about an hour prior to an experiment so that the vapour density in the chamber reaches a steady state. The loading of the MOT in this case is controlled by switching the cooling and repumper light on or off with an electromechanical shutter (Thorlabs: SH05). When we want to load a smaller number of atoms into the MOT but with better decay time, we use the LIAD method. Here, the BLS can be switched on and off to control the loading and decay of the number of atoms in the MOT. The getter loading is used in the experiments described in Chapter 5 and the LIAD method is used in most of the calibration experiments described in the present chapter.

3.2.4 Detection of the atoms

The atoms that are being cooled in the MOT constantly scatter the laser light in all directions. The optical power from this fluorescence is typically in the range of a few hundred picowatts to a few nanowatts and can be optically imaged onto a low-light detector such as a photomultiplier tube, an APD or a femtowatt detector. This optical signal from the trapped atoms can be used to determine the number of atoms in the MOT and their density distribution.

Spatial filtering

There are a variety of paths through which stray light can get into the detector that measures the atom fluorescence, and offset this sensitive measurement. The main cause comes from the scattering of the resonant cooling and repumper laser light. This means that a lock-in detection will also not yield good results

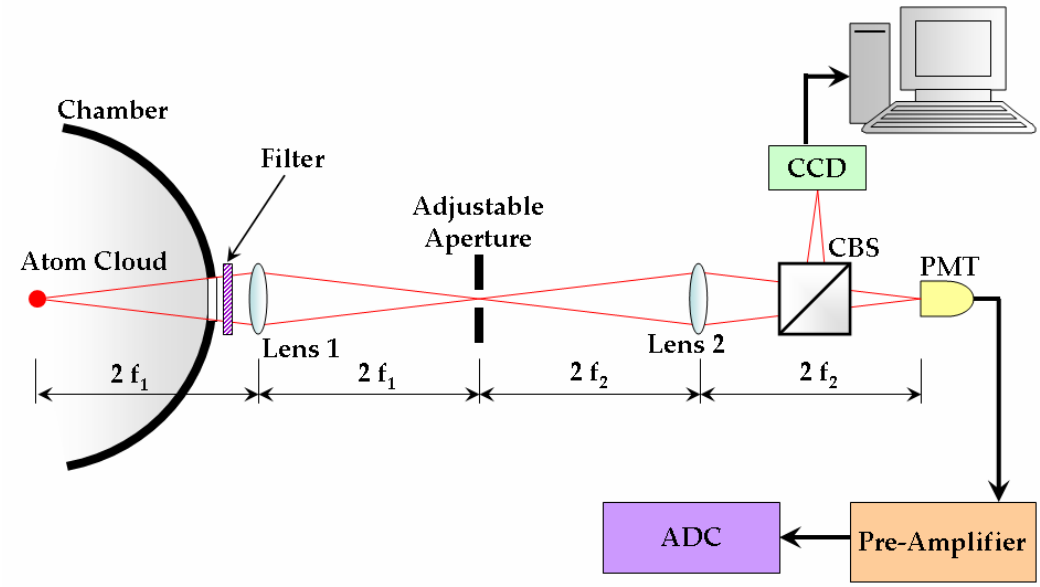

Figure 3.6: An illustration of the spatial filtering and imaging of the fluorescence from the MOT onto a PMT and a CCD camera. The entire imaging apparatus is housed in a black tubing (not shown) in order to minimize the amount of ambient and stray light entering the active areas of the detectors.

since the laser beams which cause the fluorescence are also generating the undesired noise. So we set up a spatial filtering imaging apparatus to minimize the amount of scattered light reaching the detector. The schematic diagram of the same is shown in Fig. 3.6. We use a photomultiplier tube (Hamamatsu Photonics: R636-10) for detecting the spatially integrated fluorescence light from the atoms. The fluorescence from the atoms is also imaged onto several CCD cameras (Thorlabs: DC210) to track the position of the atom cloud in independent directions. The blue light from the LIAD LED is blocked out from these detectors using interference filters (Thorlabs: FL780-10) with a narrow pass band about the laser line frequency.

Atom number and density measurements

Every individual component and the entire system is carefully characterized for its transmission losses so as to determine accurately the total light flux from the

MOT in the detector acceptance angle. The scattering rate of resonant light by an atom can be approximated by [28],

$$R = \frac{\Gamma(I/I_s)}{1 + 2(I/I_s) + 4(\Delta/\Gamma)^2} \tag{3.3}$$

where Γ is the natural linewidth of the cooling transition, I is the total cooling laser intensity in the six MOT beams, I_s is the saturation intensity for the transition and Δ is the detuning of the cooling laser from resonance. By measuring the total power of fluorescence light scattered by the atoms into the input solid angle of the spatial filtering setup, we can estimate the number of atoms in the MOT. The principle sources of error and uncertainty for the number measurement are (a) laser intensity variations, (b) the laser detuning fluctuation and line width (c) the statistical uncertainty in the measurement of the light intensity incident on the photo-multiplier. The overall uncertainty in determining the absolute atom number using the procedures adopted is estimated to be $\pm 18\%$.

A typical image of the fluorescence from the MOT captured on the CCD camera is shown in Fig. 3.7. This is a projection of the fluorescence of the full three-dimensional extent of the MOT onto a plane. This image can be fitted with a Gaussian function to obtain a certain variance σ'^2. Assuming a spherically symmetric density profile for the MOT guarantees that the variance σ^2 of the three dimensional distribution is equal to the variance σ'^2 of the two-dimensional fit-function. We calculate a typical full width at half maximum (FWHM) of 1mm. By knowing the corresponding total number of atoms in the distribution, the fit function can be integrated to obtain the normalizing constant that completely determines the density distribution. We calculate a peak density of $1.8 \times 10^9 \mathrm{cm}^{-3}$. The fit function for the atom density profile on a central plane of the MOT is shown in Fig. 3.8.

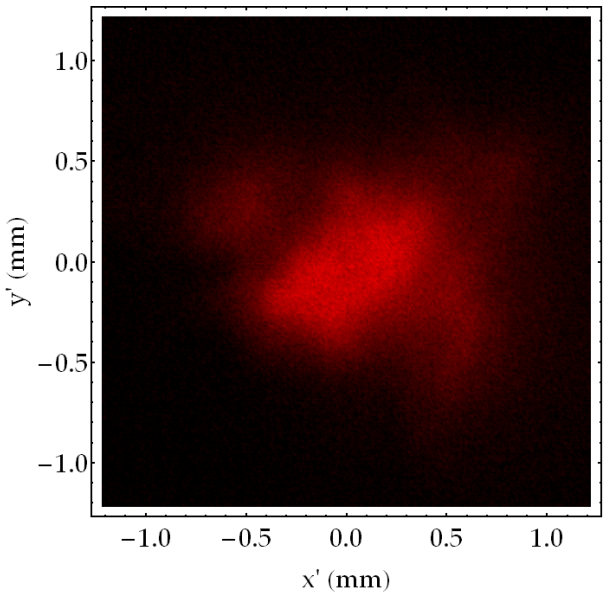

Figure 3.7: A typical false-colour image of the fluorescence from the MOT captured on a CCD camera. The image is a projection of the light scattered from the full three-dimensional extent of the atom cloud onto a plane denoted as $X' - Y'$. The magnification factor due to the different focal lengths of the two lenses shown in Fig. 3.6 has been corrected for in the dimensions of this image.

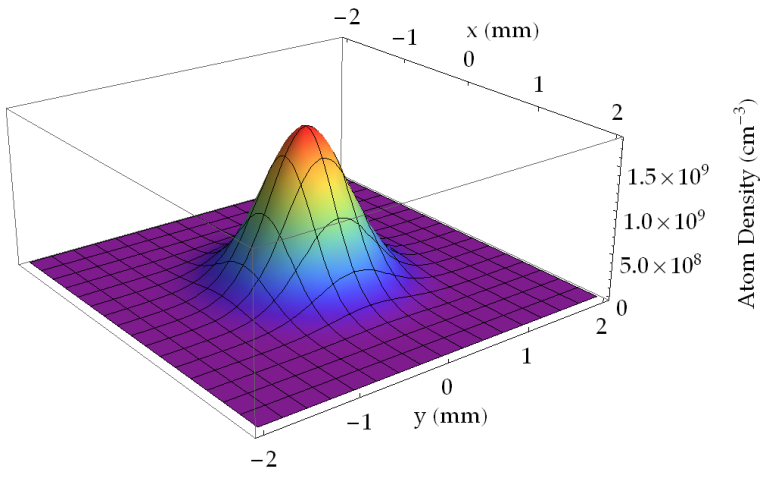

Figure 3.8: The density function of the atom cloud obtained by fitting the image data of Fig. 3.7 to a symmetric Gaussian distribution and normalizing with the total number of atoms.

3.3 The Ion Trap

3.3.1 Ionization methods

The ionization energy (IE) required to eject the electron in the outermost shell from a ^{85}Rb atom is 4.177 eV. The $^{85}Rb^{+}$ ions are loaded into the ion trap using two-photon ionization (TPI), by two different methods described below.

3.3.2 Method I: Resonant TPI

The two photons for ionization here come from the MOT laser (1.59 eV) and the blue light source (BLS) LED (peak at 2.72 eV) used for atomic desorption of the atoms for loading the MOT. Since the MOT lasers are either on resonance or only slightly detuned with respect to the atomic transition, this method corresponds to resonant TPI. The sum of the energy carried by the red and the blue light is 4.31 eV, which is slightly higher than the IE for the Rb atom. Both the sources are continuous. In the absence of the MOT (magnetic field OFF), but MOT beams and LED ON, no ions are captured into the ion trap from the residual gas vapour, though the TPI process is active in the region of overlap of the two frequencies. In order to load the ion trap efficiently, the loading of ions must happen through the MOT atoms. The dominant ionization process is

$$Rb + h\nu_{780} + h\nu_{456} \longrightarrow Rb^{+} + e^{-} + K.E. \tag{3.4}$$

Owing to the small recoil due to the release of the electron, the instantaneous velocity for the creation of the ion is almost zero. This method gives a steady loading rate of ions in the ion trap from the cooled MOT atoms. The temporal overlap of the ON phase of the ion trap along with the two light sources, loads the ion trap at a steady rate.

3.3.3 Method II: Non-Resonant TPI

A frequency doubled Nd:YAG at 532 nm, pulse width $\approx$ 10 ns, and pulse energy of the order of 165 mJ/pulse, is focused onto the trap centre by a lens of focal length 150 mm, mounted outside the vacuum system. The pulse energy is adjusted such that the ionization occurs only in the focal region of the beam. The ionization can be effected from the residual vapour in the trap volume that overlaps with the 532 nm pulse, or from the atoms in the MOT. The dominant ionization process is

$$Rb + 2^{(+)} \times h\nu_{532} \longrightarrow Rb^{+} + e^{-} + K.E. \tag{3.5}$$

where the superscript on 2 indicates the possibility of more than two photon participating in the ionization process with some probability. A single photon at 532 nm carries 2.33 eV energy, so two photons at 532 nm are sufficient to ionize a Rb atom [29]. This method permits ion creation directly from background vapour, at a specific time in the experimental cycle. However, in order to load the trap from vapour, it is required to keep the getter ON. A significant shot to shot variation, of the number of ions loaded into the ion trap, is seen in this method, irrespective of whether the ion trap is loaded from the background gas or from the MOT.

3.3.4 The RF and biasing system

The time varying RF signal for the ion trap is produced in a function generator (Agilent: 332204) and amplified using a wideband power amplifier (Krohn-Hite: 7602M). The amplifier generates two waveforms of equal amplitude (V_{RF}) and frequency nu_{RF} that are 180° out of phase and these are contacted to the respective diagonally opposite quadrupole electrodes of the trap. The Agilent function generator is used in the Burst Mode which is activated using a trigger pulse. This allows the RF trapping fields to be switched ON or OFF within a

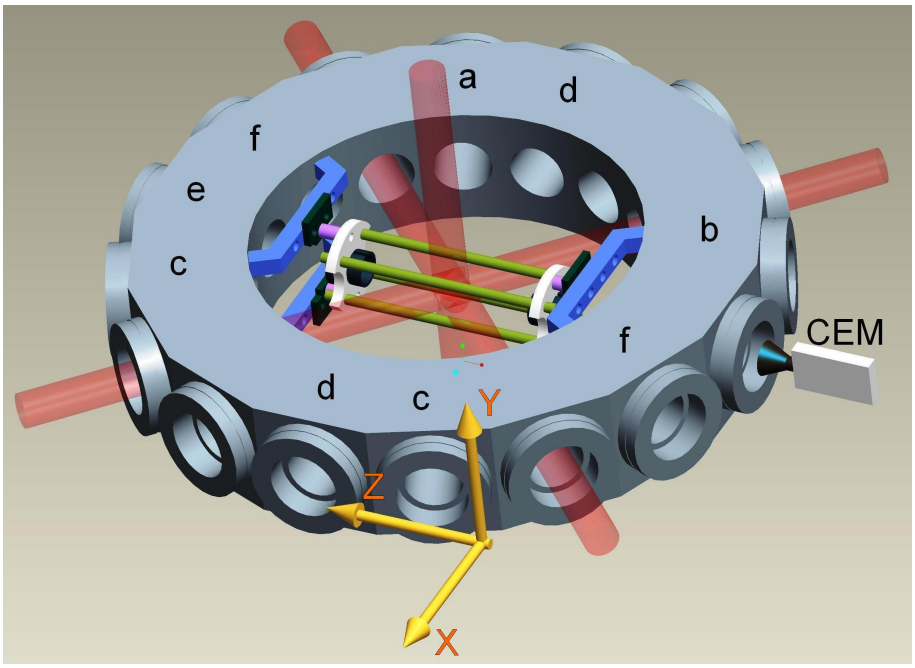

Figure 3.9: Experimental Schematic: For convenience we repeat the figure in Chapter 2 showing the schematic diagram of the hybrid, ion-atom trap, within the experimental chamber. The diagram is not to scale. The ion trap axis is oriented along the z-axis. The magnetic field coils for the MOT (not shown) are external to the vacuum system, mounted symmetrically from the origin coaxial with the y-axis. A CEM for ion detection, is mounted coaxial with respect to the ion trap axis, in the -z direction from the origin. The horizontal MOT beams intersect the z-axis, at the origin, with 45 and 135 degree angles. The vertical beam intersects this arrangement orthogonally. The ports are labelled to illustrate the relative positions of the various components of the experiment as follows. (a) alkali atom dispensers, (b) the blue light source, (c) MOT imaging and fluorescence measurement, (d) Nd:YAG ionization ports, (e) the vacuum pump connection, and (f) feedthroughs.

fraction of the RF time period. The typical range of the parameters used for trapping the ions is, 400 kHz$\leq \nu_{RF} \leq$ 600 kHz and $0 < V_{RF} \leq$ 120V. limited at the higher voltage and frequency values by the gain bandwidth product of the RF amplifier. Axial confinement is provided by a positive voltage V_{ec} on the end-cap electrodes in the range $0 < V_{ec} \leq 100$ V.

3.3.5 Detection of ions

The prospects of fluorescence detection of the ions in the trap is compromised by the lack of convenient transitions, for the closed shell Rb^+ ion. However, in the event of a trapped optically active ion, for example, a singly ionized alkaline earth atom, the optical access allowed by the experimental design permits fluorescent ion detection. For the experiments with Rb though, only the destructive detection of the ions is implemented, using a CEM (Dr.Sjuts: KBL 10RS), which is located beyond the end-cap along the z direction as shown in Fig. 3.9. The funnel of the CEM is maintained at a high negative voltage V_B for positive ion detection. This gives a significantly detectable ion signal for $|V_B| > 1800$V. The tail of the CEM is held at ground potential, enabling us to define V_B as the bias voltage of the CEM. The ions are extracted onto the CEM by switching the potential on the hollow ring end-cap electrode that is close to the CEM, to a negative value, while keeping the opposite end-cap electrode constant and the RF of the ion trap in steady operation. The switching of the potential on the end-cap electrode is effected in less than one period of the RF cycle. The trapped ions pass through the hollow centre of the end-cap electrode and are attracted by the high voltage on the CEM cone. The ions detected by the CEM can be reliably measured in two modes of operation, the pulse counting mode and the analog mode. Due to identical charge/mass (e/M) ratios for the trapped ions, all of the trapped ions impact the detector within a time window of 10 - 30 μs, depending on the extraction voltage.

CEM pulse counting

For pulse counting detection, the output electrode of the CEM is connected to a 50Ω termination of a Digital Oscilloscope. Each ion detected manifests as an 8ns negative current pulse (Fig. 3.10(inset)). The pulse train for the 10 μs interval is recorded on the Digital Oscilloscope (Tektronix: TDS-3044B), and the pulses are counted by post-processing the pulse train using an appropriately set discriminator level (DL). All instances, when the falling edge of the CEM pulse train crosses the negative DL, are counted as valid counts, and signal which peaks below this level is rejected as noise. A similar exercise is done with the exact but oppositely signed DL to determine the number of spurious counts due to bipolar noise and this is suitably subtracted. As the ion counting is done with the recorded data train, the DL can be set very systematically as illustrated in Fig. 3.10. The counts as a function of DL has identifiable regions, as illustrated in Fig. 3.10, which allows the determination of a reasonable value of discriminator level for the analysis of the ion counts at a particular CEM bias. This procedure is benchmarked against the physical counting of the peaks in several individual time traces to make the algorithm robust against over counting or under counting. A distinct advantage of this method of post analysis is that robust and consistent algorithms can be developed for pulse counting and data from several different runs can be analysed in a uniform manner. The disadvantage of this method is that several ions piling up on top of each other (within 8ns), would register as a single count. From a series of experiments, we determine that $\approx 300 \pm 30$ counts /10 μs is the limit of ions that can be counted. This implies a maximum counting rate of 30×10^6 counts/s, which pushes CEM detection to its very limit.

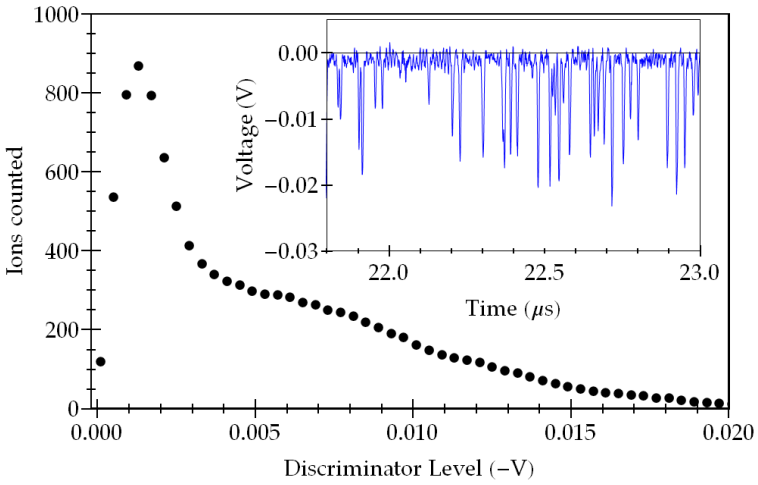

Figure 3.10: The variation of the number of ions counted as a function of set discriminator level (DL). The inset shows a small section of the CEM signal contributing to the analysis shown in the main figure. The ideal distribution would be a monotonically decreasing number as a function of increasing magnitude of the negative DL. Every negative edge crossing the DL triggers a logical valid count and adds 1 to the total number of counts. At DL $<$ 2 mV, the number of counts increases because of the presence of small offset and rapidly fluctuating noise. For DL $>$ 2 mV, the number of counts is monotonically decreasing, as expected. However the initial decrease is rapid and is susceptible to noise counts due to baseline oscillation. A voltage level of 5 mV is identified as the discriminator level for the purpose of reliable pulse counting.

Analog mode detection

For the analog mode detection, the output of the CEM is fed into a low noise pre-amplifier (Hamamatsu: C7319), with set amplification, and the output of the pre-amplifier is recorded on a digital oscilloscope (DO). The pre-amplifier has a frequency response similar to that of a low-pass filter with a 3dB cut-off frequency of 200kHz. This results in a smearing out of the individual ion pulses to give an integrated voltage waveform. The area under the curve of this waveform is then proportional to the number of ions incident on the CEM. This method of data acquisition can be utilized to reliably extend the detection ability of the CEM beyond $\approx 300 \pm 30$ counts/10 μs. The ion counts in the two modes can be calibrated against one another to determine the constant of proportionality as illustrated in Fig. 3.11. Thus we have a robust characterization of the various aspects of counting ions with the CEM. Calibrating the CEM as in Fig. 3.11, for different V_B, allows us to reliably compensate for varying detection efficiencies with V_B and extend the use of the CEM for larger count rates of ions.

When the CEM is biased for positive ion collection, the dark count rate is statistically insignificant. However in the presence of the diffuse ionizing light from the BLS, we see a spurious count rate which depends on the intensity. This systematic baseline has been corrected for wherever applicable.

3.4 The data acquisition

The entire experimental sequence is controlled through a real time operating system (RTOS) module (Keithley: CPUT10) loaded into a control rack (Keithley: ADWin Pro). This rack also has an 8-bit analog to digital converter (ADC) module and an 8-bit Digital to analog converter (DAC) module wired into it. The required triggers and analog signals in the experiment are conveniently

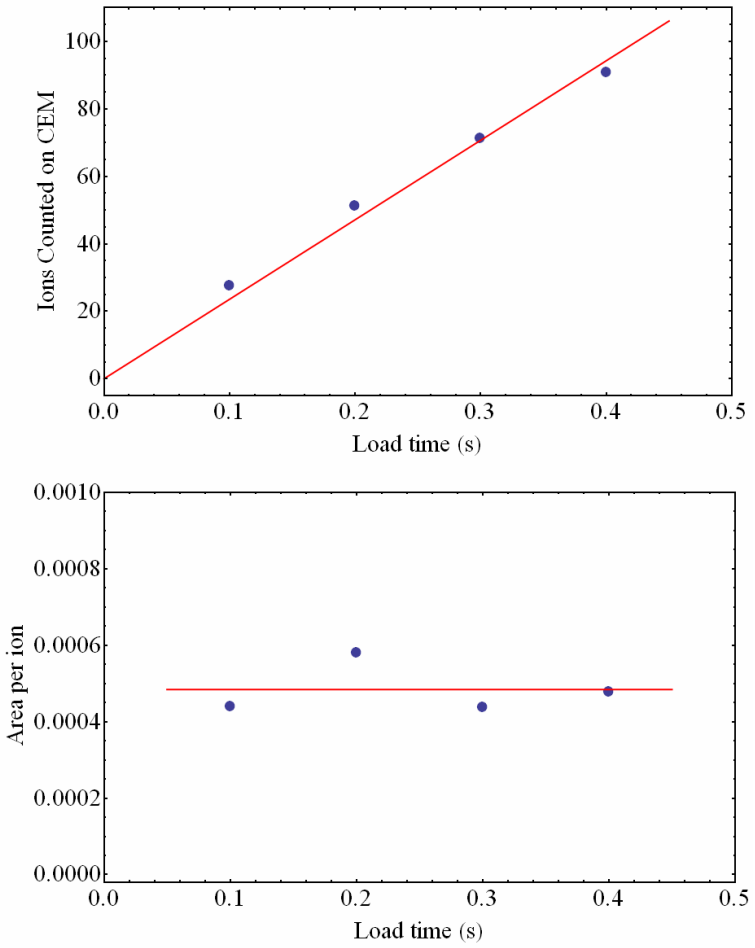

Figure 3.11: (a) The number of ion pulses counted on the CEM for different ion loading times using resonant TPI. (b) The ratio of the analog mode signal detected on the Hamamatsu(C7319) pre-amplifier with respect to the pulse counting mode of the CEM shown in panel (a) for different ion loading times. The number of trapped ions produced from the MOT increases linearly with time for the first few seconds of loading. We therefore calibrate, at $V_B = 2400$ V, the correspondence between the ions counted by the pulse counting algorithm and the analog mode signal. Such a calibration, allows us to switch between the two modes as per experimental convenience and extract the ion counts.

generated by a suitable program written in ADBasic and compiling it into to the RTOS memory. In a similar fashion, analog signals can also be recorded from the experiment onto a computer using the ADWin module as an interface.

The other instruments such as oscilloscopes, function generators, power supplies and cameras that are to be programmed remotely from a computer need to be integrated under one common platform. For this we use the software Labview 7.1 which has device-driver support for a variety of commercial instruments. Labview 7.1 also provides a convenient graphical user interface (GUI) that identifies each device as a virtual instrument (VI) and provides a structured programming platform to sequence various events on different devices in the experiment. The ADWin system is treated as a VI on the Labview platform and an ADBasic program is treated as an event. The Labview software is operated on a personal computer and the time overhead between events is of the order of a hundred milliseconds. Slow events such as saving an acquired waveform on the oscilloscope or setting a power supply voltage at a constant value are directly sequenced on Labview and the fast events such as triggers and real-time data acquisition are sequenced on the ADWin system.

3.5 The experimental sequence

The general experimental sequence is illustrated in Fig. 3.12. Before commencing any ion-atom experiment, the quadrupole magnetic field of the MOT is kept on and the cooling and repumper lasers are locked to the appropriate frequencies. Following this the experimental sequence for the two methods of MOT loading namely the getter loading and the BLS loading are described below.

Getter Loading of MOT

The getter is kept on well before the experiment so that the vapour pressure of the Rb is equilibrated inside the chamber. An electromechanical shutter blocks

the path of the cooling and repumper lasers just before the experiment. The experiment begins by opening the shutter and the MOT starts to load. The ion trap RF voltage is kept off and the voltages on the endcaps are in extraction mode till the MOT loads to saturation. Once the MOT is in saturation (typically after about $30 - 40$s of loading), the ion trap RF is switched on and the endcap voltages are switched to trapping mode (both positive). Simultaneously, the BLS is turned on and the ion-trap is loaded for a period of τ_{il}. The BLS is now turned off and at this juncture, we have the option of retaining the atoms in the MOT or ejecting them by closing the shutter, depending upon the specific experiment. The ions are held for a further hold time of τ_{ih} in the presence or absence of the MOT atoms. After this, the endcap voltages are switched to extraction mode and the ions exit the trap to hit the detector. The oscilloscope is triggered by the switching of the endcap voltage. The raw ion pulse train or the integrated ion signal from the preamp is recorded on the oscilloscope.

BLS Loading of MOT

In this method, the getter is off throughout the experiment. The shutter is kept open before starting the experiment. For the first few seconds of the experiment, we may need to collect a background light baseline for the fluorescence detector. After this, the MOT is loaded by switching on the BLS. The ion trap RF voltage is kept off and the voltages on the endcaps are in extraction mode till the MOT loads to saturation. The creation of ions is active during this period, but the created ions are not trapped. Once the MOT is in saturation, the ion trap RF is switched on and the endcap voltages are switched to trapping mode. The BLS is kept on for an ion loading time of τ_{il} after switching on the ion trap. The BLS is now turned off and at this juncture, we have the option of allowing the atoms in the MOT to slowly exit the trap with their characteristic time constant or ejecting them immediately by closing the shutter, depending upon the specific experiment. The ions are held for a further hold time of τ_{ih} in the presence

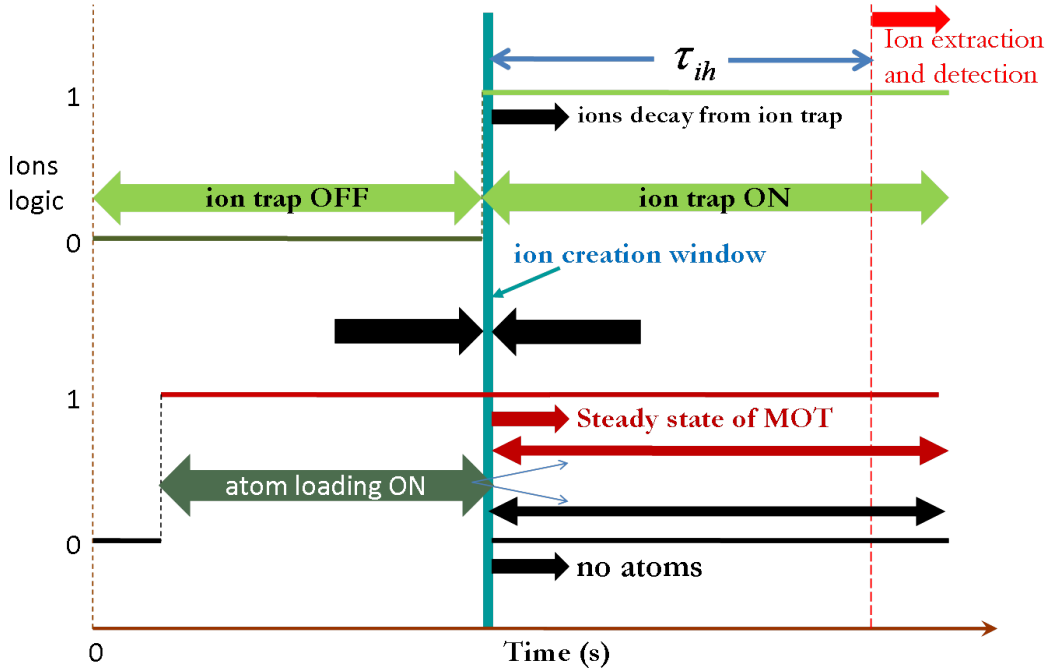

Figure 3.12: The generic time sequence of an ion-atom experiment in our setup

or absence of the MOT atoms. After this, the endcap voltages are switched to extraction mode and the ions are detected as described above.

3.6 Stability regions

The trapping of the Rb^+ ion relies on the interplay of three parameters, the frequency V_{RF}, time varying voltage amplitude V_{RF}, and the static end cap voltage, V_{ec}. We characterize the trap by varying the value of V_{RF} for each frequency and observing the number of ions remaining in the trap after a small interval of time. Fig. 3.13(a) shows the experimentally observed stability diagram at $\nu_{RF} = 600$kHz. Due to the gain-bandwidth limit of the amplifier that we use, we cannot access all the values of V_{RF} at $\nu_{RF} = 600$kHz where there is stable trapping without introducing significant harmonic distortion in the drive voltage. For comparison, we show a plot of the numerically simulated maximum trappable initial speed of the ion as a function of V_{RF} in Fig. 3.13(b). We choose the operating point for our experiments as $\nu_{RF} = 600$kHz, $V_{RF} = 91$V and

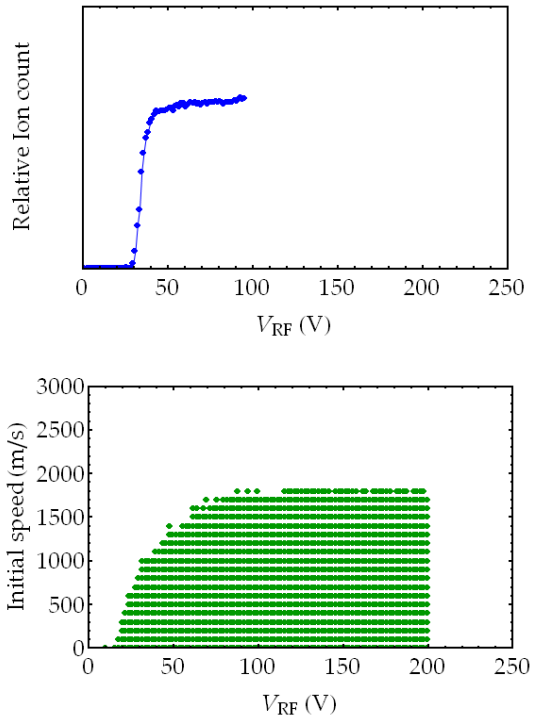

Figure 3.13: The experimentally determined stability region of the ions is shown in panel (a). Due to the gain-bandwidth limit of our RF amplifier, the measurements correspond to a distortion-free voltage only till $V_{RF} = 95$V. The vertical axis is a measure of the number of ions detected after a 0.5s loading and immediate extraction. Panel (b) shows the numerically simulated map of those initial velocities of the ion for which there is stable trapping for a period of 50 RF cycles, as a function of V_{RF}.

$V_{ec} = 80$V.

CHAPTER 4

Interactions between trapped ions and cold dilute atoms

4.1 Introduction

The experimental setup described in Chapter 3 has the capability to trap ions and atoms together in spatial overlap providing a platform to study the different interactions between them. The important questions that arise within the context of such an experiment are: What is the nature of these collisions? Which collision channels are relevant for our experimental setup? How to quantitatively describe each collision? In this chapter we formulate our strategy to systematically address these questions. The results that we derive here shall be used in the subsequent chapters to get a better understanding of the phenomena of sympathetic cooling. The theoretical framework that we shall build will serve as the basis for the numerical simulations of Chapter 5.

4.1.1 The possible interactions

We mainly confine ourselves to the binary collisions between an ion and its parent atom. The density distribution of the atoms in our experiment is in the range of $10^9 \mathrm{cm}^{-3}$ as calculated in section 3.2.4, which constitutes a very dilute system. Since the number of ions loaded is much lesser that the number of atoms in the MOT, and confined in similar trapping volumes, the density of the ions is also quite small. Therefore in the first approximation, it is reasonable to consider the ion-atom collisions that take place in the system as predominantly binary collisions, i.e. between a single atom and a single ion at any given time. There

is also the possibility of collisions between the atoms themselves and the ion-ion Coulomb repulsion. If we take the distance between two colliding entities to be R, the asymptotic atom-atom interaction is characterized by a neutral-neutral Van der Waals potential which has an attractive $\sim -1/R^6$ dependence. The ion-neutral atom interaction has an attractive $\sim -1/R^4$ dependence and the ion-ion interaction has a repulsive $\sim +1/R$ dependence. Clearly, the ion-ion interaction is the strongest of all. In fact this Coulomb interaction is not binary, not delta-correlated and the total cross-section diverges. Consequently, we cannot really describe the Coulomb repulsion in an ion cloud using a local collision framework. Rather, when the ions are in equilibrium, their motion can be approximated by considering an effective mean field potential due to the entire cloud. For very low densities of ions, this mean field can be ignored under certain conditions and the ions treated as non-interacting particles. In the subsequent sections, we shall be focussing only on the different channels in the ion-atom interaction. The atom-atom interaction will be completely neglected and the ion-ion interaction will be considered only where required.

4.2 The collision channels

The two-body collision channels between an atom and an ion can be classified into the elastic and inelastic channels. The elastic collisions only result in a change of the kinetic energy of the colliding particles while the internal degrees of freedom of the ion and the atom remain the same. In contrast, the inelastic channels comprise of the collisions where the internal state and energy of the participating entities may change after the collisions in addition to a change in their velocities. The actual duration of the collision δT_{coll} is assumed to be very short compared to the observation time scales involved in the experiment. The mean time between the collisions is determined by various factors such as the number density and the temperature and is also much greater than δT_{coll}.

4.2.1 The interaction potential

When an ion of charge Q is in the vicinity of an atom, the electric field of the ion polarizes the electron cloud of the atom. So, a dipole moment is induced in the atom and this induced dipole is attracted towards the charge. This interaction is characterized by an asymptotic potential given by

$$V(R) = -\frac{\alpha Q^2}{2(4\pi\epsilon_0)^2 R^4} \tag{4.1}$$

where α is the dipole polarizability of the atom, ϵ_0 is the permittivity of free space and R is the separation between the ion and the atom. This form of the potential corresponds to the molecular potential between the atom and the ion at large values of R where the internal degrees of freedom of the atom are not really part of the interaction except the electron cloud of the atom as a whole getting polarized. The electronic configuration of an Rb atom is such that there is a closed shell of electrons and one electron in the outermost shell. This valence electron contributes majority of the polarizability of the atom. An Rb^+ ion has a stable octet electronic configuration. So the polarizability of an Rb^+ ion is very small, similar to that of the inert gases. This is illustrated by the value of the ground state dipole polarizability for the Rb atom being $\sim 47 Å^3$ [30] and that for the Rb^+ ion being ~ 1.4 $Å^3$ [31].

For an inelastic collision, the evolution of the ion and atom in the molecular potential has to be considered. Suitable approximations can be made depending upon the energy of the collision and in many cases, a semi-classical calculation is sufficient.

4.3 Elastic collisions: Classical framework

The problem at hand for the two body scattering is to determine the final velocities of the ion and the atom after a collision with a certain impact parameter and a given set of initial velocities. This problem is simplified when we are dealing

with collisions between ions in an ion trap and cold atoms in a MOT. The typical temperature of the atoms in a MOT is of the order of $\sim 100\mu$K corresponding to an RMS velocity of less than 1m/s. The ions in the absence of any external cooling have much higher instantaneous velocities. So, effectively we can assume that an ion is colliding with an atom initially at rest in the Laboratory frame. We shall briefly investigate the theory for a general elastic collision in a central force field as discussed in various books on classical mechanics [32, 33] and then apply it to our specific situation.

Consider an ion of mass m_I and initial velocity $\mathbf{v_I}$ colliding with an atom of mass m_A at rest in the laboratory frame. If the particles were not interacting, then the distance of closest approach between the particles would be the impact parameter denoted as b. Long after the collision takes place, the velocity of the ion is $\mathbf{v'_I}$ at an angle θ_L and the velocity of the atom is $\mathbf{v'_A}$ at an angle χ_L both with respect to the original path of the ion along $\mathbf{v_I}$. The centre of mass of the two particles moves with a velocity $\mathbf{V_{CM}}$ in the laboratory frame in a direction parallel to $\mathbf{v_I}$ and remains constant throughout the collision process. The different vectors and angles before and after the collision in the laboratory frame are illustrated in Fig. 4.1.

From the conservation of linear momentum, we find that

$$(m_I + m_A)V_{CM} = m_I v_I \tag{4.2}$$

By putting $\mu = m_I m_A/(m_I + m_A)$ as the reduced mass of the pair of particles,

$$V_{CM} = v_I \left(\frac{\mu}{m_A}\right) \tag{4.3}$$

By the simultaneous conservation of kinetic energy and linear momentum in the collision, we can write

$$\begin{aligned} \frac{1}{2}m_I v_I^2 &= \frac{1}{2}m_I v_I'^2 + \frac{1}{2}m_A v_A'^2 \\ m_I v_I &= m_I v_I' \cos\theta_L + m_A v_A' \cos\chi_L \\ 0 &= m_I v_I' \sin\theta_L - m_A v_A' \sin\chi_L \end{aligned} \tag{4.4}$$

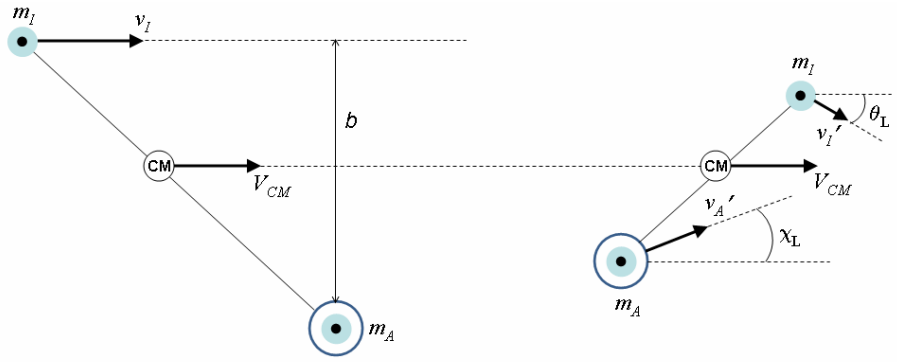

(a) Before collision (b) After collision

Figure 4.1: Elastic scattering in the laboratory frame: An ion with velocity v_I approaching an atom at rest in the laboratory frame with an impact parameter of b is shown in (a). The interaction between the ion and the atom in general slows down the ion and changes its direction of motion. (b) shows the velocity vectors and the angles of deflection of the ion and the atom long after the interaction has taken place. Note that since there is no external force on the ion-atom system, the velocity of the centre of mass $\mathbf{V_{CM}}$ remains unaffected before, during and after the collision. The ion and the atom are attracted towards each other as shown owing to the form of the interaction potential.

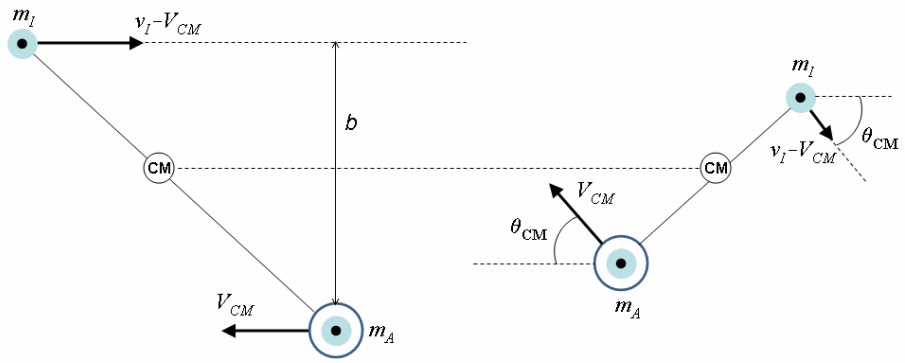

(a) Before collision (b) After collision

Figure 4.2: Elastic scattering in the centre of mass frame: (a) and (b) illustrate the scattering of Fig. 4.1 from a reference frame where the centre of mass of the ion-atom system is at rest. Note that in (a) the atom is moving with a velocity opposite to that of the ion such that their mutual approach velocity remains to be v_I. After the collision, as shown in (b), the angle of scattering of the ion and the atom is a common angle θ_{CM} with respect to the central axis. The magnitudes of the velocities of the ion and the atom remain the same as that of their respective velocities before the collision

The final velocities of the atom and the ion can be determined from the above relations in terms of their initial velocities and the scattering angles in the laboratory frame as

$$\begin{aligned} v'_I &= v_I \sqrt{1 - \frac{4\mu^2}{m_I m_A} \cos^2 \chi_L} \\ v'_A &= 2 v_I \frac{\mu}{m_A} \cos \chi_L \end{aligned} \tag{4.5}$$

To determine the scattering angles θ_L and χ_L, we go to the centre of mass frame of reference. The different velocity vectors before and after the collision in this reference frame are illustrated in Fig. 4.2. The velocity of each particle in the laboratory frame is equal to the vectorial sum of its velocity in the centre of mass frame and the velocity of the centre of mass itself. By comparing Fig. 4.1(b) and Fig. 4.2(b), we can draw the vectorial relations as shown in Fig. 4.3. Clearly, the angle χ_L is related to θ_{CM} by

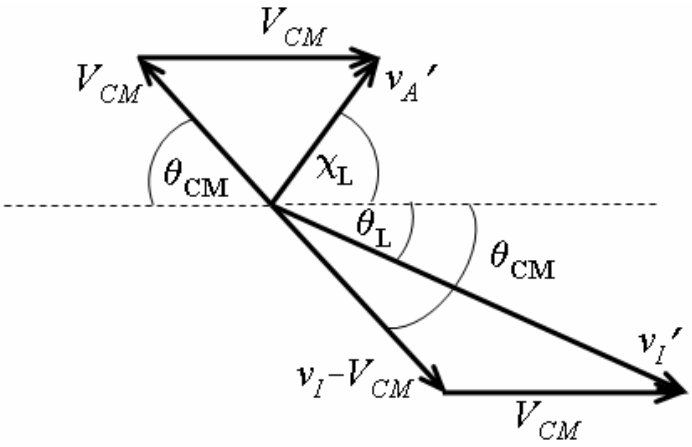

Figure 4.3: The velocity vectors of the ion and the atom after the collision are schematically shown to illustrate their vectorial relations with the velocity of the centre of mass. A velocity in the laboratory frame is a vectorial sum of the respective velocity in the centre of mass frame and the velocity of the centre of mass itself. From this diagram, it is straightforward to express χ_L and θ_L in terms of θ_{CM}.

$$\chi_L = \frac{1}{2}(\pi - \theta_{CM}) \tag{4.6}$$

and the angle θ_L is related to θ_{CM} by

$$\tan\theta_L = \frac{(v_I - V_{CM})\sin\theta_{CM}}{V_{CM} + (v_I - V_{CM})\cos\theta_{CM}}. \tag{4.7}$$

But since $V_{CM}/(v_I - V_{CM}) = m_I/m_A$, we can write

$$\tan\theta_L = \frac{\sin\theta_{CM}}{\frac{m_I}{m_A} + \cos\theta_{CM}}. \tag{4.8}$$

Thus for a given impact parameter and initial instantaneous velocity of the ion before the collision, we can determine the final velocity after the collision provided we know the deflection angle θ_{CM} in the centre of mass reference frame.

The angle θ_{CM} of course depends upon the specifics of the central potential. The standard approach is to transform the two body scattering into an equivalent problem of a hypothetical particle of mass equal to the reduced mass μ scattered by a fixed centre of force in the centre of mass frame. This problem is dealt with in many textbooks on classical mechanics [32, 33]. We do not give

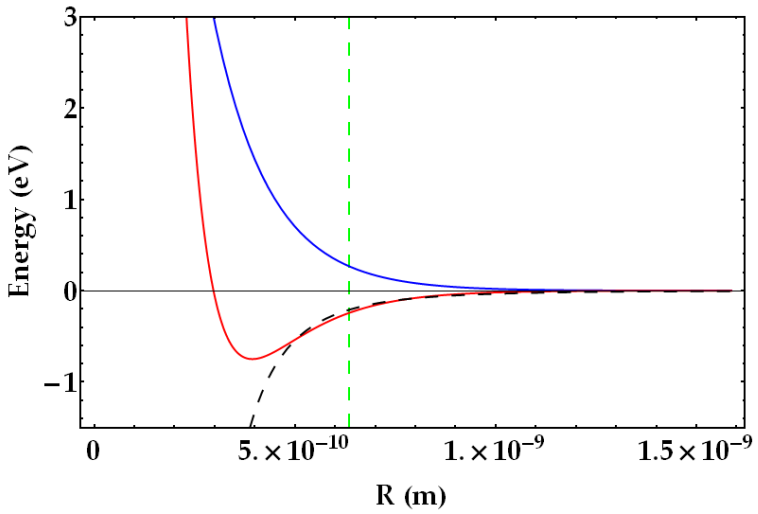

Figure 4.4: The molecular potential energy curves for the $^{85}Rb^{+}-^{85}Rb$ system [34]. The blue curve corresponds to the ungerade symmetry and the red curve corresponds to the gerade symmetry. The black dashed curve is the asymptotic form of the potential as given by Eqn. 4.1 which is valid for large values of R beyond the green dashed line shown.

the details of this calculation here. For an interaction potential $V(R)$, the centre of mass scattering angle is given by

$$\theta_{CM}(v_I, b) = \pi - 2b \int_{R_a}^{\infty} \frac{dr/R^2}{\sqrt{1 - \frac{2V(R)}{\mu v_I^2} - \frac{b^2}{R^2}}} \tag{4.9}$$

where R_a is the distance of closest approach given by the largest root of the equation

$$1 - \frac{2V(R_a)}{\mu v_I^2} - \frac{b^2}{R_a^2} = 0. \tag{4.10}$$

A real solution for R_a does not necessarily always exist for potentials of arbitrary form. For the ion-atom collision, the long range potential is given by Eqn. 4.1 and we can rewrite Eqn. 4.10 specifically as

$$1 - \frac{\alpha Q^2}{(4\pi\epsilon_0)^2 \mu v_I^2 R_a^4} - \frac{b^2}{R_a^2} = 0. \tag{4.11}$$

The range of validity of the asymptotic form of the potential with respect to the ion-atom molecular potential is only at values of $R > 6 \times 10^{-10}$m for Rb-Rb^{+},

as illustrated in 4.4. In this regime, the scattering trajectories can be classified into simple angular deflections and inspiralling trajectories depending upon the existence of a real root of Eqn. 4.11. A particular value of $b = b_c^{el}$ namely the critical impact parameter separates these two types of trajectories. This is found by analysing the discriminant of Eqn. 4.11 to be

$$b_c^{el} = \left[\frac{4Q^2\alpha}{(4\pi\epsilon_0)^2\mu v_I^2}\right]^{1/4} \tag{4.12}$$

So at a given approach velocity v_I, for an impact parameter $b \leq b_c^{el}$, there is no real root of Eqn. 4.11 and it corresponds to the ion going into an orbit around the atom and in some cases it may emerge out of the potential after a few revolutions in orbit or in some cases it may even inspiral into the scattering centre. When $b > b_c^{el}$, a real root for Eqn. 4.11 exists, and the scattering corresponds to a simple deflection by an angle θ_{CM} which can be determined by Eqn. 4.9. The integral of Eqn. 4.9 cannot in general be solved analytically and a numerical integration has to performed when necessary.

A constraint of the scattering process described above is that since the collision is dictated by a central force, the entire collision including the final velocities lies in a plane determined by the initial velocity vector of the ion and the point where the atom is initially at rest. Using this constraint, and the equations 4.9, 4.8, 4.6 and 4.5, we can completely determine the final velocity vectors of the atom and the ion in the laboratory frame for any impact parameter $b > b_c^{el}$. For $b \leq b_c^{el}$, the final velocity can be determined for certain situations. A detailed calculation of the same is discussed in the appendix of Ref [33] in the context of determining mobilities of ions in neutral gases.

4.3.1 The critical impact parameter for elastic collisions

The critical impact parameter is an important quantity which gives a length scale for the collision process. Fig. 4.5 shows a plot of b_c^{el} versus v_I for elastic

scattering of $^{85}Rb^{+}$ by ^{85}Rb. To get a picture of the interplay between the collision velocity and the impact parameter, we plot the fractional change in kinetic energies $(v_I'^2 - v_I^2)/v_I^2$ and $(v_A'^2 - v_A^2)/v_A^2$ of the $^{85}Rb^{+}$ ion and the ^{85}Rb atom respectively as a function of b for different values of v_I as shown in Fig. 4.6. The first observation is that the ion is always either slowed down by the atom or its velocity is left unchanged. The atom, which we have assumed to be initially at rest always either gains energy or continues to stay at rest depending upon the collision parameters. We also see that there is no significant exchange of energy between the colliding species for values of b higher than a few critical impact parameter units, typically beyond $2b_c^{el}$. At velocities $v_I < 100$ m/s, the absolute value of $b_c^{el} > 50$ a.u. leading to the collision being active even at relatively large impact parameters of a few hundred Bohr radii. For very low velocities where the number of partial waves involved in the collision is small, a full quantum scattering treatment has to be considered. In this work, we do not calculate the cross-sections for the ion-atom scattering and its energy dependence for various regimes. Nonetheless, there are excellent references for the same. The theory of quantum elastic scattering has been considered in detail for species such as Na and Yb in references [4, 35, 36].

4.4 Inelastic collisions

In the previous section we discussed the classical elastic scattering of the ion by an atom with the internal states of the colliding species remaining intact. The problem, in classical theory, was essentially about determining the final velocity vectors of the ion and the atom given the initial velocity of approach and the impact parameter. Most details of the internal states of the species like the wavefunctions and the electronic structure were not really required to describe the scattering in a wide range of collision energies except at very low energies. Only the polarizability α of the atom and the charge of the ion Q were used to

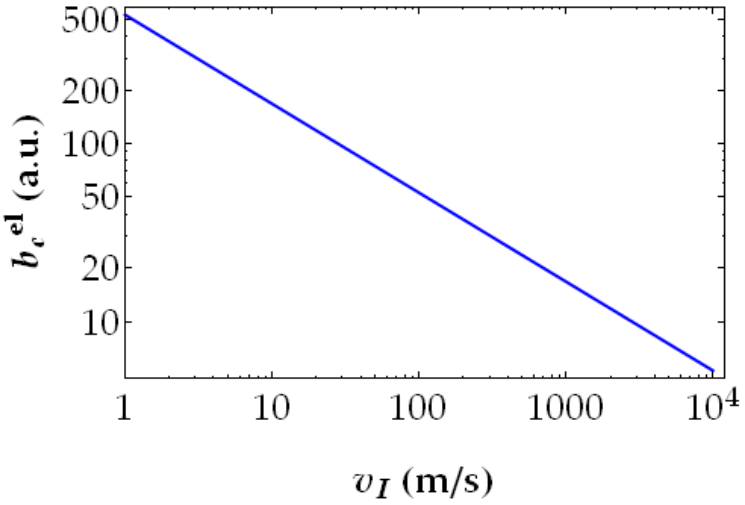

Figure 4.5: Critical impact parameter(b_c^{el}) versus the collision velocity (v_I): The critical impact parameter for elastic collisions as determined by Eqn. 4.12 is plotted against the initial velocity of the ion in the rest frame in a Log-Log scale. We have considered the elastic scattering of a $^{85}Rb^+$ ion by ^{85}Rb atom at rest. The (b_c^{el}) is shown in atomic units corresponding to the Bohr radius and the velocity in SI units

determine the interaction potential of the form Eqn. 4.1 which encompassed all the details of the species. In contrast, for ion-atom binary systems, an inelastic collision involves a change in the internal states of the colliding species, and the problem is about determining the transition probability from an initial state to a final state of the two body system. The number of possible final states for an inelastic process becomes enormously large and an efficient way of handling the problem lies in identifying the specific collision channels which have a much higher probability of occurring than the rest of the channels.

To stay within the context of the present work, we shall restrict our discussions to inelastic collisions involving a positive ion say A^+, with its parent atom A in the ground state. A further restriction that can be enforced is that the kinetic energy in the collision is much lesser than the energy of the optical transitions of the atom and the ion. In other words, we can assume that there is no exchange of energy between the kinetic energy and the internal states of

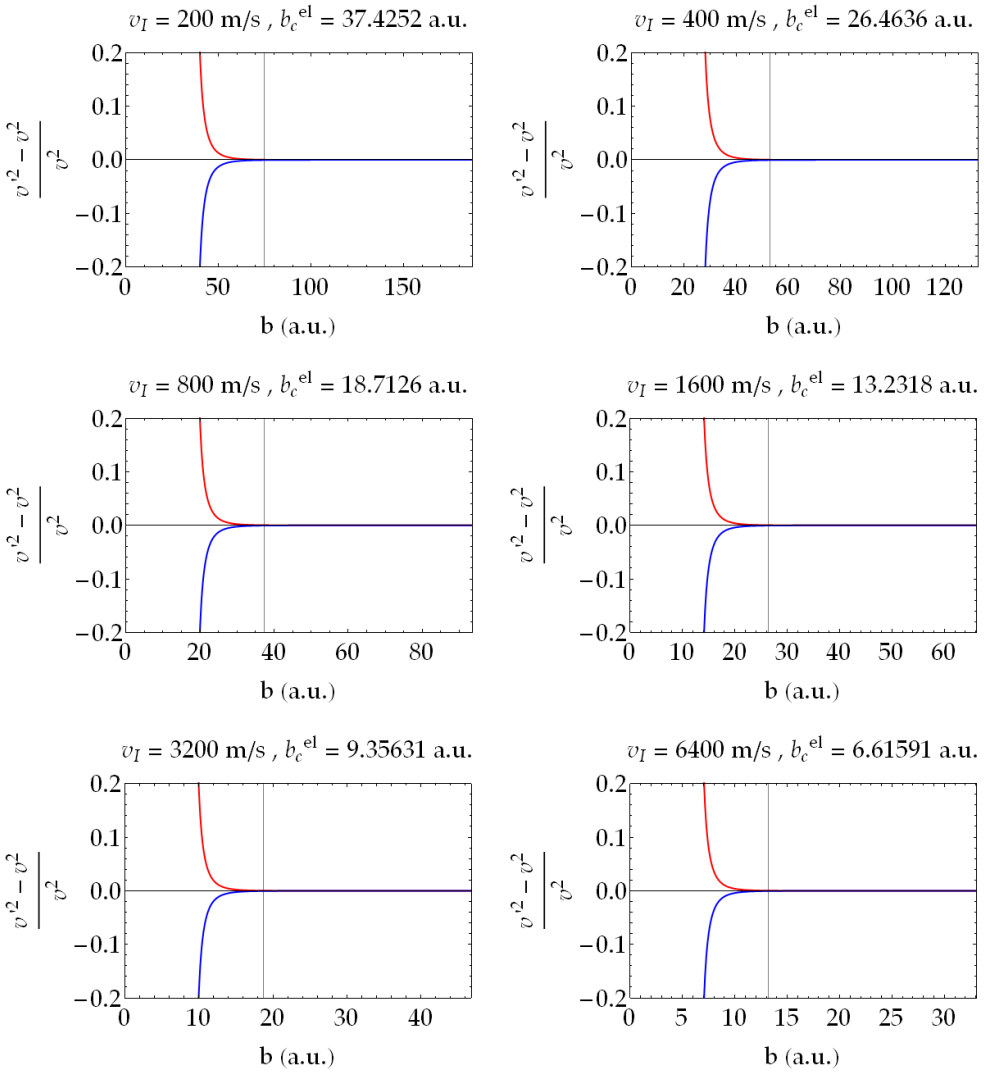

Figure 4.6: The fractional change in the kinetic energy of the ion (blue) and the atom (red) due to the collision is plotted against the impact parameter for different values of the approach velocity v_I. The above plots are again for the same example of $^{85}Rb^{+}-^{85}Rb$ scattering. A typical distance scale for a significant deflection corresponding to $2b_c^{el}$ is illustrated in each plot.

the colliding entities. This is a safe assumption to make for instance in our case of Rb atoms and Rb^+ ions in a Paul trap. A ground state Rb atom needs about 1.6 eV of energy to be excited to its first excited state. This corresponds to a velocity of about 1900 m/s and a temperature of approximately 18000 K. There can be situations where a trapped ion can attain instantaneous velocities as high as this but it is highly improbable that a collision with an atom can happen at such an instant and the entire kinetic energy is coupled into exciting the atom and hence we shall neglect such collisions. Other transitions which are of much lower energy, for instance transitions between the hyperfine states and the corresponding Zeeman sublevels of the atom, shall be ignored for the sake of simplicity. Since we are assuming only two-body collisions, the simultaneous conservation of linear momentum and energy rules out any process involving the formation of a bond between the colliding atom and the ion that could result in a single entity like a molecule after the collision. With these restrictions, the simplest ion-atom inelastic channel is that of charge exchange. As the name suggests, this process involves the exchange of charge, usually due to the transfer of a valence electron from the atom to the ion during the collision. When the ion and the atom are of the same species, the process is called a resonant charge exchange collision and is represented by the reaction

$$A + A^+ \longrightarrow A^+ + A$$

We shall briefly discuss the general nature of such a collision and then address the specific example of charge exchange for the $^{85}Rb^+ - ^{85}Rb$ system. In the above reaction, the valence electron in the outermost shell of atom A hopped onto the equivalent empty shell in the ion A^+ so that long after the collision, the particle which was an ion before is now an atom and vice versa. Of course, this process is a completely quantum effect and identifying between the indistinguishable cores A^+ is not really valid in a pure sense. But in certain situations, like in a beam-target apparatus, we can "label" the neutral particles that emerge

out at a small angle with respect to the beam axis as the atoms "created" due to charge transfer. Specifically, a charge exchange collision between a Rb atom and a Rb^+ ion in their respective ground states involves the transfer of the electron in the outermost s-shell of the atom to the empty s-shell of the ion. Since the two colliding species are the same, the electron does not require any extra energy to get transferred from the shell of one atom to that of the other, irrespective of the kinetic energy of the collision. In other words, such a charge transfer is resonant at all collision energies and hence this process is called resonant charge transfer or resonant charge exchange. For low ion-atom collision energies (E), the cross section for resonant charge exchange $\sigma_{cx} \propto 1/E^{1/2}$, is comparable to the ion-atom elastic cross section [35, 37] $\sigma_{el} \propto 1/E^{1/3}$. At higher energies, the resonant charge exchange, which depends on the molecular state overlap is a very slowly varying function of energy and therefore dominates in comparison to the elastic channel.

4.4.1 Resonant charge exchange (RCx)

Now that we have narrowed down the various possibilities to just one specific channel, the problem is to find out the probability P_{ex} for this charge exchange process to happen in a collision. We shall follow a calculation given in an early work of Holstein [38] to get an estimate of P_{ex}. This method is simple and illustrative, yet giving a very good estimate of the quantities involved. We shall deal with the specific case of the Rubidium atom where the single valence electron can be considered to be bound to an atomic "core" consisting of the nucleus and the tightly bound electrons in the inner shells. The extension of the theory to other alkali atom-ion combinations is straightforward. There are many later works with involved calculations [34, 39, 40]. We refer the reader to these references for improved calculations of the experimentally measurable parameters such as cross-sections and mobilities in a wide range of collision energies.

The formalism

To treat the ion-atom interaction in a quantum mechanical framework, we consider the total wavefunction of the system consisting of the two identical atomic cores and the single valence electron. Using the Born-Oppenheimer approximation, we can first freeze the slow motion of the cores at a certain internuclear separation R and consider only the electronic part of the total wavefunction of the system. This wavefunction has two possible symmetries namely the gerade or even symmetry and the ungerade or odd symmetry corresponding to the bonding and antibonding orbitals of the molecule respectively. The energy eigenvalue of the electronic Hamiltonian $\hat{\mathcal{H}}_e$ for these orbitals expressed as a function of the parameter R gives the molecular potential energy curves. The indistinguishability of the atomic shells to which the electron can get bound to during the collision gives rise to an exchange interaction in the system. This leads to the splitting of the degeneracy between the ungerade and gerade molecular potentials at low values of the internuclear separation R. At large values of R, when the electron is unambiguously attached to one of the atomic cores, the molecular potential asymptotically tends to the formula given by Eqn. 4.1. Fig. 4.4 shows the potential energy curves for the gerade and ungerade symmetries of the ground state $^{85}Rb^{+}-^{85}Rb$ system [34]. For convenience let us label the two identical atomic cores as "1" and "2". When the two cores are far apart, the electron is bound to one of them and the other core corresponds to a free ion. Let the system be described by a state ψ_1 when core 1 corresponds to the ion and core 2 corresponds to the atom and by a state ψ_2 when core 2 corresponds to the respectively with the other core being a free ion. The molecular orbitals corresponding to the gerade (g) and the ungerade (u) symmetries are linear

combinations of ψ_1 and ψ_2 written with the explicit time dependence as

$$\psi_u(t) = \frac{1}{\sqrt{2}}[\psi_1 - \psi_2] \exp\left[-\frac{i}{\hbar}\int^t E_u(R)dt\right]$$
$$\psi_g(t) = \frac{1}{\sqrt{2}}[\psi_1 + \psi_2] \exp\left[-\frac{i}{\hbar}\int^t E_g(R)dt\right] \tag{4.13}$$

where $\hat{\mathcal{H}}_e\psi_u = E_u(R)\psi_u$ and $\hat{\mathcal{H}}_e\psi_g = E_g(R)\psi_g$. E_u and E_g are functions of time via the time dependence of R. In the case of a collision the molecular system is not in one of these stationary states, but rather in a linear superposition of them written as

$$\mathbf{\Phi}(t) = C_u\psi_u(t) + C_g\psi_g(t). \tag{4.14}$$

Let us assume that at a time t_i much before the collision, the core 1 corresponds to the ion and the core 2 corresponds to the atom. The state of the system is described by ψ_1 at that time. So,

$$C_u\psi_u(t_i) + C_g\psi_g(t_i) = \psi_1. \tag{4.15}$$

Using Eqn. 4.13, we can determine the coefficients C_u and C_g which we assume to be independent of time as

$$C_u = \frac{1}{\sqrt{2}} \exp\left[-\frac{i}{\hbar}\int^{t_i} E_u(R)dt\right]$$
$$C_g = \frac{1}{\sqrt{2}} \exp\left[-\frac{i}{\hbar}\int^{t_i} E_g(R)dt\right] \tag{4.16}$$

By substituting these coefficients into Eqn. 4.15 and simplifying we obtain the state of the system at some arbitrary time t as

$$\mathbf{\Phi}(t) = \exp\left[-\tfrac{i}{2\hbar}\int_{t_i}^{t}(E_u + E_g)dt\right]\left(\psi_1 \cos\left[\tfrac{1}{2\hbar}\int_{t_i}^{t}(E_u - E_g)dt\right] + i\psi_2 \sin\left[\tfrac{1}{2\hbar}\int_{t_i}^{t}(E_u - E_g)dt\right]\right) \tag{4.17}$$

For notational simplicity, we have skipped the explicit dependence of E_u and E_g on R. Now, at a much later time t_f, the probability of core 2 being the ion and core 1 being the atom is given by the modulus squared of the coefficient of ψ_2 in Eqn. 4.17 with $t = t_f$. This is also the probability of the charge exchange to take place between the ion and the atom. In the limit of $t_i \to -\infty$ and $t_f \to \infty$, the probability for charge exchange is given by

$$P_{ex} = \sin^2 \left[\frac{1}{2\hbar} \int_{-\infty}^{\infty} (E_u - E_g) dt \right] \tag{4.18}$$

To put in the explicit time dependence of R, we need to make one more assumption. We assume that the collision is fast enough that the ion is moving almost along a straight line during the collision. This is the basis for the impact parameter method discussed in many books on scattering [41, 42]. Although we know that at low energies or at small impact parameters, the trajectory is not really a straight line, given the extent to which it simplifies the calculations, we shall nonetheless follow this method and extrapolate the results to small energies and/or small impact parameters. The straight line trajectory in the laboratory frame of reference is illustrated in Fig. 4.7. The internuclear separation R is then given by

$$R = \sqrt{b^2 + v_1^2 t^2}. \tag{4.19}$$

With this substitution and putting $V_d(R) = E_u(R) - E_g(R)$, Eqn. 4.18 for a given impact parameter b can be written as

$$P_{ex} = \sin^2 \left[\frac{1}{\hbar} \int_{b}^{\infty} \frac{R V_d(R)}{\sqrt{R^2 - b^2}} dR \right] \tag{4.20}$$

We can evaluate this probability for different impact parameters using the potential energy curves from Ref. [34], which are shown in 4.4. A plot of $P_{ex}(b)$ versus b for a given velocity v_1 is shown in Fig. 4.8. $P_{ex}(b)$ is a highly oscillatory function of b with an average value of $1/2$ till a certain value $b = b_{cx}$ which we call as the critical impact parameter for charge exchange. At $b = b_{cx}$,

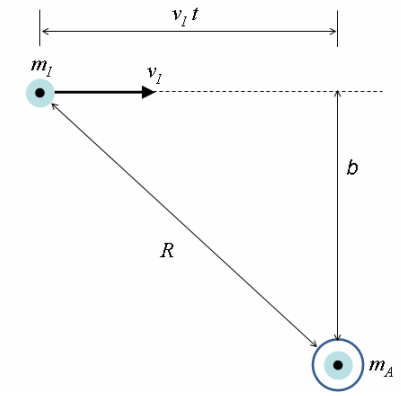

Figure 4.7

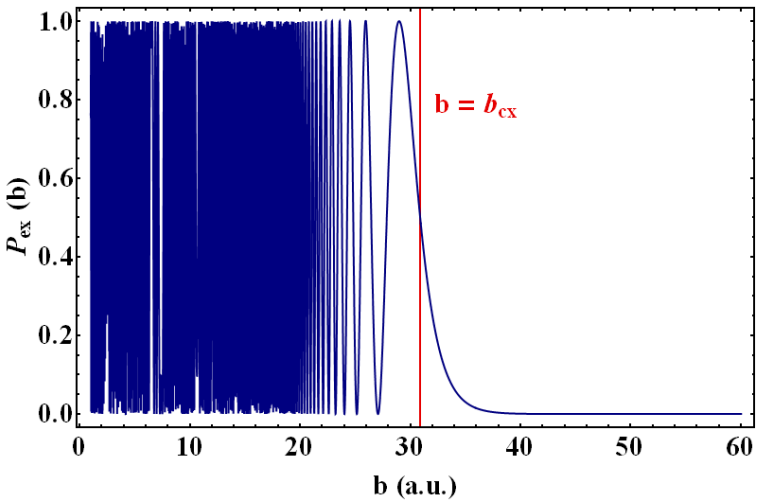

Figure 4.8: The probability of charge exchange as a function of the impact parameter. Here the ion's velocity is taken to be $v_I = 500\text{m/s}$. The probability is a highly oscillating function of b till the value $b = b_{cx}$ as shown with a mean value of half. At $b = b_{cx}$, the probability is exactly half and then falls off rapidly to zero.

$P_{ex}(b_{cx}) = 1/2$ and for $b > b_{cx}$, the value of $P_{ex}(b)$ falls off rapidly to zero. This means that if the impact parameter in the collision is below the critical value b_{cx}, there is an average probability of $1/2$ for the charge exchange to take place. If the impact parameter is much greater than b_{cx}, no charge exchange takes place for the given velocity v_I. We can write the approximate relation

$$P_{ex}(b) \approx \begin{cases} \frac{1}{2}, & b \leq b_{cx} \\ 0, & b > b_{cx} \end{cases}$$

The value of b_{cx} of course depends upon the velocity v_I as shown in Fig. 4.9. The corresponding b_c^{el} is also plotted for comparison.

Post-collision velocities

To obtain the velocities of the particles after the collision, we proceed as in Section 4.3. But when the impact parameter is less than b_{cx}, we assign, on an average, half a chance for the final velocity vectors of the ion and the atom to be exchanged. We observe from Fig. 4.9 that there is a certain range of velocities where $b_{cx} \gg b_c^{el}$. When a collision happens at such a velocity and the impact parameter is such that $b_{cx} > b \gg b_c^{el}$, the deflection produced is very small but there is a 50% probability for the ion and the atom to switch their post-collision velocities. Such a "glancing" charge-exchange collision of a fast ion approaching an atom at rest will result in an ion almost at rest and a fast moving atom after the collision.

4.5 Conclusion

In the above description of the elastic and charge-exchange scattering of an ion by an atom, we have simplified the calculations making use of the relevant energy ranges encountered in our experiments. For instance we have not gone into details of the full quantum calculation of the elastic scattering process at

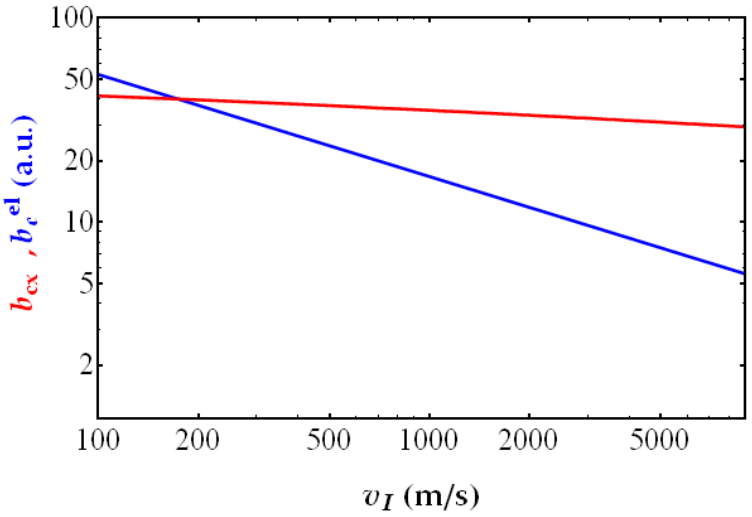

Figure 4.9: The critical impact parameter for charge exchange (red line) is plotted as a function of the ion's velocity v_I. The blue line is the critical impact parameter for elastic collisions shown for comparison. The two lines intersect at about $v_I \approx 150$m/s and in the region where $v_I \gg 150$m/s, we notice that $b_c^{el} \ll b_{cx}$ which corresponds to the regime of glancing charge-exchange collisions.

low energies. The description of the charge exchange process uses the semi-classical impact parameter method. If we were interested in the accurate study of individual collisions, these descriptions may not be adequate. But in the context of a large number of ions moving in time-varying external potentials and undergoing a huge number of collisions with cold atoms in a reservoir, we can use these approximations to get a fairly clear picture of the nature of the interactions in the experiments.

Collisions in the excited state

Another possible ion-atom process that could occur in our system is the charge exchange between an excited state atom and an ion. Depending upon the symmetries of the system involved and the different angular momentum states, the above formalism may or may not be sufficient to describe such a process. But in an ensemble such as a MOT, the total fraction of atoms in the excited state

is estimated to be less than 10%. The majority of the collisions are between the ground state atoms and the ions. But at the same time, for instance, Rb atoms in the excited state have a polarizability that is thrice that in the ground state [28]. In other words, the molecular potentials for the excited state extend to much larger values of R. This generally means higher cross-sections for the elastic and charge exchange processes. Keeping this in mind, depending upon the context, in some cases we shall completely ignore the excited state collisions and in some other cases, we shall specify the degree of importance of such collisions in the phenomenon under study.

CHAPTER **5**

Cooling of ions by interactions with cold atoms

To realize the full potential of the combined trap, it becomes very vital to trap steady numbers of atoms and ions together, possibly in thermal equilibrium, for sufficiently long observation times. However, the different individual trapping mechanisms for the ions and the atoms results in the trapped atoms being significantly colder than the trapped ions. Also, unlike Rb atoms, since Rb^+ ions have a closed shell electron configuration, they are not amenable to direct laser cooling. In fact, the trapped ions get heated [23] due to a variety of factors such as trap imperfections, background gas collisions and radiofrequency (RF) heating due to ion-ion repulsion. The strong binary ion$-$atom interaction resulting in heat flow from ions to atoms is the only available cooling channel for Rb^+ ions in our system. Conversely, trapped ions can also get collisionally heated by the cold atoms, making the resulting equilibrium between ions and atoms intriguing. In this chapter we describe how we utilize these ion-atom collisions to internally stabilize the ion-atom ensemble.

Arguing from first principles, we propose a hypothesis for the scope of collisional cooling in our system of ions and atoms having almost equal mass, and then present our experimental observations that indeed demonstrate the sympathetic cooling of $^{85}Rb^+$ ions in the ion trap by cold ^{85}Rb atoms in the MOT. We then describe the numerical simulations that consider the interactions described in the previous chapter to demonstrate the cooling hypothesis.

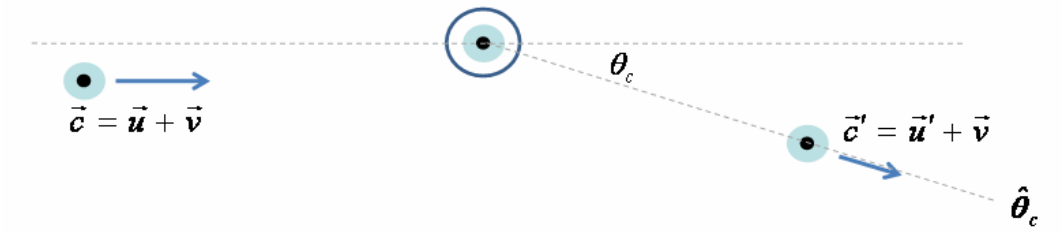

Figure 5.1: The instantaneous velocity of the trapped ion in the centre of mass reference frame before and after a collision is schematically shown.

5.1 The scope for sympathetic cooling

The ability to cool ions using the conventional techniques of buffer-gas cooling is primarily dependent upon the ratio of the masses of the ion and atom species. Such techniques have efficient cooling of the ion when it is much heavier than the atom, heating when the ion is lighter than the atom and no average exchange of energy for ions and atoms of equal mass. To show that the collisions between the trapped $^{85}Rb^{+}$ ions and the cold ^{85}Rb atoms in the MOT leads to cooling of the ions, we closely follow the early, seminal work of Major and Dehmelt [17]. In describing the ion−atom collisions, the MOT atom temperature of ≈100 μK permits us to set the velocity of the atom before a collision, $\mathbf{v_A} = 0$. If the instantaneous velocity of the ion before a collision is $\mathbf{c}$, its velocity after the collision $\mathbf{c}'$ is given by

$$\mathbf{c}' = (m_A/M)c\hat{\theta}_c + (m_I/M)\mathbf{c}, \tag{5.1}$$

where $\hat{\theta}_c$ is a unit vector oriented at an angle θ_c with respect to $\mathbf{c}$, m_I is the ion mass, m_A the atom mass and $M = m_I + m_A$ is the total mass of the two-particle system. θ_c corresponds to the angle of deflection of the ion in the centre of mass reference frame. The ion motion can be decomposed into its macromotion and its in-phase micromotion oscillation with the applied electric field [18] as shown in Fig. 5.2(a). Assuming the spatial extent of the ion-atom interaction to be small and also that the collision is almost instantaneous, the instantaneous velocities

of the ion before and after the collision are then, $\mathbf{c} = \mathbf{u} + \mathbf{v}$ and $\mathbf{c}' = \mathbf{u}' + \mathbf{v}$ respectively. Here $\mathbf{u}$ and $\mathbf{u}'$ are the respective secular velocities, $\mathbf{v} \propto \mathbf{E}sin(\phi_{RF})$, is the micromotion velocity and ϕ_{RF} is the phase of the electric field $\mathbf{E}$ at the instant of collision.

A change in the ion's macromotion velocity changes the spatial extent to which the ion oscillates subsequently in the trap and hence its average energy in a macromotion cycle of oscillation. So the quantity of interest is $\langle u'^2 - u^2 \rangle$ which gives a measure of the extent of the change in the ion's kinetic energy averaged over long times. Substituting $\mathbf{c} = \mathbf{u} + \mathbf{v}$ and $\mathbf{c}' = \mathbf{u}' + \mathbf{v}$ in Eqn. 5.1 and with some regrouping of the terms, we obtain an expression for $u'^2 - u^2$ as

$$\begin{aligned} u'^2 - u^2 = -2m_I m_A(u^2 + 2\mathbf{u}\cdot\mathbf{v} + v^2)(1 - \cos\theta_c)/M^2 \\ +2m_A(v^2 + \mathbf{u}\cdot\mathbf{v} - c\,\hat{\theta}_c\cdot\mathbf{v})/M. \end{aligned}$$

In conventional buffer gas cooling techniques, a non-reactive buffer gas in thermal equilibrium with a reservoir floods the entire ion trap volume with collisions possible at all parts of an ion's trajectory. But since the ion spends most of its time at the classical turning points of its macromotion where $\langle|\mathbf{u}|\rangle \to 0$ and $\langle|\mathbf{v}|\rangle \gg 0$, most collisions happen there and we can make the approximation $c\,\hat{\theta}_c \cdot \mathbf{v} \approx v^2 \cos\theta_c$. This results in the right hand side of 5.2 being negative for $m_A \ll m_I$ which is a case of ion cooling, positive for $m_A \gg m_I$ which leads to ion heating, and no net change of ion temperature for $m_A = m_I$ as summarized below.

$$\left\langle u'^2 - u^2 \right\rangle \approx \begin{cases} \left[\langle v^2\rangle - \langle u^2 + v^2\rangle\right](1 - \cos\theta_c)2m_A/m_I & , m_A \ll m_I \\ 2\langle v^2\rangle(1 - \cos\theta_c) & , m_A \gg m_I \\ \left[\frac{1}{2}\langle v^2\rangle - \langle u^2 + v^2\rangle\right](1 - \cos\theta_c) & , m_A = m_I \end{cases}$$

In our experiment, the cloud of cold atoms acts as the buffer gas and its density distribution is localized around the centre of the ion trap with the volume

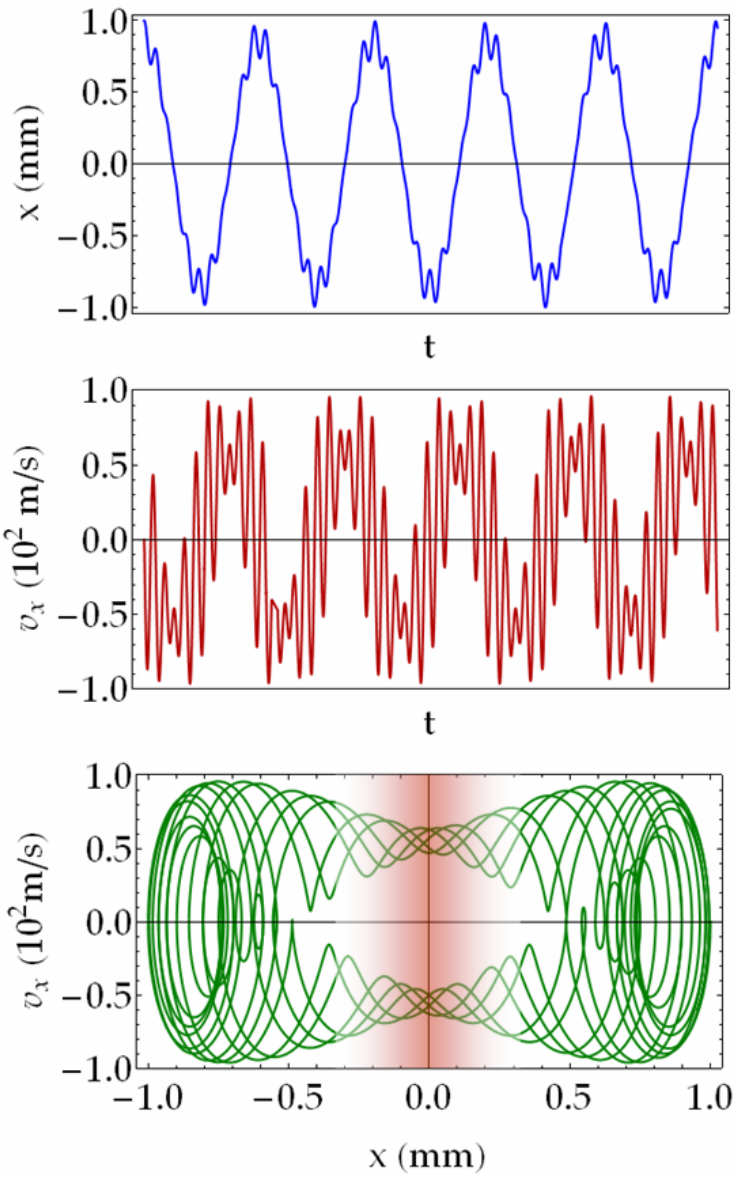

Figure 5.2: The projection of a typical trajectory of the ion on the X-axis is illustrated. Panel (a) shows the position as a function of time $x(t)$, panel (b) shows the corresponding velocity trace $v_x(t)$. Panel (c) shows the phase space plot of x versus v_x with the density profile of the atoms super-imposed on it. The ion's instantaneous velocity dramatically oscillates when it is near the classical turning points of the macromotion whereas near the $x = 0$ crossings, its value remains roughly constant. By having more collisions preferentially at the zero crossing points which is the centre of the ion trap, the average kinetic energy of the ion decreases much more efficiently than in the case of uniform density of atoms.

of trapping of the atoms being much smaller than the volume of the ion trapping region. So the ion-atom collisions happen preferentially at the centre of the trap which corresponds to the limiting case of $\langle|\mathbf{u}|\rangle \gg 0$ and $\langle|\mathbf{v}|\rangle \to 0$. This is schematically illustrated in Fig. 5.2. Evaluating Eqn. 5.2 above in this limit and after carefully taking a time average over ϕ_{RF}, we obtain the expression for $\langle u'^2 - u^2 \rangle$ as,

$$\lim_{v\to 0}\langle u'^2 - u^2\rangle \approx -2m_I m_A \langle u^2\rangle (1-\cos\theta_c)/M^2. \tag{5.2}$$

For a given deflection angle, this quantity is negative irrespective of m_I/m_A and its magnitude is highest for $m_A = m_I$. In other words, there is a reduction in the average macromotion energy of the ion in each collision and that the maximum cooling in a collision, for any particular deflection angle, occurs for the equal mass case. This indicates that a spatially compact density distribution of the buffer gas leads to the cooling of the ions. We note that most of the dephasing collisions that occur at the periphery of the ion's trajectory in conventional buffer gas cooling are heavily suppressed due to the form of the density distribution of the atoms.

The analysis above is valid for elastic scattering with a fixed scattering angle θ_c in the centre of mass frame for any general combination of ion and atom species. For the specific case of $Rb^+ - Rb$ collisions the resonant charge exchange (RCx) channel [33, 35, 42, 43] is also a dominant channel which needs to be considered in the collisions between the ions and atoms. In an RCx collision, the valence electron of the atom transfers from the atom to the ion with no other change in the dynamical or internal states of the colliding partners, apart from swapping their respective charge states. For the ion$-$atom collision energy (E) involved in the experiment, the RCx cross section [35] $\sigma_{cx} \propto 1/E^{1/2}$, is comparable to the ion-atom elastic cross section [35, 37] $\sigma_{el} \propto 1/E^{1/3}$, so both channels participate in ion cooling. In those glancing collisions where RCx occurs, the swapping of the charge state results in an ion almost at rest. This swap cooling

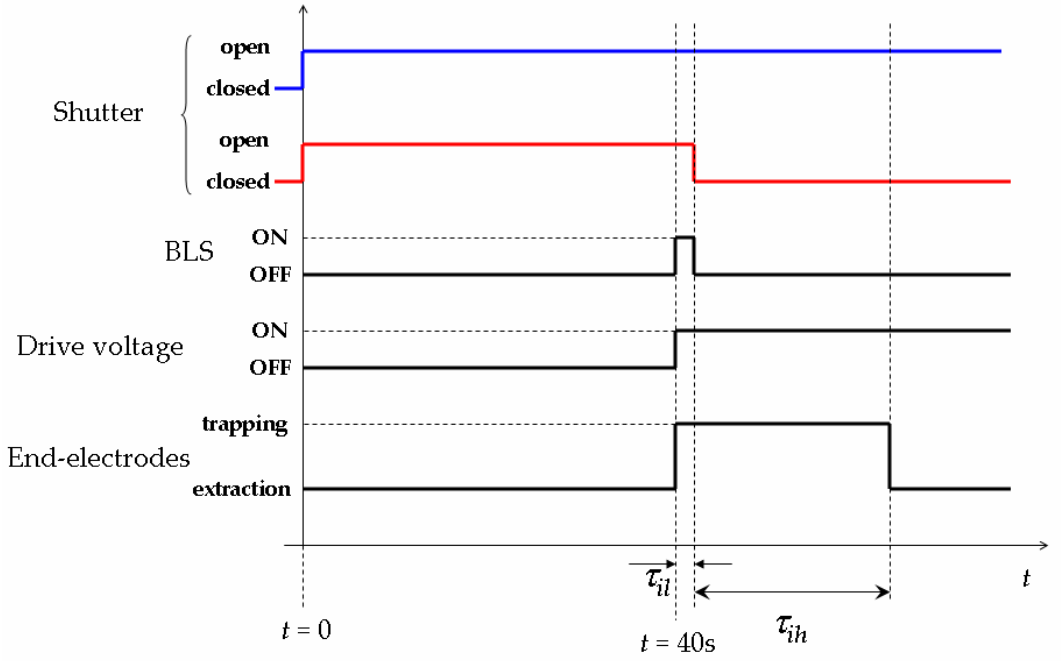

Figure 5.3: The experimental sequence of the ion-lifetime measurement for the two cases (1) without the atoms in the MOT and (2) with the atoms in the MOT. The logic pulses shown in black are common for both the cases. The shutter sequence is indicated in red for the case without MOT atoms and in blue for the case with MOT atoms.

occurs preferentially at the ion trap minimum, where the MOT density is maximum. The probability distribution for the impact parameter can be modelled as $p_b(b) \propto b$. So clearly the glancing collisions where the impact parameter is high are overwhelmingly more probable than head-on collisions where the impact parameter is low. Referring to Fig. 4.9, in the energy range where $b_{cx} \gg b_c^{el}$ the RCx mechanism for transferring energy from ions to atoms dominates the elastic channel.

5.2 Ion lifetime measurements

The above hypothesis for ion cooling by cold atoms is experimentally implemented and verified by measuring the evolution of the ion population in the trap as follows.

5.2.1 Experimental procedure

The specific sequence of the measurement is illustrated in Fig. 5.3. The Rb dispenser and the quadrupolar magnetic field for the MOT are kept ON throughout the measurement. Initially, the MOT is loaded for $\tau_{ml} = 40$ s until saturation, during which the ion trap RF field is kept OFF. Once the MOT is in saturation, the ion trap's RF field is switched ON and a small fraction of the atoms in the MOT are ionized by pulsing ON the ionizing light from the BLS for an interval of $\tau_{il} = 1$ s to load the ion trap. At the end of the ion loading interval, the cold atoms can be retained in the trap or can be ejected within a few milliseconds by simultaneously switching OFF the cooling and repumper lasers with a mechanical shutter. The ions are trapped for a further hold time, τ_{ih}, for the two cases (1) without the atoms in the MOT and (2) with the atoms in the MOT. Following this they are extracted onto the CEM. The above cycle is repeated for different values of τ_{ih} ranging from 0s to 180s. The ion count detected on the CEM is measured in the analog mode for each value of τ_{ih} separately for the

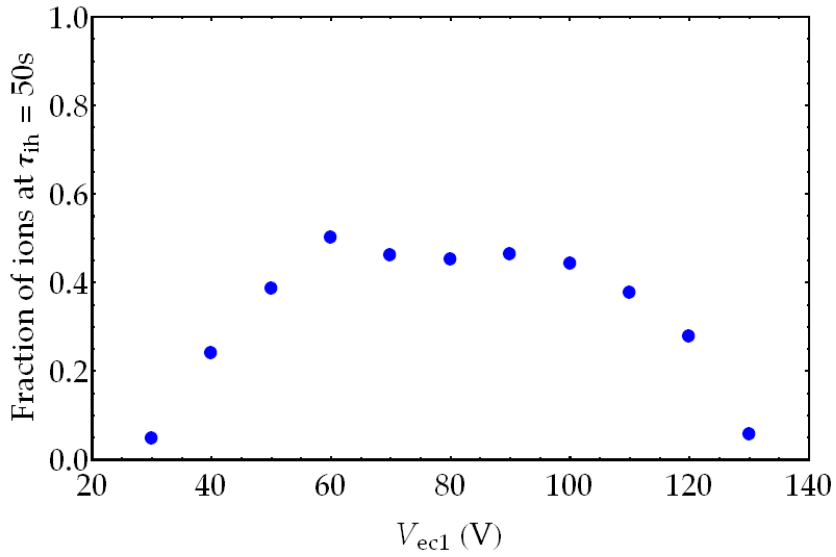

Figure 5.4: The fraction of the ion population at a hold time of $\tau_{ih} = 50$s is shown for different values of voltages on the end-electrode V_{ec1} with the voltage on the other end-electrode kept at $V_{ec2} = 80$V. The data shows a symmetric fall off of the ion fraction on either side of $V_{ec1} = 80$V.

two cases. The experiment is repeated many times to obtain sufficient statistical weight for each data point.

5.2.2 MOT-Ion trap overlap

The axial confinement for the ions is a shallow harmonic trap effected by DC voltages on the distant end-electrodes. Asymmetric DC voltages on the two end-electrodes shifts the minimum of the ion trap along the axis. We characterize the overlap between the centres of the ion trap and the MOT along the axis by shifting the ion trap centre and measuring the ion signal in the presence of the MOT at long hold times. The electrode away from the CEM is kept at a constant voltage of $V_{ec2} = 80$V and the voltage on the end-electrode near to the CEM is varied from $V_{ec1} = 30$V to $V_{ec1} = 130$V in steps of 10V. The fraction of the ion population at $\tau_{ih} = 50$s is determined in this way for different values of V_{ec1}. This fraction is plotted in Fig. 5.4. We note that the curve shows a symmet-

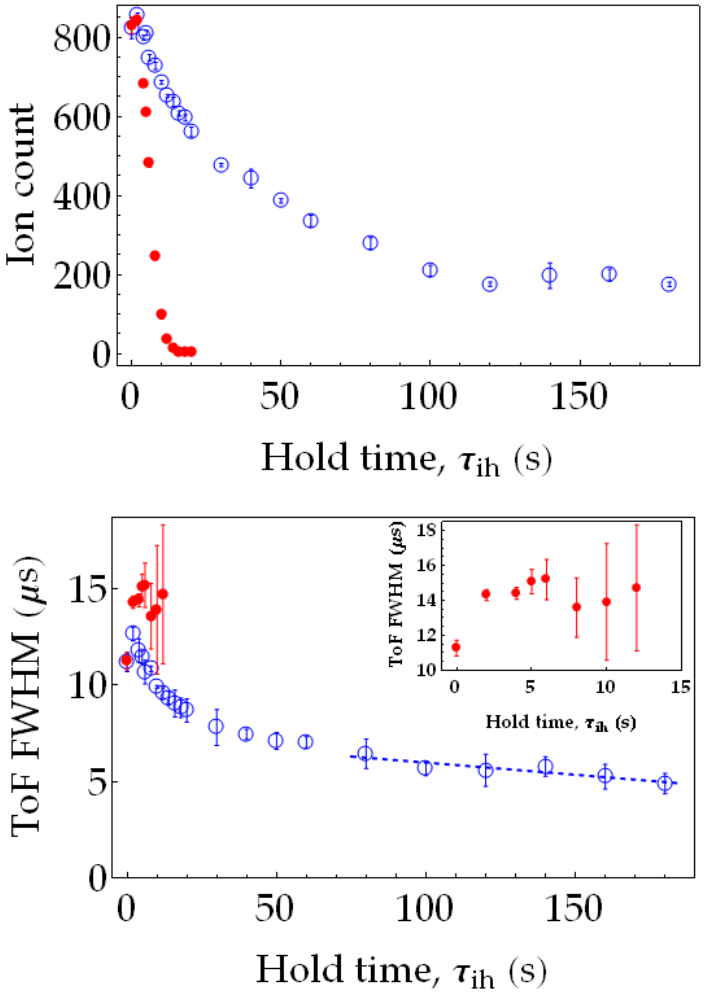

Figure 5.5: Experimental demonstration of ion cooling. Case (1) without MOT (red filled circles) and case (2) with MOT (blue empty circles). Panel (a) plots the number of Rb^+ ion counts as a function of τ_{ih}. Without a MOT, the ions exit the trap rapidly, while with cold atoms the ion loss is much slower and a stable number of ions (187 ± 9) is trapped without detectable loss beyond $\tau_{ih} \geq 2$ minutes. Panel (b) illustrates the variation of the FWHM of the ion ToF distribution against τ_{ih} for the two cases. For case (1) the FWHM increases in time as the trap empties out, while for case (2) a systematic decrease in the ion ToF distribution is seen, consistent with ion cooling. For $\tau_{ih} \geq 2$ min, when the trapped ion number has stabilized, the ToF width is still decreasing indicating continued ion cooling, as illustrated by a least square fit to the last six data points. The statistical standard deviation error-bars are shown for each data point.

ric fall off on either side of $V_{ec1} = 80$V. Though the absolute minimum within the limits of experimental error is not at this point, the general shape of the curve indicates a maximum overlap between the two traps on the axis when the ion trap end-electrodes are biased symmetrically. This ascertains that the ion-atom interaction is maximized at $V_{ec1} = V_{ec2} = 80$V and the experimental measurements are performed at this value.

5.2.3 Observations

The CEM ion counts vs. τ_{ih} is plotted in Fig. 5.5(a). The analog mode signal from the CEM has the shape of an envelope with a certain width. The FWHM of this envelope is a measure of the width of the ion arrival time-of-flight (ToF) distribution and is shown in Fig. 5.5(b). For case (1) all the ions exit the trap by $\tau_{ih} \approx 15$ s and the ToF FWHM increases rapidly. In case (2) for $\tau_{ih} \geq 1$ s, the ion loss rate from the trap is drastically reduced and the FWHM of the ion ToF distribution decreases with increasing hold time. Beyond $\tau_{ih} \geq 2$ minutes, the number of trapped ions stabilizes to a constant value, while the width of the ToF distribution nominally decreases. Intuitively, the ToF width gives a measure of the temperature of the ion cloud with a larger ToF width corresponding to a higher temperature and vice versa. So the experimental data of Fig. 5.5 indicates that though the number of ions detected is roughly constant, the ion cooling process is still underway at $\tau_{ih} = 180s$. We infer from this data that a number equilibrium between daughter ions and laser cooled parent atoms is established and achieving a thermally stable equilibrium is within experimental means.

5.3 Model for the ion heating in the absence of atoms

To get a quantitative picture of the cooling mechanisms involved in our system, we first need to estimate the rate of heating of the ions in the absence of the MOT atoms. For this a Monte-Carlo calculation for a non interacting distribution of

ions in the absence of atoms is performed to model the loss of ions from the trap. In the absence of the atoms, there is no cooling mechanism for the ions and the ion cloud is dilute which means that the ion trajectories are mostly independent of each other except for occasional dephasing collisions which heat them up. The ions can also heat due to other factors such as trap imperfections and finite linewidth of the drive voltage. We assume a homogeneous exponential anti-damping factor Γ to collectively represent these mechanisms of ion heating over long time scales.

5.3.1 The envelope of maximum energy

Consider an ion initially at a point (x_i, y_i, z_i) in a linear Paul trap operating at a radio frequency voltage of amplitude V_{rf} and frequency Ω. The Mathieu stability parameter in the radial direction is $q = 2eV_{rf}/(m_I \Omega r_0^2)$ where r_0 is a geometrical constant of the trap. Let the secular frequencies in the radial and axial direction be ω_r and ω_z respectively. For $q \ll 1$, the ion's trajectory in the presence of an anti-damping factor Γ is given by

$$\begin{aligned} x(t) &= x_0 \cos(\omega_r t)\left[1 + \frac{q}{2}\cos(\Omega t)\right] \exp\left[\frac{\Gamma}{2m_I}t\right] \\ y(t) &= y_0 \cos(\omega_r t)\left[1 - \frac{q}{2}\cos(\Omega t)\right] \exp\left[\frac{\Gamma}{2m_I}t\right] \\ z(t) &= z_0 \cos(\omega_z t) \exp\left[\frac{\Gamma}{2m_I}t\right] \end{aligned} \tag{5.3}$$

The energy of the ion rapidly oscillates between zero and a maximum value and this maximum value changes over time under the influence of Γ. The time-derivatives of Eqn. refEq:traj give the corresponding instantaneous velocities. Squaring each velocity, we substitute the quadratic oscillatory terms with the corresponding maximum values and neglect the linear oscillatory terms. The remaining time dependence is in the form the exponential anti-damping factor.

The maximum kinetic energy contributions from each direction are obtained as

$$\begin{aligned}
\frac{1}{2}m_I(X'(t))^2 &\approx \frac{1}{2}m_I x_0^2 \exp\left(\frac{\Gamma}{m_I}t\right)\left[\left(\omega_r^2+\frac{\Gamma^2}{4m_I^2}\right)+\frac{q^2}{4}\left(\Omega^2+\omega_r^2+\frac{\Gamma^2}{4m_I^2}\right)\right] \\
\frac{1}{2}m_I(Y'(t))^2 &\approx \frac{1}{2}m_I y_0^2 \exp\left(\frac{\Gamma}{m_I}t\right)\left[\left(\omega_r^2+\frac{\Gamma^2}{4m_I^2}\right)+\frac{q^2}{4}\left(\Omega^2+\omega_r^2+\frac{\Gamma^2}{4m_I^2}\right)\right] \\
\frac{1}{2}m_I(Z'(t))^2 &\approx \frac{1}{2}m_I z_0^2 \exp\left(\frac{\Gamma}{m_I}t\right)\omega_z^2
\end{aligned} \tag{5.4}$$

Summing these, the evolution of the total energy of the ion, including the micromotion is subsequently obtained as

$$E(t)=\frac{1}{2}m_I \exp\left[\frac{\Gamma}{m_I}t\right]\left[(x_0^2+y_0^2)\left\{\left(\omega_r^2+\frac{\Gamma^2}{4m_I^2}\right)+\frac{q^2}{4}\left(\Omega^2+\omega_r^2+\frac{\Gamma^2}{4m_I^2}\right)\right\}+z_0^2\omega_z^2\right] \tag{5.5}$$

When q is not so small compared to unity like in our experiment, the expression for the ion's trajectory is not well represented by Eqn. 5.3. But the expression for the energy envelope Eqn. 5.5 still remains a good approximation and can be used for calculations that take only the overall energy envelope into account.

If E_{ej} is the maximum kinetic energy that the ion can possess including the micromotion and still remain in the trap, the time t_{ej} at which the ion reaches a kinetic energy of E_{ej} is obtained by inverting Eqn. 5.5 as

$$t_{ej}=\frac{m_I}{\Gamma}\log\left[\frac{2E_{ej}}{m_I\left[(x_0^2+y_0^2)\left\{\left(\omega_r^2+\frac{\Gamma^2}{4m_I^2}\right)+\frac{q^2}{4}\left(\Omega^2+\omega_r^2+\frac{\Gamma^2}{4m_I^2}\right)\right\}+z_0^2\omega_z^2\right]}\right] \tag{5.6}$$

where $x_0 = x_i/(1+q/2)$, $y_0 = y_i/(1-q/2)$ and $z_0 = z_i$, Ω is the drive frequency, q is the Mathieu stability parameter and ω_r and ω_z are the secular oscillation frequencies in the radial and axial directions respectively.

5.3.2 Monte-Carlo

A large number of samples of (x_i, y_i, z_i) are generated consistent with the density distribution of the MOT from which the ions are initially created. Assuming

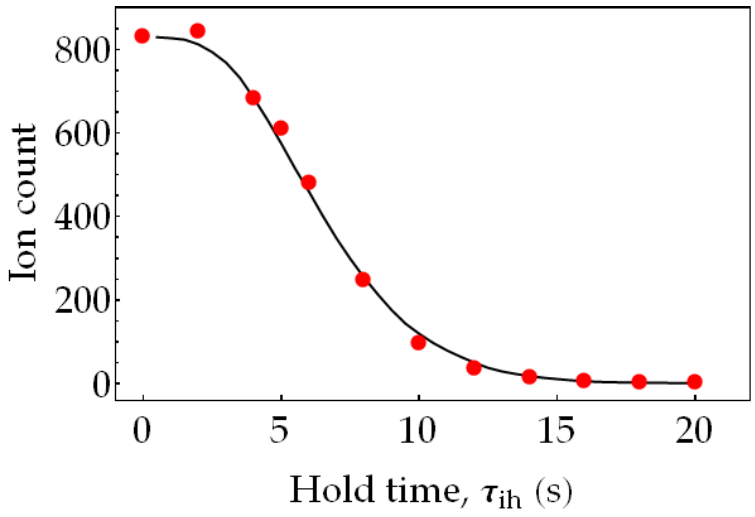

Figure 5.6: The measured ion counts (red circles) as a function of hold time is shown to be fitted with a function (black solid line) obtained by the non-interacting ion Monte-Carlo model.

that an ion exits the trap when its total energy exceeds a particular value E_{ej}, we can calculate the time of ejection t_{ej} of the ion for each of these initial positions using Eqn. 5.6.

The cumulative probability distribution for t_{ej} gives the fraction of ions ejected from the trap at a certain time t_{ej}. From this we determine the fraction of ions remaining in the trap at different times with respect to the initial population. The model curve is compared with the measured data of Fig. 5.5(a) in the absence of MOT atoms for different values of Γ and E_{ej} and the pair of (Γ, E_{ej}) for which the χ^2 is minimized is taken as the final values for the model. The model and the data are shown in Fig. 5.6 for $\Gamma = 0.57 \times 10^{-25}$ kg s^{-1} and $E_{ej} = 2.83$ eV. This value of E_{ej} corresponds to an average secular motion energy of 0.8eV.

5.4 Estimating the ion temperature

In order to get an estimate of the temperature of the ion cloud for the width of the time of flight distribution, we numerically simulate the process of the detection of ions from different initial conditions. We generate positions and

velocities of two hundred interacting ions for the instant just before they are extracted on to the detector. The spatial distribution is taken to be Gaussian with the standard deviations (σ_x, σ_y, σ_z) in each direction to be inversely proportional to the square of the respective secular motion frequencies (ω_r, ω_z) with $\sigma_x^2\omega_r^2 = \sigma_y^2\omega_r^2 = \sigma_z^2\omega_z^2$. The velocities are sampled from a Maxwellian distribution corresponding to a temperature T. This velocity distribution is assumed to be independent of the spatial distribution. This is a reasonable assumption to make given that the time of ion creation and the eventual evolution of the ions in the presence of collisions is a stochastic process. From these initial conditions, we evolve the motion of the interacting ions using a molecular dynamics framework under the influence of the transient extraction voltages of the trap. The arrival times of the ions at the detector area is determined and the specifics of the detection circuit's frequency response are incorporated to obtain an integrated waveform. The FWHM of this waveform is determined for different values of σ_z and T, fitted with a surface and plotted as shown in Fig. 5.7.

5.5 Simulating the ion-atom collisions

To better understand the data of Fig. 5.5(a) in the presence of the MOT, we need to adapt the general ion-atom collision calculations of Chapter 4 to the context of our combined ion-atom trap. This is quite a challenging exercise for the following reasons:

1. There are multiple collisions involved for each ion.

2. The ion trajectories are non-linear and there are large variations in the instantaneous velocities. This complicates the situation especially when the cross-sections have an energy dependence.

3. The trajectories are further complicated by the presence of Coulomb repulsion of the ions.

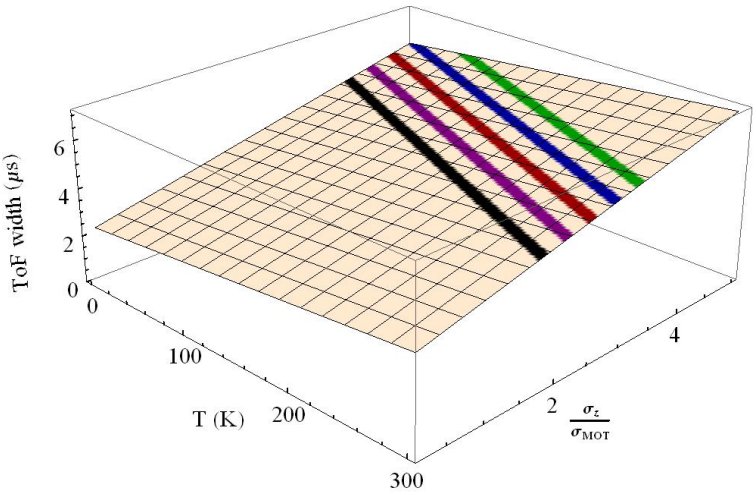

Figure 5.7: The results of the extraction simulations. The width of the ion TOF distribution is plotted against the size of the ion cloud and the temperature just before extraction. The size of the ion cloud is represented by the standard deviation along the axial direction normalized with the standard deviation of the atom distribution. The bands on the surface indicate the loci of equal ToF width corresponding to five values of hold times in the presence of the MOT. The bands are coded as Green$\rightarrow$ $\tau_{ih} = 100s$, Blue$\rightarrow$ $\tau_{ih} = 120s$, Red$\rightarrow$ $\tau_{ih} = 140s$, Violet$\rightarrow$ $\tau_{ih} = 160s$ and Black$\rightarrow$ $\tau_{ih} = 180s$.

4. The density distribution of the atoms is non-uniform and the ions are moving through this in non-linear paths.

Given these challenges, in the following sections we attempt to, semi-quantitatively characterize the interactions with numerical simulations. Our main aim is to establish that:

- The algorithms described below qualitatively demonstrate our cooling hypothesis for a non-uniform density distribution of atoms.
- The cooling is active when only the elastic collisions are active.
- The presence of resonant charge exchange collisions indeed accelerates the cooling process.
- The general qualitative trends and the time-scales of evolution of the observed ion population are reflected by the simulations.

5.6 Simulation: The elastic and RCx channels

We first describe the simulations that compare the elastic and RCx channels for their role in the cooling of the ions. Trajectories of hundred non-interacting trapped ions are computed, each undergoing multiple collisions within a Gaussian density distribution (standard deviation of $=$ 0.43mm) of atoms about the ion trap centre. The ions are evolved in the analytical potential given by Eqn. 2.6, from a random initial position distribution which is much bigger than the extent of the atomic distribution. The computation is done separately for elastic collisions only and for elastic and RCx collisions combined. The ion$-$atom binary interaction potential described in Chapter 4 determines the specifics of the scattering event. All collisions are instantaneous and the time between collisions is sampled from a Poisson distribution with a mean of 20 rf cycles chosen

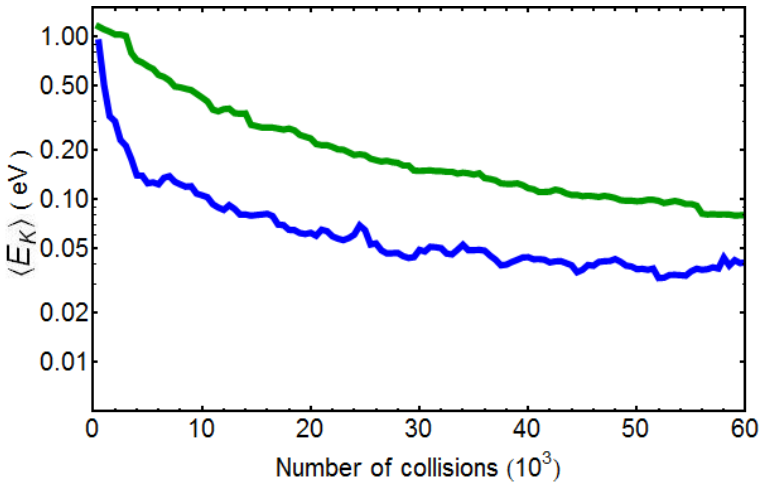

Figure 5.8: The fall in average ion kinetic energy ($\langle E_K \rangle$) as a function of the total number of collision events (which corresponds directly to evolution time) for the simulation of 100 independent ions with the localized atoms. Here the green triangles represent elastic and the blue circles represent elastic+RCx collisions. In both cases $\langle E_K \rangle$ decreases with collision number. However, we note that for the elastic+RCx collision, the reduction in $\langle E_K \rangle$ is much faster when the ions are more energetic.

to balance the experimental reality and the computational constraints. Each collision occurs with an impact parameter b chosen from a probability distribution $p_b(b) \propto b$ such that $0 < b < b_{max}$ where b_{max} corresponds to a scattering angle $\theta_c > 60\mu$ radians. The collision results in the change of ion velocity from $\mathbf{c} \rightarrow \mathbf{c}'$. When $b < b_{cx}$, we account for a 50% probability for charge exchange to occur. The kinematics of the collision are computed as described in Chapter 4. The computed kinematic states of the ion and the atom are interchanged when charge exchange takes place.

The mean ion kinetic energy for the cases where only the elastic channel is active and both elastic and RCx channels are active is shown in Fig. 5.8. Ion cooling is clear from the reduction of mean kinetic energy per ion of the non-interacting ions in the trap with time. The step changes in the kinetic energy occur for either a head on elastic or glancing RCx collision at the trap bottom. The ions cool much faster when the RCx channel is active along with the elastic

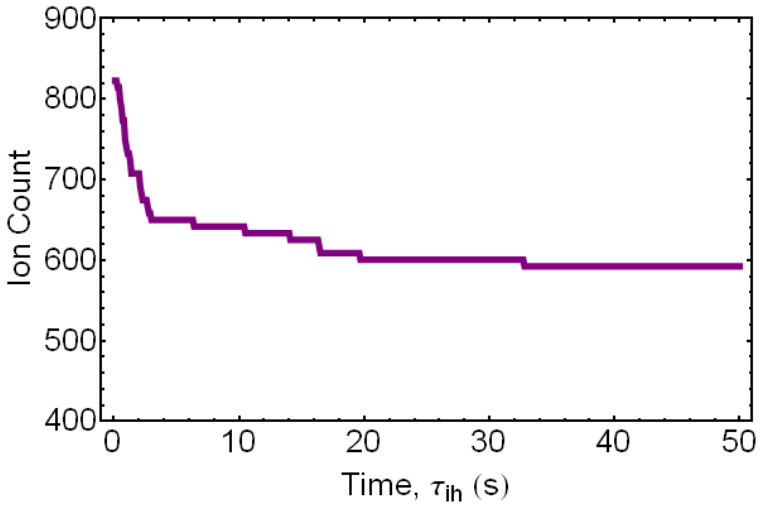

Figure 5.9: The evolution of the ion population with hold time τ_{ih} as computed from the multiple collision simulations in the presence of the exponential anti-damping factor. The simulations give the fraction of the initial ion population which is scaled to the experimentally observed ion population at $\tau_{ih} = 0$. We note that this is qualitatively similar to the blue trace of Fig. 5.5(a).

one. The initial spatial distribution of the ions is taken to be much bigger than the FWHM of the atom density distribution to emphasize the role of compactness in the distribution of atoms for ion cooling.

5.7 Simulation: Collisions in the presence of ion heating

To model the data of Fig. 5.5(a) in the presence of the MOT, we combine the methods of Sections 5.3 and 5.6. The values for the anti-damping factor and the maximum trappable kinetic energy computed in Section 5.3 are used to model the evolution of the ion population in the presence of the atoms. We perform the multiple-collision numerical simulations of Section 5.6 for hundred non-interacting ions in the presence of the anti-damping factor Γ but this time we sample their initial positions from the density distribution of the MOT

($\sigma = 0.43$mm and peak density of $1.8 \times 10^{15}\text{m}^{-3}$). We sample an impact parameter b for each collision such that $0 < b < b_{max}$ with a probability distribution $p_b(b) \propto b$ as before. However, to realistically represent the time-scales of the measured data, after every collision we estimate the average macromotion-speed $\langle u \rangle$ of the ion and the average atomic density $\overline{n}$ that it passes through. From this we dynamically determine the time interval before the next collision as $T_{coll} = \overline{n}\sigma_s \langle u \rangle$ where $\sigma_s = \pi b_{max}^2$ is a hypothetical cross-section corresponding to the maximum sampled impact parameter. The calculated ion trajectories are then analysed to determine the fraction of the ion population remaining in the trap (with energy less than E_{ej}) as a function of time. Both the elastic and the RCx channels are incorporated in the simulations as described in Section 5.6. The results of this simulation are shown in Fig. 5.9. Owing to the simplicity of the approach, it shows only a qualitative correspondence to the blue trace of Fig. 5.5(a). The anti-damping factor that we calculated for the case without the MOT is valid for a dilute cloud of ions. However, in the presence of the collisional cooling, the density of the ion cloud increases and the non-interacting ion model with a single anti-damping factor is no longer a good approximation. Also, the other channels of ion-atom collisions such as the charge exchange between an excited state atom and an ion have not been incorporated into the simulation.

CHAPTER 6

Conclusions

6.1 Summary of the results

We have designed a combined trap that confines $^{85}Rb^{+}$ ions and cold ^{85}Rb atoms simultaneously with spatial overlap. The established technology of Magneto Optical Trap (MOT) has been adopted to cool and trap the atoms. A modified linear Paul trap, that can simultaneously accommodate the MOT in the same region of trapping, is designed to confine the ions. The different regimes of operation of the ion trap and the effect of one trap on the other have been numerically simulated and characterized.

The numerically validated trap design has been successfully implemented and constructed. The simultaneous confinement of ions and cold atoms in this trap has been demonstrated with an indirect, destructive detection technique implemented for the optically dark $^{85}Rb^{+}$ ions. The fluorescence from the atoms has been measured to estimate the total number of atoms in the trap and their density distribution. The parameter space of the ion trap has been scanned to experimentally determine the stable regions of ion trapping. Generic sequences and protocols have been formulated and implemented to perform experimental studies on the ion-atom ensemble.

The elastic and resonant charge exchange collisions between the $^{85}Rb^{+}$ ions and the ^{85}Rb atoms have been identified as the primary channels in our system. The kinematics and mechanisms of these collisions involving ions and atoms in their ground state have been formalized in the energy regimes that are relevant to our experiment.

The conventional methods of buffer gas cooling of ions have established that

the ion cooling is possible only when the mass of the buffer gas atom is much less than that of the ion. The ion is expected to heat when the mass of the atom is much greater than that of the ion and no significant exchange in energy takes place for the case of equal masses. In this work, a hypothesis has been proposed for the cooling of ions by collisions with atoms in a spatially compact distribution, for all mass ratios, contrary to the above expectations. This hypothesis is studied for the case of $^{85}Rb^{+}$ ions colliding with equal mass ^{85}Rb atoms in the MOT. The role of elastic collisions and resonant charge exchange collisions in the cooling process have been studied by performing multiple-scattering numerical simulations. The hypothesis for cooling is shown to be valid when purely elastic collisions are present and the cooling process is shown to be accelerated in the presence of resonant charge exchange collisions. The glancing collisions where resonant charge exchange occurs is highlighted as an important mechanism of cooling, where in a fast ion colliding with an atom at rest can result in a slow ion and a fast atom.

The time evolution of the $^{85}Rb^{+}$ ion population in the ion trap has been experimentally studied in the presence and absence of the ^{85}Rb atoms in the MOT as a function of the hold time. Significantly longer trapping times of the ions in the presence of the MOT atoms are observed compared to that in the absence of the MOT atoms, with all other conditions remaining the same. This is argued to be a stand-alone signature of ion cooling, thus verifying the above hypothesis. The number of ions in the trap, after being in contact with the MOT atoms for a hold time greater than 2min, is shown to be stabilized at a constant value within the limits of experimental error. The width of the ion arrival time distribution at the detector, which is a measure of the ion temperature, has been measured as a function of the hold time and shows a qualitative signature of ion cooling.

A Monte-Carlo simulation has been performed to model the experimentally measured evolution of the trapped ion population in the absence of the MOT.

A single exponential anti-damping factor is assumed to collectively represent all the ion heating mechanisms and the functional form of the ion evolution given by this simulation shows good agreement with the observed data and we achieve quantitative agreement with a two-parameter fit. The anti-damping factor hence derived has been used in conjunction with the multiple scattering simulation to get the qualitative features of ion stability in the presence of atoms. Finally, the process of detection of the ions is numerically modelled for different initial position and velocity distributions of the ions to obtain a correspondence between the observed width of the ion arrival time distribution and the temperature of the ions in the trap. The range of temperatures and cloud sizes which correspond to the observed widths have been established.

6.2 Perspectives and future challenges

The scope of the present work has mainly focussed on the system of $^{85}Rb^{+}$ ions and cold ^{85}Rb atoms. The study of ion-atom collisions in the combined trap can be extended to other species of atoms and ions and their different isotopes. Experiments with two different isotopes, for example $^{85}Rb^{+}$ ions and ^{87}Rb atoms, can give a comparison between the resonant and non-resonant charge exchange collisions while at the same time having almost equal masses. Relative collision rates between the different channels can be determined by comparative studies. The cooling hypothesis presented here has been verified only for the $^{85}Rb^{+}$ - ^{85}Rb equal mass combination. Using a heavier species of ions or atoms, the hypothesis can be verified for unequal mass ratios. The numerical simulations of the ion-atom collisions in the present work, have been confined to the scattering of ions and atoms in their ground states. However, the system such as a MOT, has stochastic excitations and de-excitations of atoms between the ground and excited states. The numerical study of charge-exchange collisions in such a time-varying, stochastic framework is a challenging problem. The state of

thermal equilibrium of the ions and the path to this equilibrium in the presence of atoms is an interesting problem that can be further studied both experimentally and numerically on this system. The intrinsically stabilized system of ions and atoms can be used to probe the effect of the ion-atom interaction on the photo-association of the atoms. This would potentially be the first step towards the long term scientific goals of cold-chemistry and many-body studies in the combined ion-atom system.

APPENDIX **A**

Mechanical drawings of the ion trap

Given below are the mechanical drawings of the ion trap assembly. Each figure shows a specific part of the assembly with the relevant dimensions and the material and quantity required. All dimensions are in mm. The components shown here are to be used in conjunction with a vacuum chamber (Kimball Physics: MCF600-SHD20000.16) and its associated groove grabbers (Kimball Physics: MCF600-GG-CR04-A). For clarity, the fasteners required to secure the the assembly are not shown in the drawings.

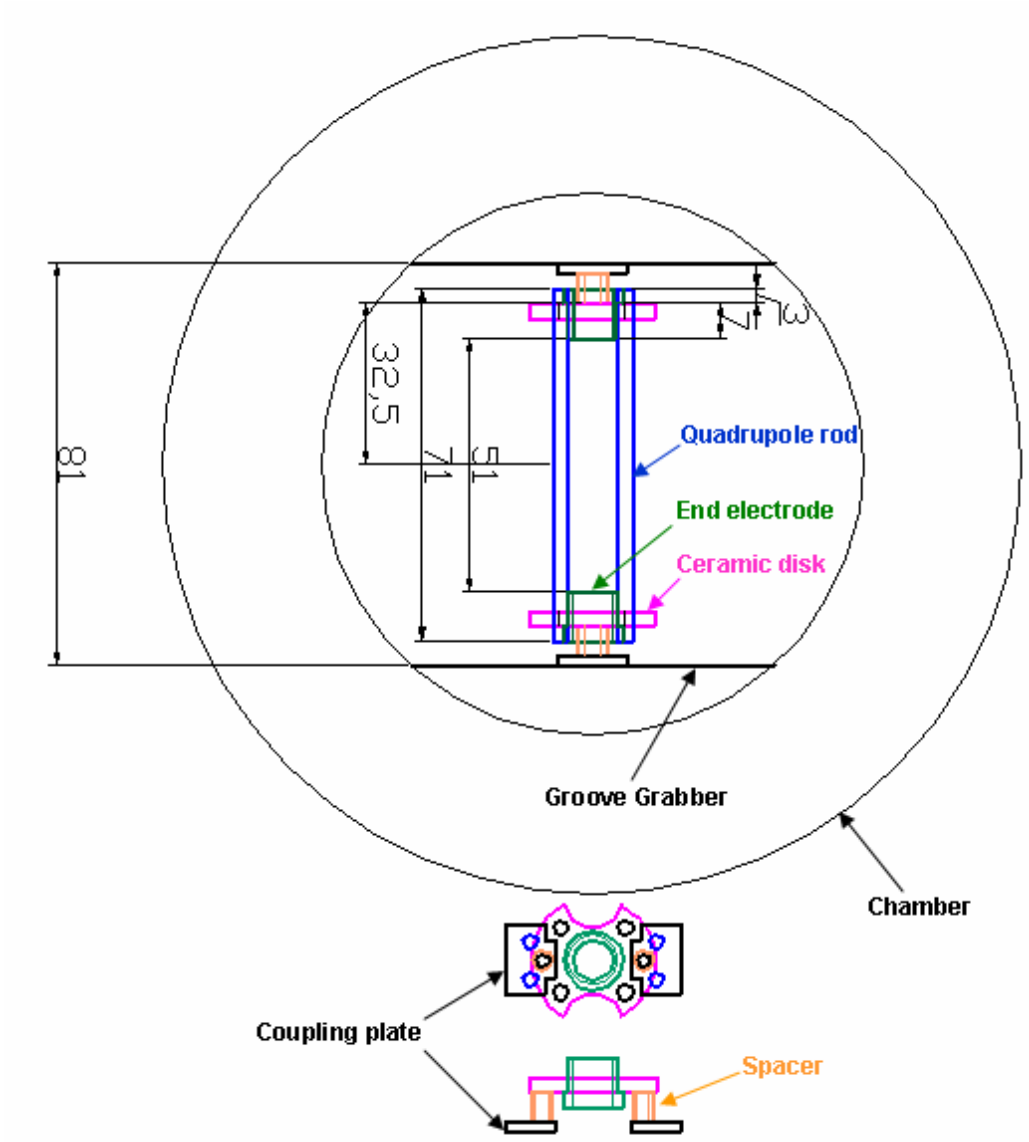

Figure A.1: Layout: The layout of the ion trap in the chamber in top view with all the components overlayed.

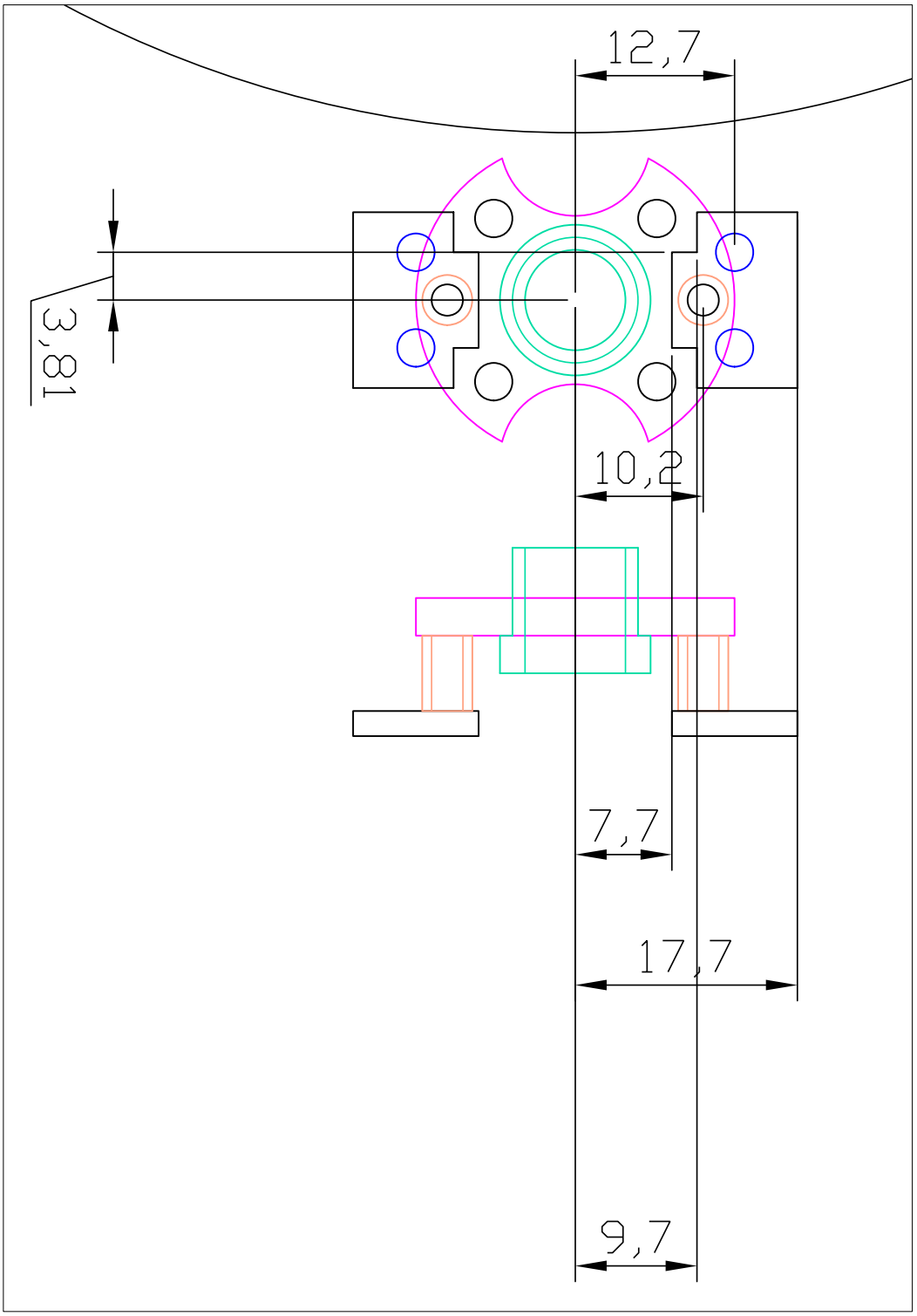

Figure A.2: A zoomed in part of Fig. A.1 showing the ceramic disk and the groove-grabber coupling arrangement.

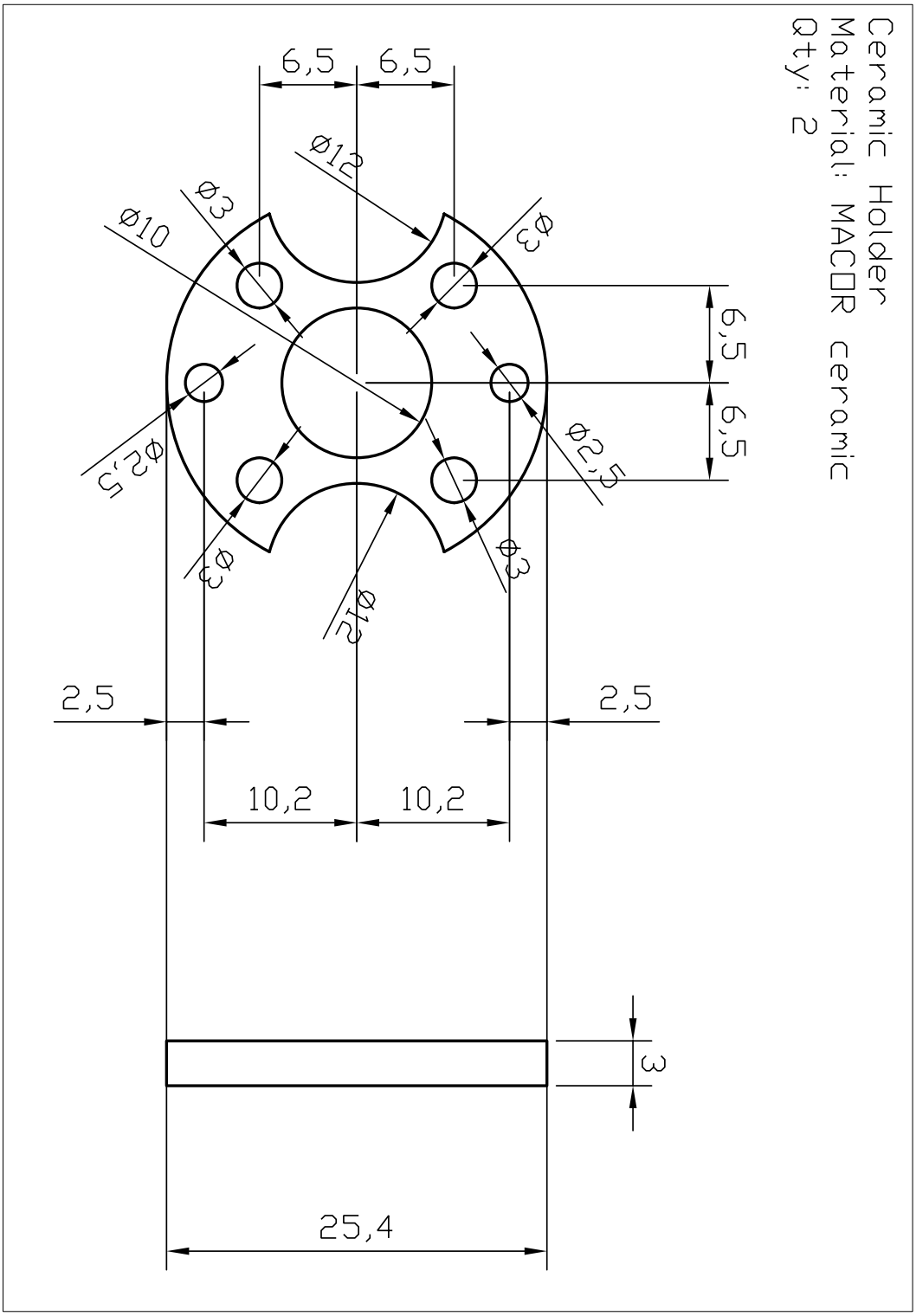

Figure A.3: Ceramic disk: The detailed dimensions of the ceramic holder that is used to hold the quadrupole rods of the ion trap.

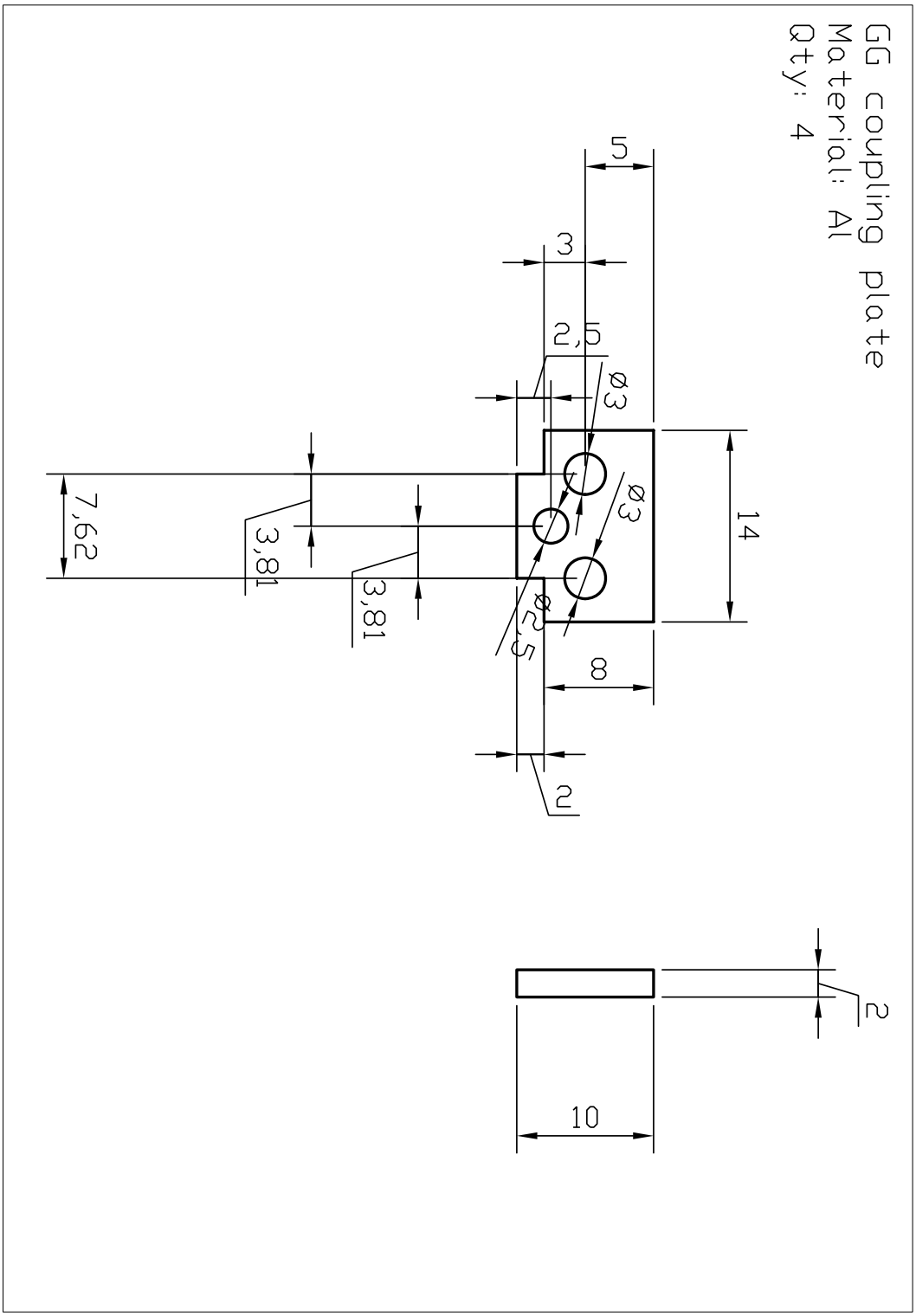

Figure A.4: Coupling plate: This plate couples the ceramic disk to the groove grabbers and hence to the chamber.

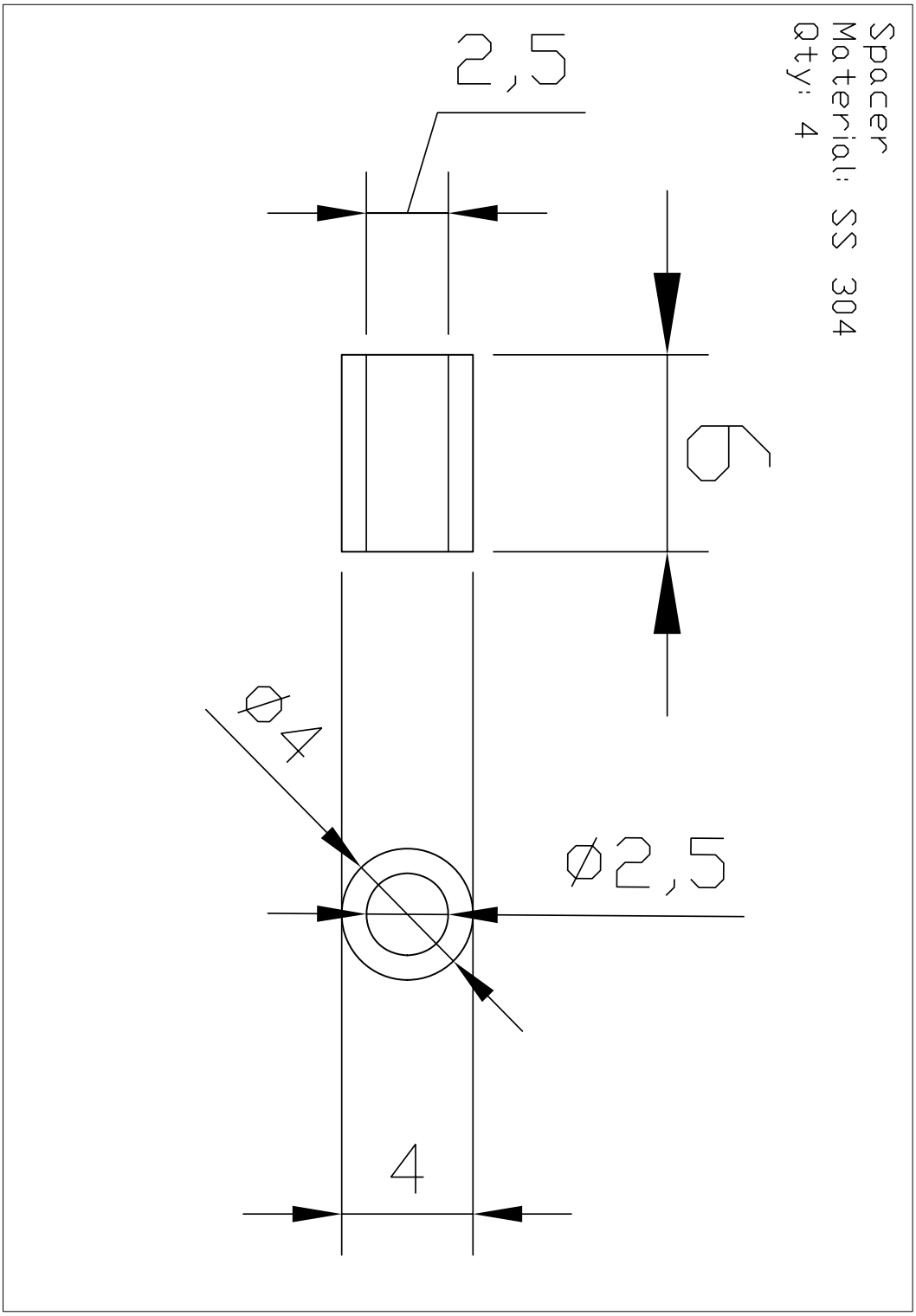

Figure A.5: Spacer: This component introduces a rigid spacing between the ceramic disk and the coupling plate.

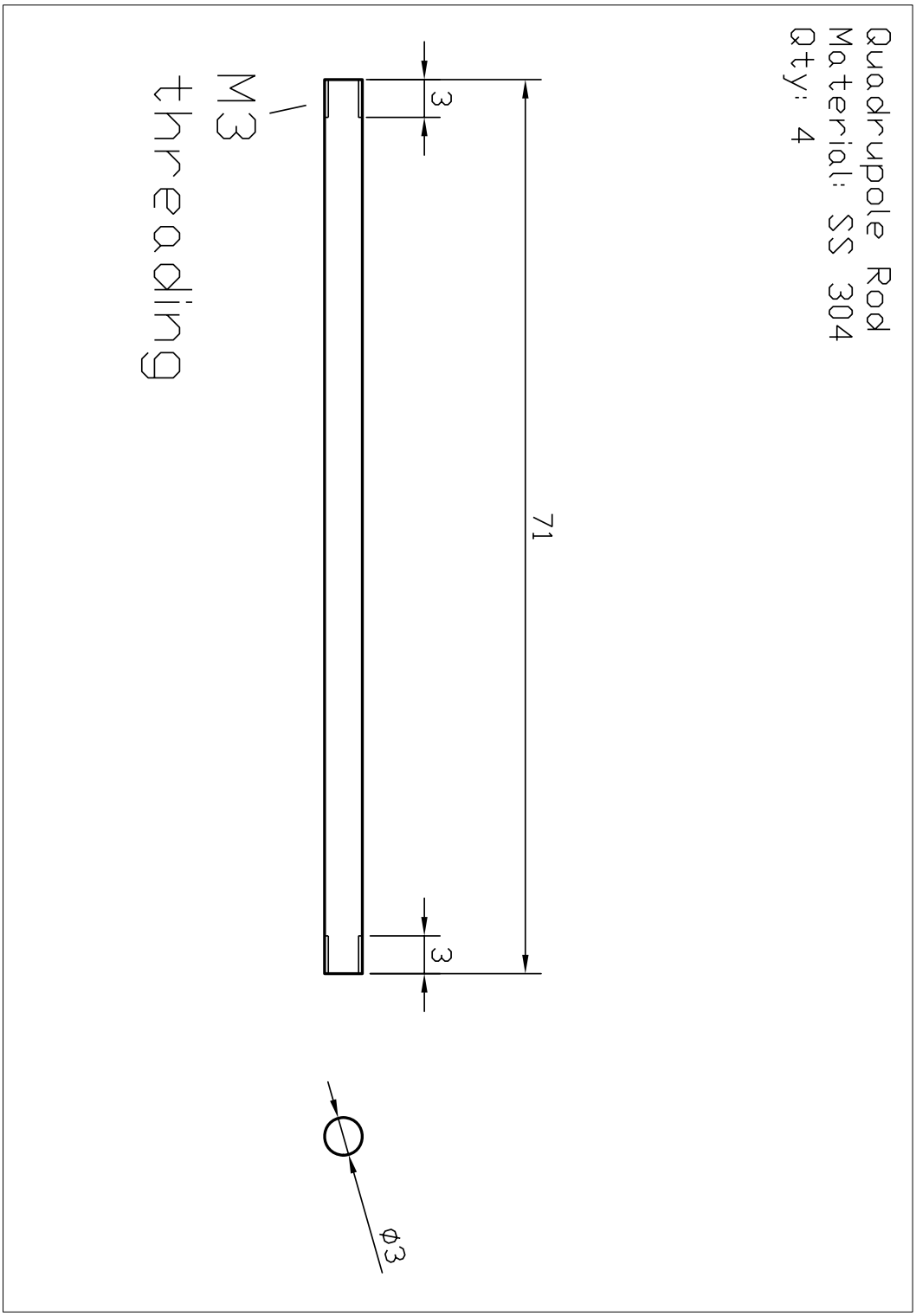

Figure A.6: Quadrupole rod: The quadrupole rods of the ion trap that are inserted into the four corresponding holes of the ceramic disks.

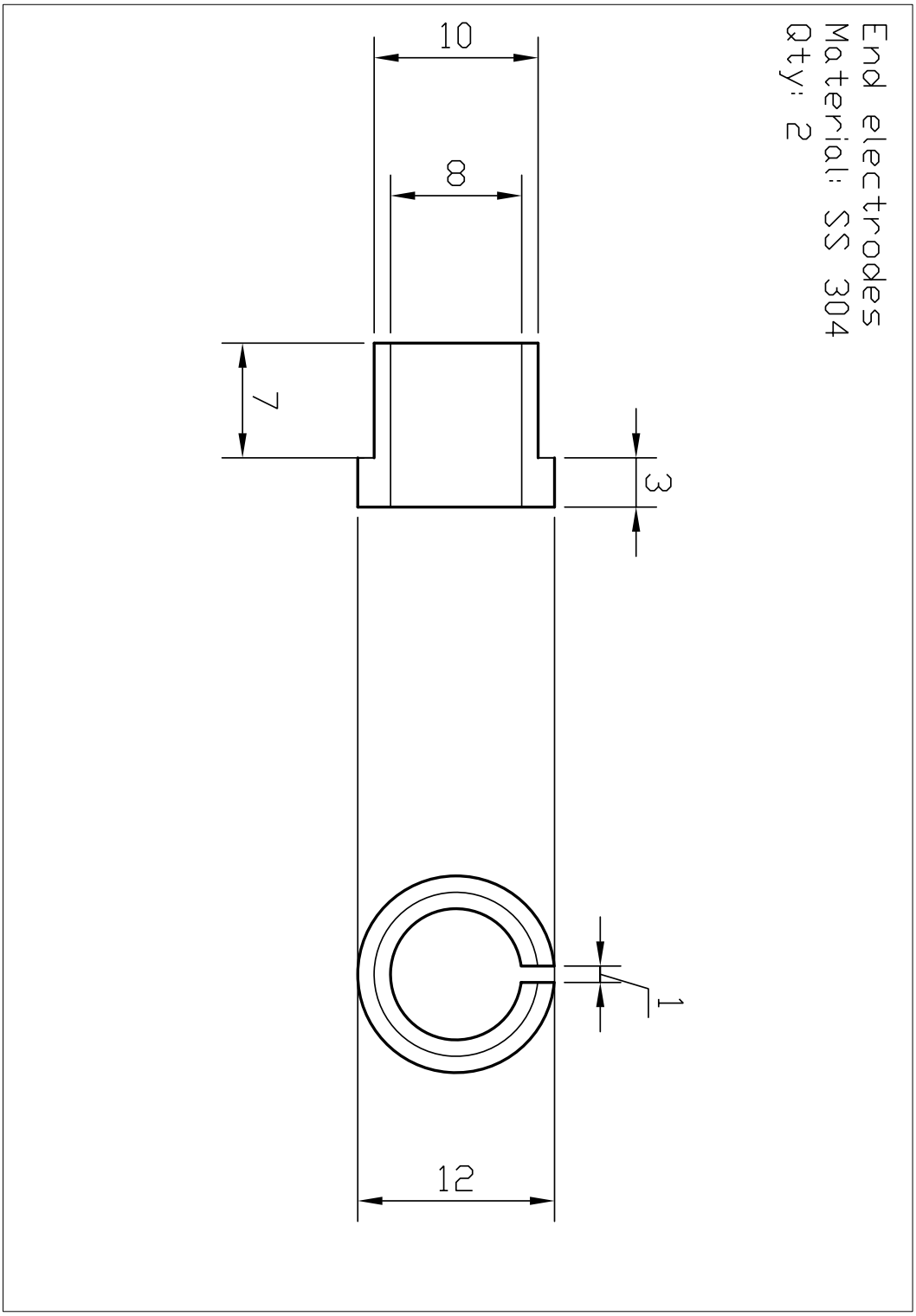

Figure A.7: End electrodes: The ring shaped end-electrodes of the ion trap that are inserted into the central holes of the ceramic disks by a push-fit arrangement.

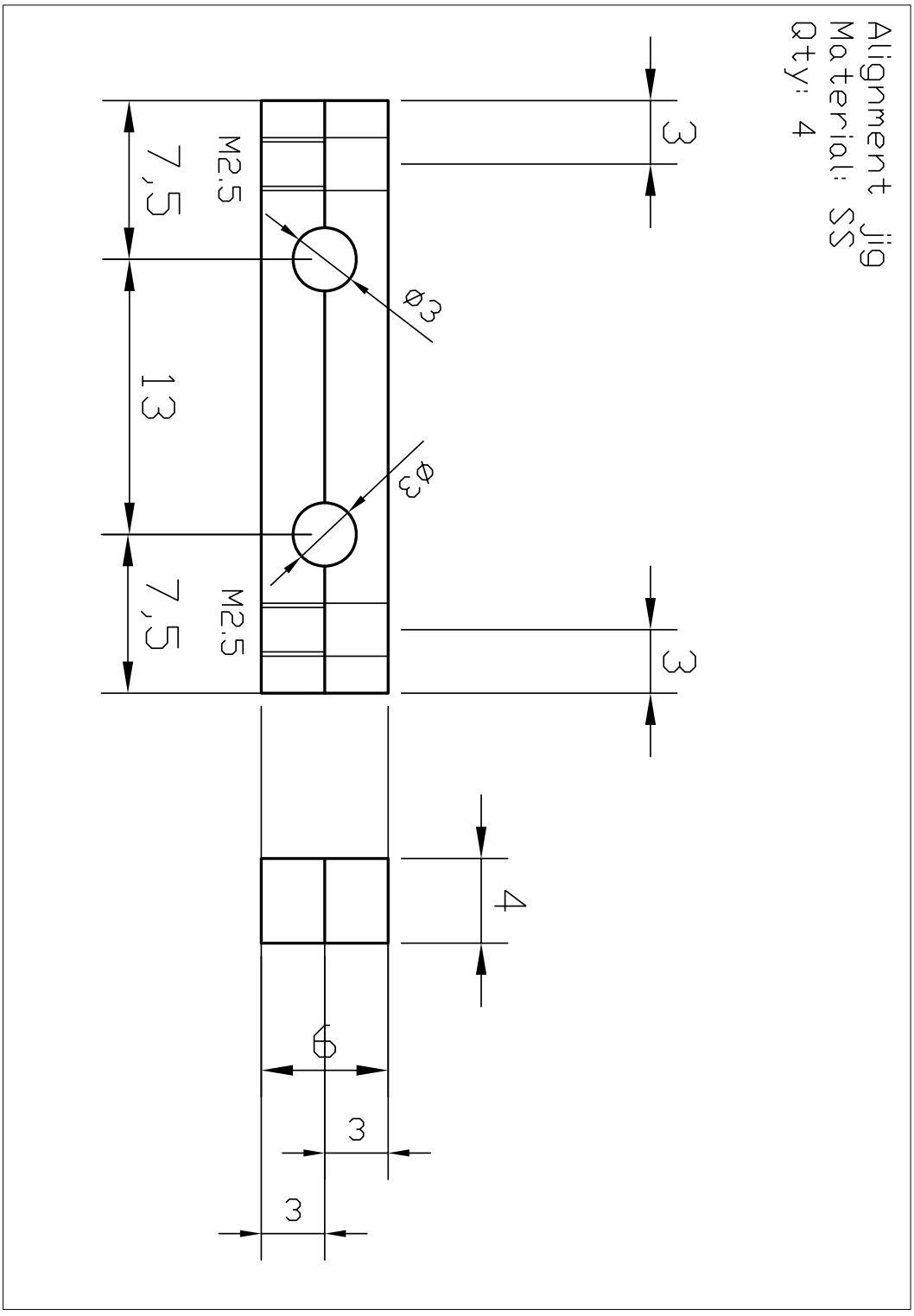

Figure A.8: Alignment jig: Four of these jigs are fastened onto each pair of adjacent quadrupole rods to align their axes with respect to each other. Once the ion trap is fully assembled, these jigs are dismantled.

APPENDIX **B**

List of computer programs

Various programs have been used throughout this work for ion trap design, numerical simulations of the dynamics of ions, experimental control and study of ion-atom collisions. Given below is a list of the important programs. These are available on request from the research group.

1. AutoCAD2000 files for the mechanical design of the ion trap assembly shown in Appendix A

2. Stability of a single ion in the ion trap in the presence and absence of a quadrupolar nagnetic field

3. Estimation of the probability of resonant charge exchange as a function of impact parameter, from the molecular potential energy curves

4. Collisions of an ensemble of non-interacting ions with atoms in a MOT in the absence of heating. This program is used to compare the efficiency of ion cooling between different collision channels.

5. Monte-Carlo simulation of the ion's heating in the absence of atoms, modelled by a single exponential anti-damping factor.

6. Collisions of an ensemble of non-interacting ions with atoms in a MOT in the presence of heating modelled by a single exponential anti-damping factor. This program is used get the qualitative time-evolution of the ion ensemble in the trap.

7. Molecular dynamics simulation of an ensemble of interacting ions subjected to the transient extraction potentials of the ion trap from different initial conditions. This program is used to mimic the process of detection

of the ions and relate their initial spatial spread and temperature with the observed arrival time distribution.

8. Labview programs for controlling various devices on the experiment on a single platform.

Bibliography

[1] M. T. Bell and T. P. Softley. Ultracold molecules and ultracold chemistry. *Molecular Physics*, 107:99, 2009.

[2] W. W. Smith, O. P. Makarov, and J. Lin. Cold ionneutral collisions in a hybrid trap. *Journal of Modern Optics*, 52:2253, 2005.

[3] M. Cetina, A. Grier, J. Campbell, I. Chuang, and V. Vuletić. Bright source of cold ions for surface-electrode traps. *Physical Review A*, 76:041401, 2007.

[4] A. T. Grier, M. Cetina, F. Oručević, and V. Vuletić. Observation of cold collisions between trapped ions and trapped atoms. *Physical Review Letters*, 102:223201, 2009.

[5] C. Zipkes, S. Palzer, C. Sias, and M. Köhl. A trapped single ion inside a boseeinstein condensate. *Nature*, 464:388, 2010.

[6] S. Schmid, A. Härter, and J. H. Denschlag. Dynamics of a cold trapped ion in a bose-einstein condensate. *Physical Review Letters*, 105:133202, 2010.

[7] K. Ravi, S. Lee, A. Sharma, G. Werth, and S. A. Rangwala. Combined ion and atom trap for low temperature ion-atom physics. *Appl. Phys. B: Lasers and Optics*, 107:971, 2012.

[8] S. Willitsch, M. T. Bell, A. D. Gingell, S. R. Procter, and T. P. Softley. Cold reactive collisions between laser-cooled ions and velocity-selected neutral molecules. *Physical Review Letters*, 100:043203, 2008.

[9] C. Zipkes, S. Palzer, L. Ratschbacher, C. Sias, and M. Köhl. Cold heteronuclear atom-ion collisions. *Physical Review Letters*, 105:133201, 2010.

[10] F. H. J. Hall, M. Aymar, N. Bouloufa-Maafa, O. Dulieu, and S. Willitsch. Light-assisted ion-neutral reactive processes in the cold regime: Radia-

tive molecule formation versus charge exchange. *Physical Review Letters*, 107:243202, 2011.

[11] W. G. Rellergert, S. T. Sullivan, S. Kotochigova, A. Petrov, K. Chen, S. J. Schowalter, and E. R. Hudson. Measurement of a large chemical reaction rate between ultracold closed-shell ^{40}Ca atoms and open-shell ^{174}Yb^{+} ions held in a hybrid atom-ion trap. *Physical Review Letters*, 107:243201, 2011.

[12] R. Côté, V. Kharchenko, and M. D. Lukin. Mesoscopic molecular ions in bose-einstein condensates. *Physical Review Letters*, 89:093001, 2002.

[13] K. Blaum, Y. Novikov, and G. Werth. Penning traps as a versatile tool for precise experiments in fundamental physics. *Contemporary Physics*, 51:149, 2010.

[14] A. J. Leggett. Bose-einstein condensation in the alkali gases: Some fundamental concepts. *Reviews of Modern Physics*, 73:307, 2001.

[15] D. Leibfried, R. Blatt, and D. Wineland. Quantum dynamics of single trapped ions. *Reviews of Modern Physics*, 75:281, 2003.

[16] J. Ye, H. J. Kimble, and H. Katori. Quantum state engineering and precision metrology using state-insensitive light traps. *Science*, 320:1734, 2008.

[17] F. G. Major and H. G. Dehmelt. Exchange-collision technique for the rf spectroscopy of stored ions. *Physical Review*, 170:91, 1968.

[18] C. Zipkes, L. Ratschbacher, C. Sias, and M. Köhl. Kinetics of a singe ion trapped in an ultracold buffer gas. *New Journal of Physics*, 13:053020, 2011.

[19] E. A. Cornell and C. E. Wiemann. Nobel lecture: Bose-einstein condensation in a dilute gas, the first 70 years and some recent experiments. *Reviews of Modern Physics*, 74:875, 2002.

[20] M. Weidemüller and C. Zimmermann. *Interactions in Ultracold Gases: From Atoms to Molecules*. John Wiley and Sons, 2003.

[21] S. Giorgini, L. P. Pitaevskii, and S. Stringari. Theory of ultracold atomic fermi gases. *Reviews of Modern Physics*, 80:1215, 2008.

[22] H. J. Metcalf and P. van der Straten. *Laser Cooling and Trapping*. Springer-Verlag, New York, 1999.

[23] F. G. Major, V. N. Gheorghe, and G. Werth. *Charged particle traps*. Springer-Verlag, Heidelberg, 2005.

[24] D. A. Dahl. *Simion 3D Version 7.0 User Manual*. Bechtel BWXT, Idaho, 2000.

[25] H. J. Weber and G. B. Arfken. *Essential Mathematical Methods for Physicists*. Academic Press, 2004.

[26] M. Meucci, E. Mariotti, P. Bicchi, C. Marinelli, and L. Moi. Light-induced atom desorption. *Europhysics Letters*, 25:639, 1994.

[27] E. B. Alexandrov, M. V. Balabas, Budker D., D. English, D. F. Kimball, C. H. Li, and V. V. Yashchuk. Light-induced desorption of alkali-metal atoms from paraffin coating. *Physical Review A*, 66:042903, 2002.

[28] D. A. Steck. *Rubidium 85 D line data*. unpublished, available online at http://steck.us/alkalidata, 2008.

[29] T. Takehoshi, M. G. Brooke, B. M. Patterson, and R. J. Knize. Absolute rb one-color two-photon ionization cross-section measurement near a quantum interference. *Physical Review A*, 69:053411, 2004.

[30] David R. Lide. *CRC Hand Book of Chemistry and Physics*. CRC Press, New York, 2004.

[31] I. S. Lim, J. K. Laerdahl, and P. Schwerdtfeger. The static electric dipole polarizability of Rb^+. *Journal of Physics B*, 33:L91, 2000.

[32] H. Goldstein, C. P. Poole, and J. L. Safko. *Classical Mechanics*. Pearson Education, third edition, 2002.

[33] E. W. McDaniel. *Collision Phenomena in Ionized Gases*. John Wiley and Sons, New York, 1964.

[34] R. E. Olson. Determination of the difference potential from resonant charge-exchange total cross sections: analysis of Rb^+-Rb and Cs^+-Cs. *Physical Review*, 187:153, 1969.

[35] R. Côté and A. Dalgarno. Ultracold atom-ion collisions. *Physical Review A*, 62:012709, 2000.

[36] P. Zhang, A. Dalgarno, and R. Côté. Scattering of Yb and Yb^+. *Physical Review A*, 80:030703(R), 2009.

[37] L. D. Landau and E. M. Lifshitz. *Quantum Mechanics*. Pergamon Press, Oxford, second edition, 1965.

[38] T. Holstein. Mobilities of positive ions in their parent gases. *Journal of Physical Chemistry*, 56:832, 1952.

[39] J. N. Bardsley, T. Holstein, B. R. Junker, and S. Sinha. Calculations of ion-atom interactions relating to resonant charge-transfer collisions. *Physica Review A*, 11:1911, 1975.

[40] C. Herring. Critique of the Heitler-London method of calculationg spin-couplings at large distances. *Reviews of Modern Physics*, 34:631, 1962.

[41] B. H. Bransden and C. J. Joachain. *Physics of Atoms and Molecules*. Pearson Education, second edition, 2003.

[42] B. M. Smirnov. *Physics of atoms and ions*. Springer-Verlag, 2003.

[43] B. M. Smirnov. Atomic structure and the resonant charge exchange process. *Physics-Uspekhi*, 44:221, 2001.